論文 / 著書情報
Article / Book Information

題目(和文)	
Title(English)	Precipitation, Transformation and Growth of Iron Particles in a Copper Matrix
著者(和文)	藤居俊之
Author(English)	TOSHIYUKI FUJII
出典(和文)	学位:博士(工学), 学位授与機関:東京工業大学, 報告番号:甲第2532号, 授与年月日:1992年12月31日, 学位の種別:課程博士, 審査員:
Citation(English)	Degree:Doctor of Engineering, Conferring organization: , Report number:甲第2532号, Conferred date:1992/12/31, Degree Type:Course doctor, Examiner:
学位種別(和文)	博士論文
Type(English)	Doctoral Thesis

TOKYO INSTITUTE OF TECHNOLOGY

PRECIPITATION, TRANSFORMATION AND GROWTH OF IRON PARTICLES IN A COPPER MATRIX

A DISSERTATION
for the Degree
DOCTOR OF ENGINEERING
Field of Materials Science and Engineering

by
TOSHIYUKI FUJII

Nagatsuta
Midori-ku
Yokohama, Japan

1992

CONTENTS

Chapter 1.

General Introduction

This thesis describes studies on various aspects of physical metallurgy of precipitate iron particles in a copper matrix using Cu-Fe and Cu-Fe-Co alloys. In this chapter, the Cu-Fe alloy system will first be overviewed briefly and then the motivation of the present studies will be introduced.

1.1. The Cu-Fe system

When a supersaturated Cu-Fe solid solution with less than 4 mass% Fe is aged, owing to the small lattice misfit between copper and γ-iron, spherical and coherent γ-iron (f.c.c.) particles are first formed in a copper matrix [1, 2]. As can be seen in the Cu-Fe equilibrium phase diagram [3] in Fig. 1-1, the γ-iron particles are thermodynamically metastable below 1185K. However, they do not transform into stable α-iron even when the alloy is simply cooled down to the liquid helium temperature (4.2K) [4]. To introduce the γ→α transformation in the iron particles, either plastic deformation of the alloy [2, 5-7], extraction of the particles from the copper matrix [8], or prolonged aging (for example, over 30d when aged at 973K) [9, 10] is necessary. The γ-iron particles are paramagnetic at room temperature and have the Neel temperature at about 100K [11]. On the other hand, the transformed α-iron particles are, of course, ferromagnetic. Therefore, the γ→α transformation accompanies the magnetic change.

The γ→α transformation caused by plastic deformation is martensitic in nature and, as a result, a layered internal structure consisting of two twin-related α-iron variants is formed in the transformed particles [7, 8, 12]. Both of the variants nearly satisfy the Kurdjumov-Sachs (KS) orientation relationship, $\{111\}_{Cu}//\{110\}_{Fe}$ and $\langle 110\rangle_{Cu}//\langle 111\rangle_{Fe}$, to the copper matrix [7, 8, 12].

Annealing of the as-transformed α-iron particles is known to induce a spherical to ellipsoidal shape change with the direction of elongation parallel to $\langle 110\rangle_{Cu}$ [13]. Associated with this change is the disappearance of the twinned structure and the α-iron particles eventually become single crystals.

1.2. Historical background and the motivation of the present study

The Cu-Fe alloy system is unique, useful and interesting. Various aspects of physical

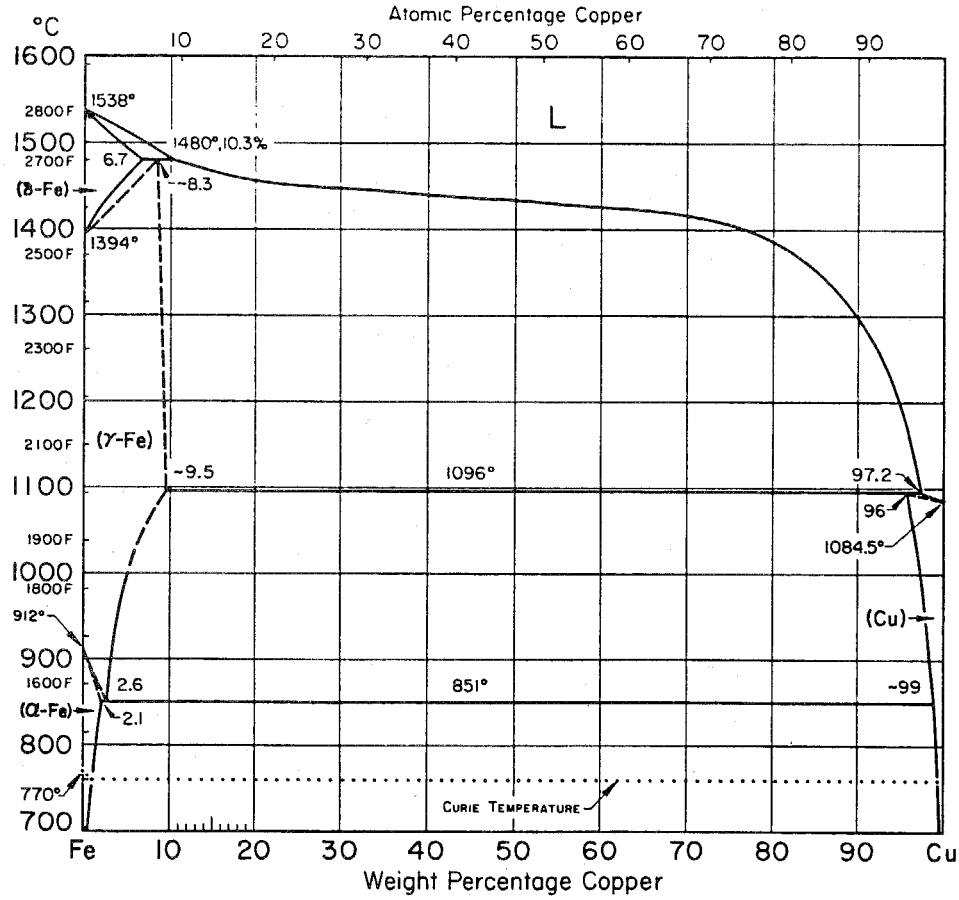

Fig. 1-1. Equilibrium phase diagram of the Cu-Fe system [3].

metallurgy can be studied using this alloy. (1) phase transformation, (2) growth and coarsening kinetics of precipitates, (3) magnetism, (4) crystallography of precipitates are among them and all of these will be studied in this thesis. In the following, unique features of the Cu-Fe system to investigate such topics as above will be listed and the motivation and aim of the present study will be identified.

As for (1), it is well known that martensitic transformations are affected by external stresses such as a uniaxial stress or hydrostatic pressure [7, 13-25]. The Cu-Fe system is very suited for the investigation of the stress effects since the transformable sites are pre-determined as the iron particles. There are two different ways of understanding the stress effects. The more commonly accepted one is that due to Patel and Cohen [14]. They considered that the applied stress helped the total shape deformation accompanying the transformation. The other, proposed by Bogers and Burgers [16], considers that the applied stress helps the shear deformation involved in the lattice change.

Although many experimental studies have been performed [7, 20-22, 26-29], it appears that the stress effects on martensitic transformations have not been clearly understood. This is possibly because various mechanical effects, such as those of internal stresses and interaction between martensites, almost always appear during the course of the transformation. These may inevitably mask the true effect of the applied stress. Since the volume fraction of the γ-iron particles is small and the distance between particles is large compared with the particle size, the direct effect of the applied stress on the $\gamma \rightarrow \alpha$ martensitic transformation can be expected in the Cu-Fe alloy with no need to pay attention to the internal stresses and the interaction.

For (2) the growth and coarsening kinetics of precipitates, Matsuura *et al.* [30] examined the growth of γ-iron particles and found that the growth rate obeyed the Lifshitz-Slyozov-Wagner (LSW) law [31, 32] of the Ostwald ripening. From this, they evaluated the coherent γ-Fe/Cu interfacial energy. Applying a proper heat treatment and deformation, one can obtain a Cu-Fe alloy containing both γ- and α-iron particles. It is interesting to know what happens when the two different kinds of particles coexist during the particle growth process. The unique feature of the Cu-Fe alloy system gives us a unique opportunity to study this subject.

Although aging of a supersaturated solid-solution Cu-Fe polycrystals induces the precipitation of coherent γ-iron particles inside the grains, incoherent α-iron particles are usually formed on grain boundaries from the beginning of aging [33]. To investigate the grain-boundary precipitation, however, a Cu-Fe-Co alloy is more suited since ternary addition of Co to the Cu-Fe alloy is known to enhance the precipitation of boundary α-Fe-Co particles [34]. It is well known that the nucleation

frequency and morphology of grain-boundary precipitates depend strongly on the character of grain boundaries [35-45]. Monzen *et al.* recently investigated the grain-boundary precipitation in the early stage of aging using orientation-controlled Cu-Fe-Co bicrystals [34, 45]. They have shown excellent correlation between the grain-boundary energy and the precipitation frequency: the larger the boundary energy, the more precipitates are formed. It is expected that if longer aging is conducted, the boundary α-Fe-Co particles will grow and its morphology will change. Although the growth of boundary precipitates has been studied by several investigators [41, 44], usage of polycrystals prohibited them from finding the relationship between growth kinetics and grain-boundary character. In this study, this point will be examined using orientation-controlled Cu-Fe-Co bicrystals.

During the course of the investigation, the LSW theory as applied to one-, two- and three-dimensional diffusion mechanisms had to be considered. As a by-product of the present study, a new method was found to derive the fundamental rate equations for particle growth very easily.

When single crystals of a Cu-Fe alloy are used to investigate the stress-induced $\gamma \rightarrow \alpha$ martensitic transformation, specific KS variants out of 24 crystallographically equivalent ones are formed preferentially depending on the sense (tension or compression) and direction of the applied stress [7, 46]. Moreover, as mentioned earlier, the α-iron particles grow and elongate along $\langle 110 \rangle_{Cu}$ directions on annealing. These phenomena will introduce magnetic anisotropy, due to both crystal- and shape-anisotropy effects, in the alloy. In turn, if magnetic anisotropy of the alloy is measured, one may be able to know what stress-induced variants are formed preferentially. As for (3) magnetism, this idea will be pursued.

Finally, for (4) the crystallography of precipitates, the morphology and crystallography of elongated (well-grown) α-iron particles in a copper matrix will be investigated. It is known that the particle/matrix interface orientation is often determined so as to make the interface "best fitted" [47-53]. Kato *et al.* recently proposed geometrical criteria to predict and explain the crystallography and morphology of best-fit interfaces [54]. If these criteria hold, the interface orientation between the α-iron particles and the copper matrix must be described by the Bain correspondence since the molar volumes of the two crystals are almost the same [54]. It is true that the geometrical criteria were originally developed to discuss epitaxial relationships between substrate and deposit crystals. Since the combination of copper and iron, one for the substrate and the other for the deposit, was mainly used experimentally by Kato *et al.*, it is of particular interest to examine whether or not the criteria is also applicable to the α-iron precipitate/copper matrix interface.

1.3. Outline of this thesis

In Chapter 2, "Stress Effects on Martensitic Transformation of Small Iron Particles in a Copper Matrix", the stress effect on the $\gamma \rightarrow \alpha$ martensitic transformation in small iron particles is examined using single crystals. It is concluded that applied stress helps the shear deformation involved in the f.c.c. to b.c.c. lattice change.

In Chapter 3, "Growth of α-Iron Particles in a Copper Matrix", the growth kinetics of α-iron particles in a copper matrix is examined for the cases where only α-iron particles exist and where both α- and γ-iron particles coexist. By applying the LSW theory, the α-Fe/Cu interfacial energy is evaluated. In addition, the fundamental rate equations for Ostwald ripening processes are derived by taking directly into account the change in interfacial free energies.

In Chapter 4, "Magnetic Anisotropy Caused by the Formation of Stress-Induced Martensite in Small Iron Particles in a Copper Matrix", magnetic anisotropy of Cu-Fe single crystals with transformed α-iron particles is investigated by measuring magnetic torque which appears when a sample is set in a magnetic field. From this measurement, the preferential formation of stress-induced particular KS variants of α-iron particles as well as the shape change of the particles by annealing is detected.

In Chapter 5, "Crystallography and Morphology of Needle-Like α-Iron Particles in a Copper Matrix", the crystallography and morphology of elongated α-iron particles in a copper matrix are studied. It is found that the experimental results can be explained excellently by adopting the recently developed geometrical criteria for interface crystallography.

In Chapter 6, "Growth of Grain-Boundary Precipitates in Cu-Fe-Co Bicrystals", the growth of α-Fe-Co particles on [011] symmetric tilt boundaries in Cu-Fe-Co bicrystals is examined. The change in the width of precipitate-free zones with aging is also investigated. By considering both the volume diffusion of iron atoms in the copper matrix and the pipe diffusion through grain-boundary dislocations, the growth mechanism of the boundary precipitates is discussed.

In Chapter 7, "General Summary and Future Prospects", the contents and main findings and conclusions of this thesis are summarized and some remarks for possible future studies are presented.

References

[1] F. Bitter and A. R. Kaufmann: *Phys. Rev.*, **56** (1939), 1044.

[2] C. S. Smith: *Phys. Rev.*, **57** (1940), 337.

[3] R. E. Johnson: *Metals Handbook*, 8th Edition Vol.8 Edited by T. Lyman, American Society for Metals, Ohio, (1973), p. 293.

[4] J. M. Denney: *Acta Metall.*, **4** (1956), 586.

[5] K. E. Easterling and H. M. Miekk-Oja: *Acta Metall.*, **15** (1967), 1133.

[6] K. E. Easterling and G. C. Weatherly: *Acta Metall.*, **17** (1969), 845.

[7] M. Kato, R. Monzen and T. Mori: *Acta Metall.*, **26** (1978), 605.

[8] H. Kubo, Y. Uchimoto and K. Shimizu: *Met. Sci. J.*, **9** (1975), 61.

[9] J. B. Newkirk: *Trans. AIME*, **209** (1957), 1214.

[10] Y. Watanabe, M. Kato and A. Sato: *J. Mater. Sci.*, **26** (1991), 4307.

[11] U. Gonser, C. J. Meechan, A. H. Muir and H. Wiedersich: *J. Appl. Phys.*, **34** (1963), 2373.

[12] K. R. Kinsman, J. W. Sprys and R. J. Asaro: *Acta Metall.*, **23** (1975), 1431.

[13] R. Monzen, A. Sato and T. Mori: *Trans. Jap. Inst. Met.*, **22** (1981), 65.

[14] J. R. Patel and M. Cohen: *Acta Metall.*, **1** (1953), 531.

[15] J. A. Venables: *Phil. Mag.*, **7** (1962), 35.

[16] A. J. Bogers and W. G. Burgers: *Acta Metall.*, **12** (1964), 255.

[17] J. F. Breedis: *Acta Metall.*, **13** (1965), 239.

[18] R. W. Pohde and R. A. Graham: *Trans. AIME*, **245** (1969), 2441.

[19] P. L. Mangonon Jr and G. Thomas: *Met. Trans.*, **1** (1970), 1587.

[20] Y. Higo, F. Lecroisey and T. Mori: *Acta Metall.*, **22** (1974), 313.

[21] M. Kato and T. Mori: *Acta Metall.*, **24** (1976), 853.

[22] M. Kato and T. Mori: *Acta Metall.*, **25** (1977), 951.

[23] A. Sato, M. Kato, Y. Sunaga, T. Miyazaki and T. Mori: *Acta Metall.*, **28** (1980), 367.

[24] A. Sato, H. Kasuga and T. Mori: *Acta Metall.*, **28** (1980), 1223.

[25] T. Kakeshita, K. Shimizu, Y. Akahama, S. Endo and F. E. Fujita: *Trans. Jap. Inst. Met.*, **29** (1987), 109.

[26] G. Stone and G. Thomas: *Met. Trans.*, **5** (1974), 2095.

[27] D. Goodchild, W. T. Roberts and D. V. Wilson: *Acta Metall.*, **18** (1970), 1137.

[28] G. F. Bolling and R. H. Richman: *Scripta Metall.*, **4** (1970), 539.

[29] H. Onodera, H. Goto and I. Tamura: *Proc. 1st JIM Int'l Symp. on New Aspects on Martensitic*

Transformation, The Japan Institute of Metals, (1976), 327.

[30] K. Matsuura, M. Kitamura and K. Watanabe: *J. Jap. Inst. Met.*, **41** (1977), 1285.

[31] I. M. Lifshitz and V.V. Slyozov: *J. Phys. Chem. Solids*, **19** (1961), 35.

[32] C. Wagner: *Z. Elektrochem.*, **65** (1961), 581.

[33] N. Shigenaka, R. Monzen and T. Mori: *Acta Metall.*, **31** (1983), 2087.

[34] R. Monzen and K. Kitagawa: *Scripta Metall.*, **22** (1988), 173.

[35] D. Vaughan: *Acta Metall.*, **16** (1968), 563.

[36] P. N. T. Unwin and R. B. Nicholson: *Acta Metall.*, **17** (1969), 1379.

[37] D. Vaughan: *Acta Metall.*, **18** (1970), 183.

[38] J. Le Coze, C. Ranson and C. Goux: *C. r. Acad. Sci. Paris*, **C291** (1970), 1120.

[39] J. Le Coze and C. Goux: *C. r. Acad. Sci. Paris*, **C291** (1970), 1225.

[40] J. Le Coze, M. Biscondi, J. Levy and C. Goux: *Mém. Sci. Rev. Métall.*, **70** (1973), 397.

[41] E. P. Butler and P.R. Swann: *Acta Metall.*, **24** (1976), 343.

[42] B. Forest and M. Biscondi: *Met. Sci.*, **12** (1978), 202.

[43] J. K. Park and A. J. Ardell: *Acta Metall.*, **34** (1986), 2399.

[44] P. Czurratis, R. Kroggel and H. Löffer: *Z. Metall.*, **79** (1988), 307.

[45] R. Monzen, K. Kitagawa, M. Kato and T. Mori: *J. Jap. Inst. Met.*, **54** (1990), 1308.

[46] M. Kato, T. Fujii, Y. Hoshino and T. Mori: *J. Jap. Inst. Met.*, **56** (1992), 865.

[47] G. C. Weatherly, P. Humble and D. Borland: *Acta Metall.*, **27** (1979), 1815.

[48] A. Crosky, P.G. McDougall and J. S. Bowles: *Acta Metall.*, **28** (1980), 1495.

[49] U. Dahmen: *Acta Metall.*, **30** (1982), 63.

[50] U. Dahmen and K. H. Westmacott: *Proc. Int. Conf. Solid-Solid Trans.*, TMS-AIME, New York, (1982), p.433.

[51] U. Dahmen, P. Ferguson and K. H. Westmacott: *Acta Metall.*, **32** (1984), 803.

[52] C. P. Luo and G. C. Weatherly: *Acta Metall.*, **35** (1987), 1963.

[53] C. P. Luo and G. C. Weatherly: *Phil. Mag.*, **A58** (1988), 445.

[54] M. Kato, M. Wada, A. Sato and T. Mori: *Acta Metall.*, **37** (1989), 749.

Chapter 2.
Stress Effects on the Martensitic Transformation of Small Iron Particles in a Copper Matrix

2.1. Introduction

It is well known that uniaxial applied stress helps martensitic transformations and raises the martensite start (M_s) temperature. This can naturally be understood since the martensitic transformations are characterized by diffusionless and shear-type ones. The stress-induced martensites, thus formed, may be crystallographically and morphologically different from martensites formed by simple cooling. By simple cooling, all crystallographically equivalent martensite variants can be formed with equal probabilities. On the other hand, if the transformation is assisted by stress, only a few variants may be formed preferentially [1, 2].

However, even if we limit ourselves to the f.c.c. (γ) to b.c.c. (α) transformation in ferrous alloys, no unanimous understanding of the stress effects on the martensitic transformation appears to be established. Many investigators [3-6] follow the thermodynamic discussion developed by Patel and Cohen [1]. They have considered that the stress helps the total shape deformation accompanying the transformation. This stress effect will be referred to as the "stress effect on the shape deformation". For a plate-shaped martensite, the total shape deformation consists of a shear component parallel to the habit plane and a dilatational component perpendicular to the habit plane. Patel and Cohen considered that such a martensite variant whose total shape deformation is most effectively helped by the applied stress is formed most easily.

Another way of understanding the stress effect is that the applied stress helps the shear movement of atoms to change the lattice [2, 7-12]. As the shear movement, the $\{111\}\langle 211\rangle$ shear system of the γ phase is considered by Bogers and Burgers [7] and the occurrence of the two independent $\{111\}\langle 211\rangle$ shear systems results approximately in the lattice change from f.c.c. to b.c.c. (the Bain deformation). This shear movement is considered to occur in the early stage of the transformation [8-12]. The stress effect of this type will be referred to as the "stress effect on the lattice change".

According to the phenomenological crystallographic theory of martensitic transformations [13, 14], the total shape deformation consists of lattice deformation (Bain deformation), lattice-invariant deformation and rigid-body rotation. Since the lattice deformation considered in the latter stress effect is only a part of the total shape deformation, it may appear very easy to experimentally find

which stress effect plays a more important role. However, if polycrystals are used for the experiment, since the stress effect varies with the orientation of individual grains, it is difficult to make a conclusive argument. Moreover, as will be mentioned later, even if single crystals are used for the experiment, unless proper combinations of alloy systems and experimental conditions are selected, it is not easy to know the predominant stress effect from the observed preferentially formed stress-induced martensite variants.

The main purpose of the present study is to find which of the above two stress effects is more important. The Cu-Fe alloy system is best suited for this purpose. This is because only the γ-iron particles embedded in the copper matrix can undergo the f.c.c. to b.c.c. martensitic transformation and, therefore, the transformable sites in the alloy are pre-determined and limited. On the other hand, if a usual austenitic alloy is used as a starting material to investigate the stress-induced martensitic transformation, any region of the parent austenite phase can transform. In such a case, internal stresses developed by the formation of martensites *per se* and the interaction between martensite plates may affect the successive formation of martensite variants. If this is the case, it is impossible to regard that the formation of all the martensites is assisted by the applied stress. In fact, such phenomena as the autocatalytic effect [17] and the self-accommodating morphology [18] are well known to be caused by the effects of the internal stresses and the interaction between martensites. On the contrary, since the volume fraction of the iron particles in the copper matrix is small, the effects of the internal stresses and the interaction between the particles can be neglected and the direct effect of the applied stress can reasonably be expected for the preferential formation of stress-induced variants.

Using this alloy, Kato *et al.* [11] identified the stress-induced variants and concluded that the stress effect on the lattice change was more important. In the present study, as an extension of the study by Kato *et al.*, preferentially formed martensite variants will be investigated by applying the external tensile and compressive stresses along [001] and [419] to Cu-Fe single crystals. Furthermore, the fraction of transformed α-iron particles will be examined as a function of the amount of plastic strain.

2.2. Experimental

2.2.1. Specimen preparation

Single crystals of a Cu-1.5mass%Fe alloy were grown by the Bridgman method. Tensile (3×3×50mm) and compressive (3×3×5mm) specimens were cut from the single crystals so as to

have the stress axis of either [001] or [419]. These specimens were solution treated at 1273K for 4h and quenched into water. To obtain precipitated γ-iron particles (average diameter of 100nm) in the copper matrix, the specimens were aged at 973K for 3d. According to the Cu-Fe equilibrium phase diagram, the volume fraction of the γ-iron particles is 1.40vol%.

2.2.2. Stress-induced martensites

To know the amount of plastic strain accurately, several micro-Vickers indentations were pressed near the central part of the specimens. Then, the specimens were deformed either in tension or in compression using the Instron-type testing machine at the cross-head speed of 5×10^{-3} mm/s. Specimens to examine preferentially formed variants by transmission electron microscopy (TEM) were deformed at 77K (liquid nitrogen) by about 10% plastic strain. The deformation induced the $\gamma\rightarrow\alpha$ martensitic transformation in practically all the particles. On the other hand, specimens to examine the fraction of transformed particles were deformed at room temperature and various plastic strains were imposed.

2.2.3. TEM observation

Deformed single-crystal specimens were cut parallel to {111} planes to make thin foils for TEM. Final electrolytic polishing was performed using the HNO_3:CH_3OH = 1:4 solution at 243K and 5V. A Hitachi H-700 TEM was used under the acceleration voltage of 200kV.

2.2.4. Magnetic measurement

To find the amount of transformed particles as a function of plastic strain, saturation magnetization of deformed specimens was measured using a vibrating sample magnetometer (VSM). Figure 2-1 shows the construction of VSM. A magnetic field of 10T is applied to magnetize a specimen S to saturation. By moving the specimen up and down (amplitude: 0.1-0.2mm, frequency: 80Hz), vibrating magnetic flux is produced in a search coil C. The saturation magnetization of the specimen is obtained by comparing the induced alternating current of the search coil with that of another search coil set at a standard magnet M.

The saturation magnetization of iron at room temperature is 2.16T [19]. Therefore, if all the iron particles are assumed to have transformed into α-iron, the saturation magnetization of

$$I_S = 2.16 \times 1.40 \times 10^{-2}\ [\mathrm{T}] = 3.01 \times 10^{-2}\ [\mathrm{T}]$$

can be expected. If the measured saturation magnetization of the specimen is I, I/I_S is defined as the fraction of transformed particles in the present study.

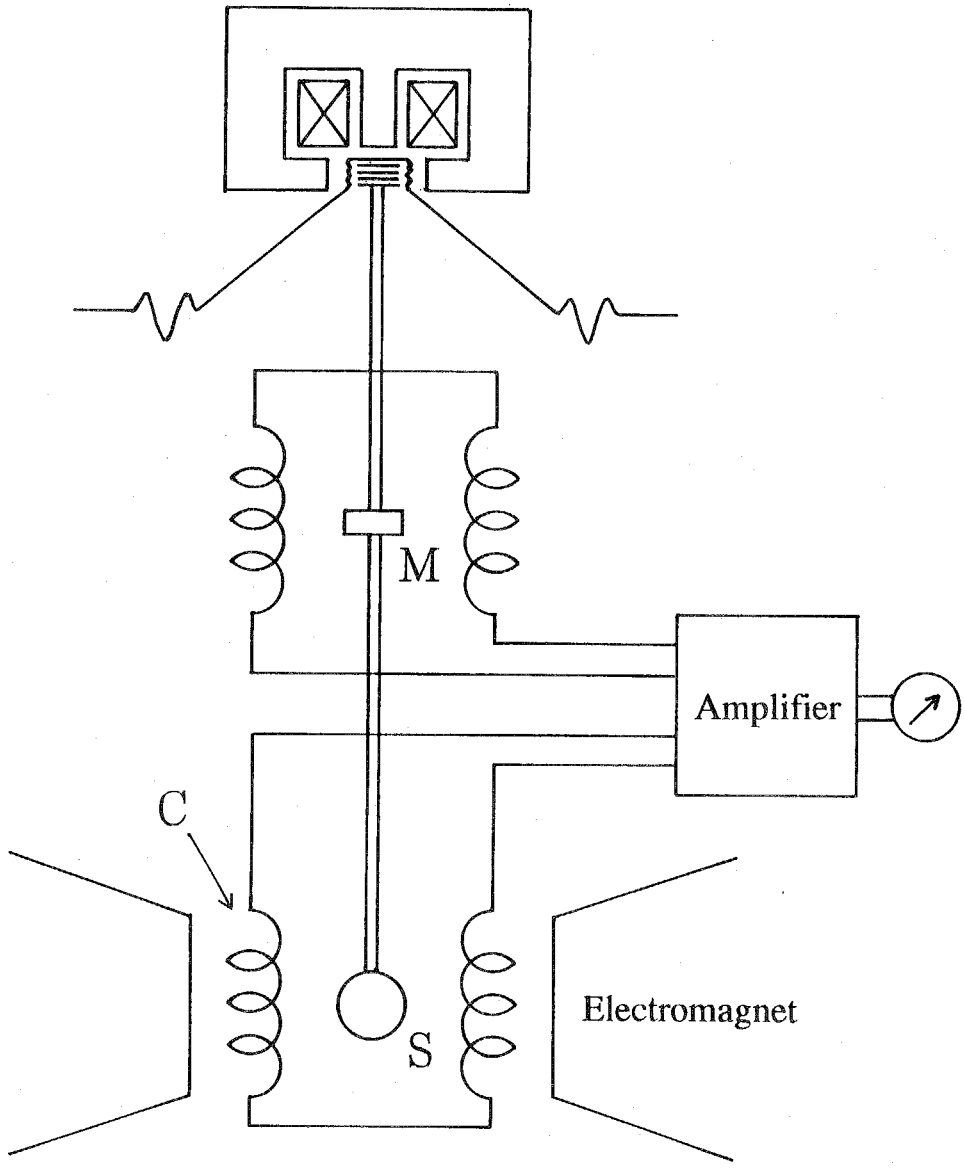

Fig. 2-1. Schematic diagram of the vibrating sample magnetometer.

2.2.5. Notation of 24 KS variants

As mentioned earlier, the α-iron martensite particles have nearly the KS orientation relationship to the copper matrix. Therefore, following the notation adopted in the previous studies [8, 9], the 24 KS variants are denoted as in Table 2-1. In the following, the subscripts f and b will denote f.c.c. and b.c.c., respectively.

2.3. Results

2.3.1. TEM observation

Preferentially formed variants were identified by taking diffraction patterns and dark-field micrographs. The specimens with deformation axes $[001]_f$ and $[419]_f$ will be referred to as the [001] and [419] specimens.

Figure 2-2 shows the bright-field micrograph of an [001] specimen deformed by 8% in tension. Each α-iron particle consists of alternating layers of twin-related variants with the layers parallel to $\langle 110 \rangle_f$ directions. For the [001] specimens, all the four $\{111\}_f$-type planes are crystallographically equivalent. Therefore, all the observed variants can be represented as those belonging to the family of the $(\bar{1}1\bar{1})_f$ plane in Table 2-1. For example, both of the two different variants of α-iron particles seen in Fig. 2-2 can be represented as those consisting of the twinned KS variants 1-3 and 1-6.

The same [001] specimen as above was observed with the incident beam parallel to $(\bar{1}1\bar{1})_f$ as shown in Fig. 2-3. The bright-field micrograph is shown in (a) and the dark-field micrograph (b) was taken using the $1\bar{1}0_A$ spot of the 1-3 variant in the diffraction pattern (c). Comparison between the bright-field and dark-field micrographs reveals that almost all the particles are made of the (1-3, 1-6) variant pair.

Similar observation was performed for an [001] specimen deformed by 9% in compression. It was found that α-iron particles consisting of the (1-1, 1-4) twin pair and the (1-2, 1-5) twin pair were formed approximately in equal amounts.

For the [419] specimens, the four $\{111\}_f$ planes are no longer equivalent. Therefore, rather tedious TEM observations had to be performed by preparing four types of thin foils, each parallel to either one of the four $\{111\}_f$ planes. As a result, the (1-3, 1-6) pair was found to be predominant in a [419] specimen deformed in tension and the (1-1, 1-4) and (2-1, 2-4) pairs were found to be preferentially formed in a [419] specimen deformed in compression. These results are summarized

Table 2-1. Notation of the 24 KS variants.

Variant name	Plane (fcc)//(bcc)		Direction [fcc]//[bcc]		Twin-related variant
1-1	$(\bar{1}1\bar{1})$	(110)	$[10\bar{1}]$	$[\bar{1}1\bar{1}]$	1-4
1-2			$[0\bar{1}\bar{1}]$	$[\bar{1}11]$	1-5
1-3			$[\bar{1}\bar{1}0]$	$[\bar{1}1\bar{1}]$	1-6
1-4			$[\bar{1}01]$	$[\bar{1}11]$	1-1
1-5			[011]	$[\bar{1}1\bar{1}]$	1-2
1-6			[110]	$[\bar{1}11]$	1-3
2-1	(111)	(110)	$[\bar{1}01]$	$[\bar{1}1\bar{1}]$	2-4
2-2			$[0\bar{1}1]$	$[\bar{1}11]$	2-5
2-3			$[1\bar{1}0]$	$[\bar{1}1\bar{1}]$	2-6
2-4			$[10\bar{1}]$	$[\bar{1}11]$	2-1
2-5			$[01\bar{1}]$	$[\bar{1}1\bar{1}]$	2-2
2-6			$[\bar{1}10]$	$[\bar{1}11]$	2-3
3-1	$(1\bar{1}\bar{1})$	(110)	$[\bar{1}0\bar{1}]$	$[\bar{1}1\bar{1}]$	3-4
3-2			$[01\bar{1}]$	$[\bar{1}11]$	3-5
3-3			[110]	$[\bar{1}1\bar{1}]$	3-6
3-4			[101]	$[\bar{1}11]$	3-1
3-5			$[0\bar{1}1]$	$[\bar{1}1\bar{1}]$	3-2
3-6			$[\bar{1}\bar{1}0]$	$[\bar{1}11]$	3-3
4-1	$(\bar{1}\bar{1}1)$	(110)	[101]	$[\bar{1}1\bar{1}]$	4-4
4-2			[011]	$[\bar{1}11]$	4-5
4-3			$[\bar{1}10]$	$[\bar{1}1\bar{1}]$	4-6
4-4			$[\bar{1}0\bar{1}]$	$[\bar{1}11]$	4-1
4-5			$[0\bar{1}\bar{1}]$	$[\bar{1}1\bar{1}]$	4-2
4-6			$[1\bar{1}0]$	$[\bar{1}11]$	4-3

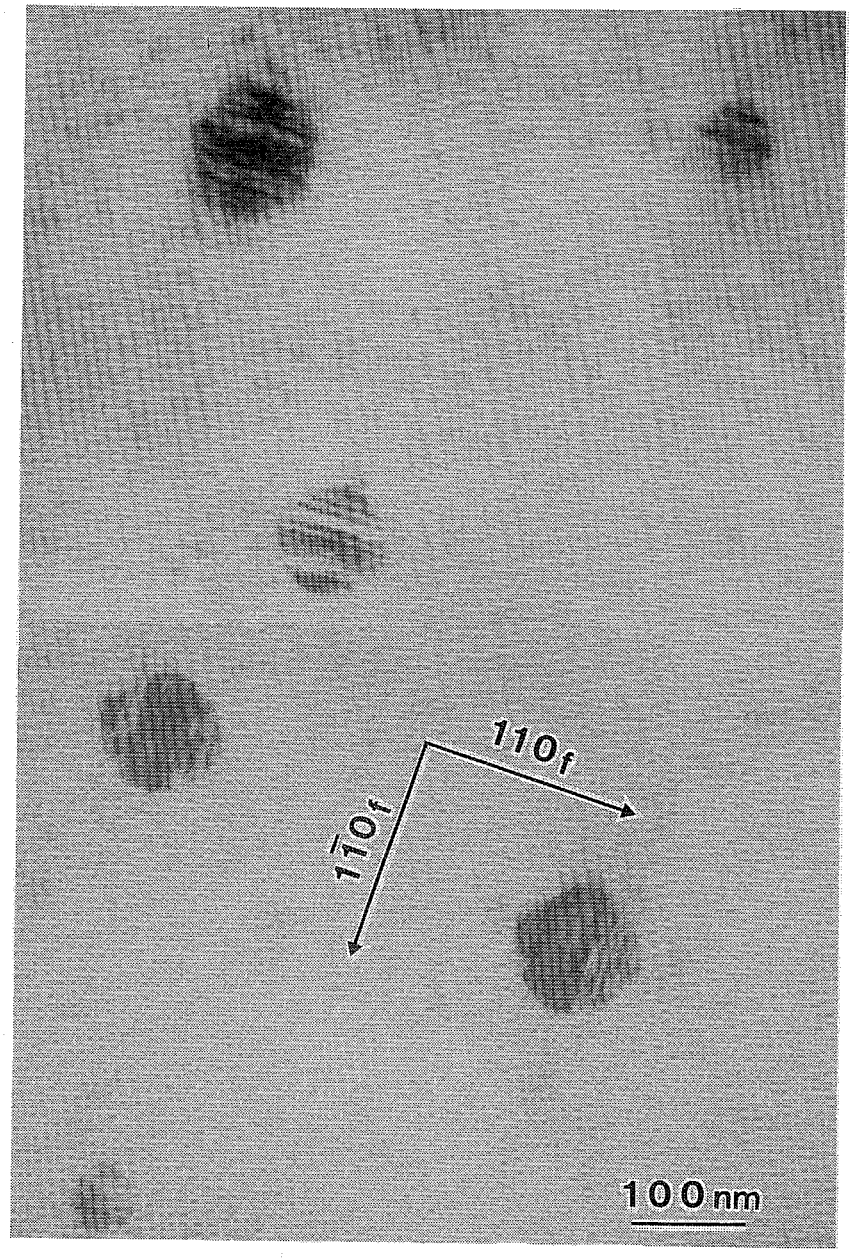

Fig. 2-2. TEM micrographs of the [001] specimen deformed by 8% in tension at 77K. Zone axis: $[001]_f$.

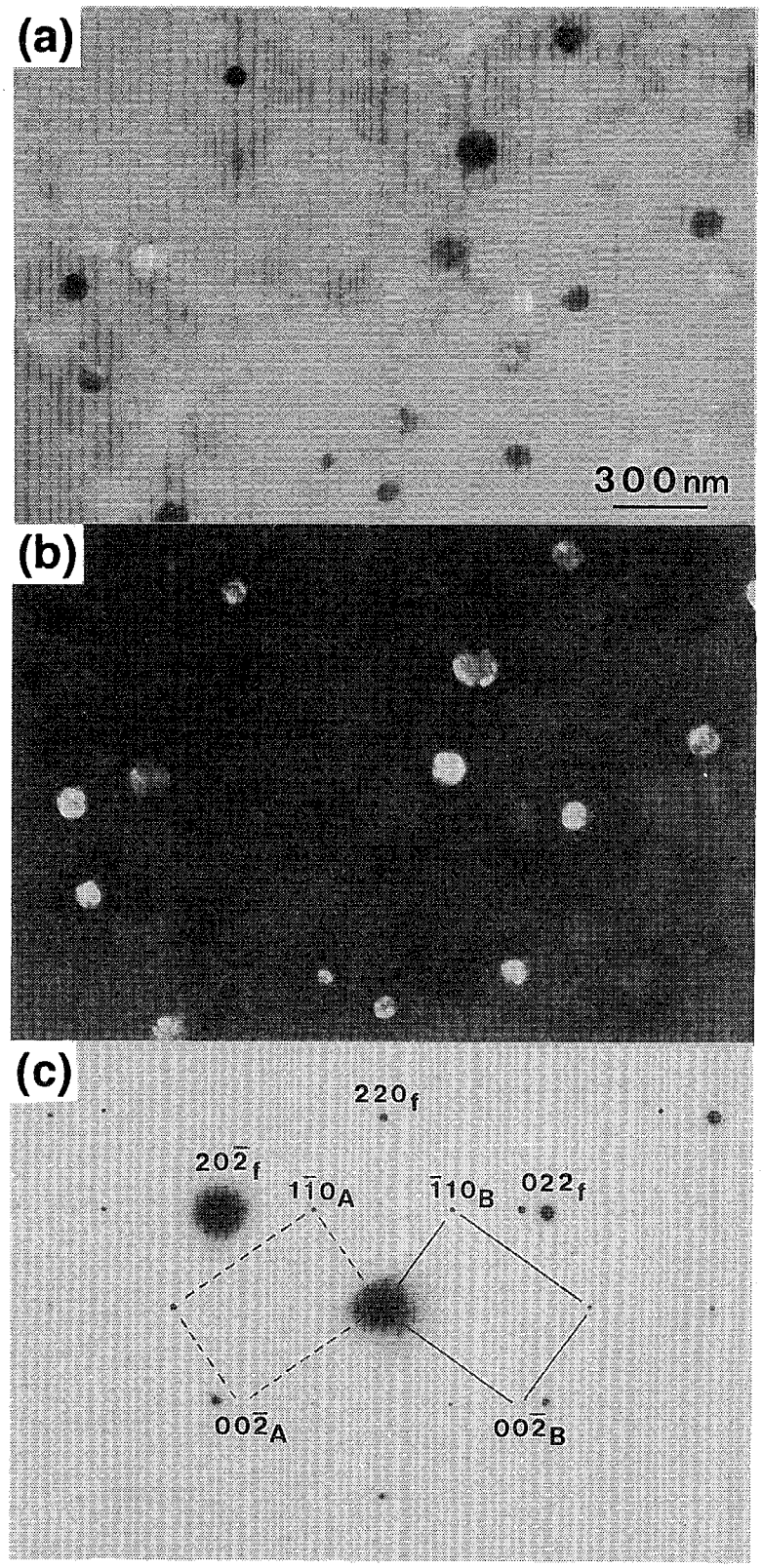

Fig. 2-3. Bright- and dark-field micrographs of the [001] specimen taken with the $[\bar{1}1\bar{1}]_f$ zone axis. In the diffraction pattern (c), spots from the twin-related KS variants 1-3 (dotted lines) and 1-6 (solid lines) are noted in addition to the 220_f-type spots from the copper matrix. The dark-field micrograph (b) was taken using the $1\bar{1}0_A$ spot in (c).

in Table 2-2.

2.3.2. Volume fraction of transformed particles

Figures 2-4 (a) and (b) show the volume fraction of transformed α-iron particles in the [001] and [419] specimens as a function of plastic shear strain. For comparison, data for polycrystals of the same alloy are shown in Fig. 2-4(c). These polycrystals were subjected to the same heat treatment as that for the single crystals and have the average grain size of 180μm. To convert the tensile (compressive) strain into the shear strain, the Taylor factor of 3.06 was adopted.

Monzen *et al.* [20] have shown that slip dislocations introduced and multiplied by the plastic deformation act as amplifiers of the applied stress, giving the same but enlarged shear component of the applied stress to the γ-iron particles. According to them, such dislocations are needed to induce the γ→α martensitic transformation in the iron particles. Since this means that plastic deformation is necessary for the transformation to take place, plastic shear strain was taken as the abscissa in Fig. 2-4.

Regardless of the sense (tension or compression) of the applied stress, the martensitic transformation is naturally promoted. Therefore, the fraction of transformed particles increases as plastic strain increases. However, it should be noted that when comparison is made at the same amount of plastic strain, compressive deformation induces more martensites than tensile deformation in the [001] specimens. On the other hand, the converse is true for polycrystalline specimens and no significant difference can be seen between tension and compression for the [419] specimens. These results suggest that the degree of promoting the martensitic transformation depends on the sense and direction of the applied stress. This important point will be discussed later in the light of the TEM observation.

2.4. Discussion

2.4.1. Preferentially formed variants

As mentioned in Introduction, two stress effects, one on the shape deformation and the other on the lattice change, have been proposed. Here, the observed variants in Table 2-2 will be discussed on the basis of these two stress effects.

As repeatedly mentioned, an α-iron particle is made of two twin-related variants. These variants are considered to be formed as a result of the occurrence of different (though crystallographically equivalent) lattice deformations (Bain deformations). For example, let us

Table 2-2. Observed preferentially-formed KS variants of twinned α-iron martensite particles in a copper matrix.

Stress axis	$[001]_f$		$[419]_f$	
	Tension	Compression	Tension	Compression
Observed variants	1-3, 1-6	1-1, 1-4 1-2, 1-5	1-3, 1-6	1-1, 1-4 2-1, 2-4

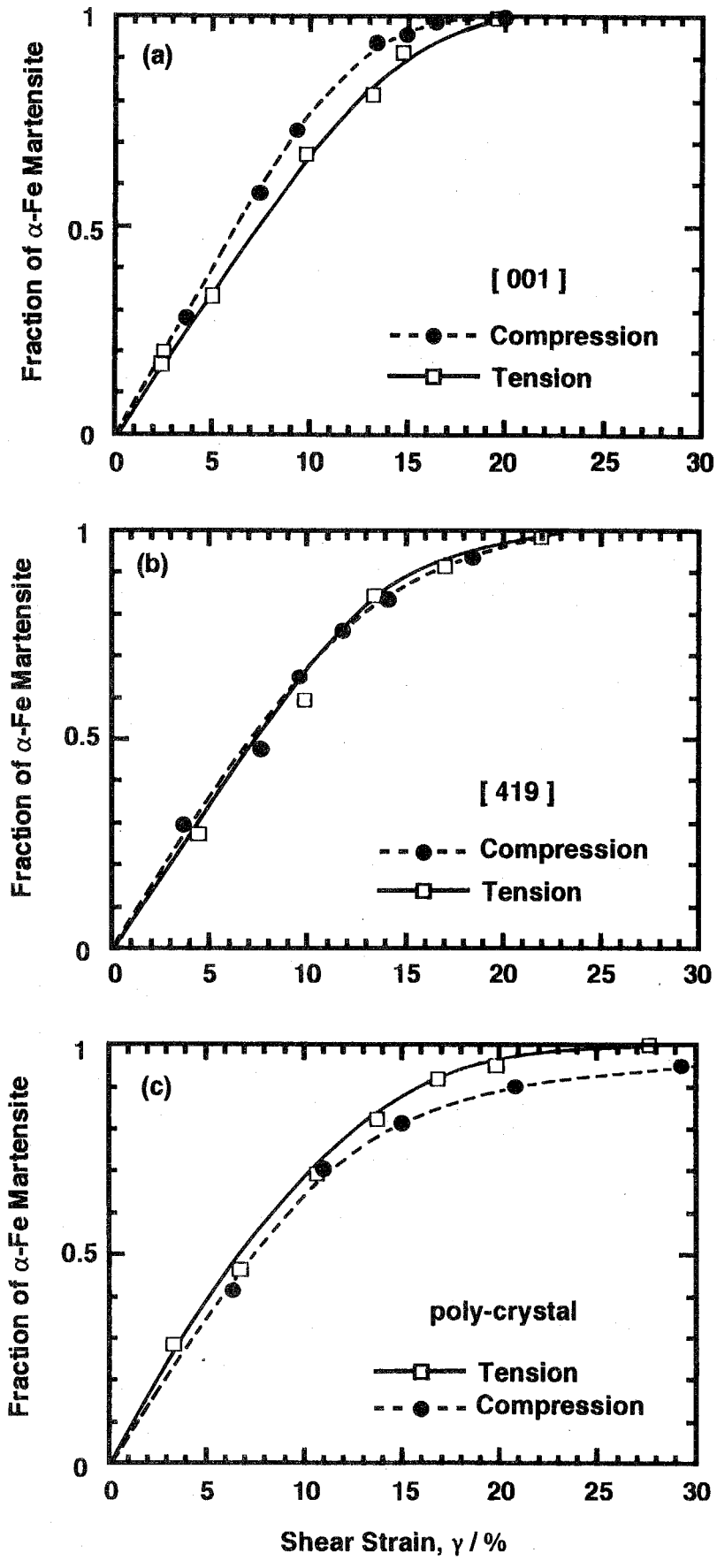

Fig. 2-4. Volume fraction of transformed α-iron martensite particles measured as a function of plastic shear strain. (a) [001] specimen, (b) [419] specimen and (c) polycrystalline specimen.

consider the twin-related KS variants 1-3 and 1-6. From the simple crystallography of the KS relationship, it is found that the three $\langle 100 \rangle_b$ directions for the KS 1-3 variant, say, x, y and z, become parallel to the following f.c.c. directions: x//$[(\sqrt{6}-2)/6, (\sqrt{6}+2)/6, 2/3]_f$, y//$[-1/6, -(2\sqrt{6}-1)/6, (\sqrt{6}+2)/6]_f$ and z//$[(2\sqrt{6}+1)/6, -1/6, (\sqrt{6}-2)/6]_f$. The Bain deformation $B_{1\text{-}3}$ for the 1-3 variant can be expressed on the x-y-z coordinate system as

$$B_{1-3} = \begin{pmatrix} \varepsilon_1 & 0 & 0 \\ 0 & \varepsilon_1 & 0 \\ 0 & 0 & \varepsilon_2 \end{pmatrix} \tag{2-1}$$

Using the lattice constants $a_f = 0.3562$nm (an extrapolated value [21]) and $a_b = 0.2862$nm of γ- and α-iron, respectively, the principal Bain strains can be obtained as $\varepsilon_1 = (\sqrt{2}\, a_b/a_f) - 1 = 0.136$ and $\varepsilon_2 = (a_b/a_f) - 1 = -0.197$.

When the angles between the stress axis and the x, y and z directions are denoted respectively as α_1, α_2 and α_3, the interaction energy $E_{1\text{-}3}$ per unit volume between the applied stress $\sigma (\sigma > 0$ for tension and $\sigma < 0$ for compression) and the Bain deformation is written from Eq. (2-1) as

$$E_{1\text{-}3} = -\sigma(\varepsilon_1 \cos^2\alpha_1 + \varepsilon_1 \cos^2\alpha_2 + \varepsilon_2 \cos^2\alpha_3)$$

Therefore, for the applied stress of a unit magnitude, we have

$$E_{1\text{-}3}{}^0 = E_{1\text{-}3}/|\sigma|$$

A similar calculation can also be applied to obtain $E_{1\text{-}6}{}^0$ for the 1-6 variant. Considering the fact that an α-iron particle is made of a twin-layered structure containing the variants 1-3 and 1-6 in equal amounts, we obtain the interaction energy E_I (per unit stress and unit volume) between the applied stress and the total shape deformation of the twinned (1-3, 1-6) particle as

$$E_I = (E_{1\text{-}3}{}^0 + E_{1\text{-}6}{}^0)/2 \tag{2-2}$$

Such a calculation of the interaction energy was performed for all the 12 different twin-paired α-iron particles for stress axes $[001]_f$ and $[419]_f$. The results are shown in Table 2-3. For [001] specimens, all the expected variants can be regarded as those belonging to the variants 1-1 to 1-6 because of the crystal symmetry mentioned previously. In Table 2-3, twin-related pairs with negative and positive E_I values are expected to be formed preferentially in tension and in compression, respectively.

From Table 2-3, it is found that all the observed twinned particles in tension have negative E_I

Table 2-3. Calculated E_I values in equation (2-2) for KS twin-related pairs which constitute α-iron particles. T and C indicate the observed pairs in tension and in compression, respectively.

Twin-related pair	[001] specimen		[419] specimen	
	E_I value	Observed pair	E_I value	Observed pair
1-1, 1-4	0.030	C	0.064	C
1-2, 1-5	0.030	C	0.002	
1-3, 1-6	-0.134	T	-0.102	T
2-1, 2-4			0.072	C
2-2, 2-5			0.025	
2-3, 2-6			-0.088	
3-1, 3-4			-0.011	
3-2, 3-5			0.001	
3-3, 3-6			-0.118	
4-1, 4-4			-0.014	
4-2, 4-5			-0.016	
4-3, 4-6			-0.114	

values and all the observed particles in compression have positive E_I values. Therefore, we can say that the stress effect on the shape deformation reasonably explains the experimental results. However, for the [419] specimens, although such twin pairs as (3-3, 3-6) ($E_I = -0.118$) and (4-3, 4-6) ($E_I = -0.114$) are expected to be formed more preferentially in tension than the observed (1-3, 1-6) ($E_I = -0.102$) pair, these pairs were not observed experimentally. This fact cannot be explained by the stress effect on the shape deformation.

Let us now consider the stress effect on the lattice change. For this purpose, the Bogers-Burgers mechanism [7] will be adopted in the present study. This mechanism considers that the Bain deformation to change the lattice from f.c.c. to b.c.c. is decomposed approximately into the combination of two $\{111\}\langle 211\rangle_f$-type shear systems. Higo *et al.* [8], Kato *et al.* [9-11] and Sato *et al.* [12] concluded that the observed stress-induced martensite variants in ferrous alloy single crystals could be explained excellently when the stress effect on the first $\{111\}\langle 211\rangle_f$ shear system was assumed to be critical. Therefore, the same idea will be adopted below.

Table 2-4 lists the first $\{111\}\langle 211\rangle_f$ shear systems of the Bogers-Burgers double-shear mechanism and their Schmid factors for the $[001]_f$ and $[419]_f$ stress axes for all the 24 KS variants. Since the $\{111\}\langle 211\rangle_f$ shear systems are unidirectional, the sign of the Schmid factors was assigned as negative when activated in tension and positive when activated in compression.

For the [001] specimen, since both 1-3 and 1-6 variants have a negative Schmid factor of –0.236, the preferential formation of the (1-3, 1-6) pair in tension can be explained. For compression, the variants 1-1 and 1-2 have a positive Schmid factor of 0.471. Therefore, the (1-1, 1-4) and (1-2, 1-5) pairs are expected to be more preferably formed than the (1-3, 1-6) pair. This is in agreement with the experimental result in Table 2-2.

For the [419] specimen, the (1-3, 1-6) pair should have the strongest effect of a tensile stress since the variant 1-6 has the largest absolute value of the Schmid factor, –0.433. This is again in agreement with the experimental result. It may appear that the (1-2, 1-5) pair should also be formed in tension since 1-5 has the same Schmid factor as 1-6. However, its twinned variant 1-2 is very unfavorable for the tensile stress with a large positive Schmid factor (0.433). On the other hand, the Schmid factor of 1-3 is zero. This difference in the Schmid factors for the twinned variants can explain the absence of the (1-2, 1-5) pair in the [419] specimen deformed in tension. A similar argument holds to explain the preferentially formed variants, (1-1, 1-4) and (2-1, 2-4) pairs, in compression.

As seen in the above discussion, both the stress effects on the shape deformation and on the lattice change can explain the experimental results of the preferentially formed variants reasonably.

Table 2-4. The first $\{111\}\langle 211\rangle_f$ shear system of the Bogers-Burgers mechanism for each KS variant and its Schmid factor.

Variant	Shear system	[001] specimen		[419] specimen	
		Schmid factor	Observed	Schmid factor	Observed
1-1	$(\bar{1}1\bar{1})[\bar{1}12]_f$	0.471	C	0.433	C
1-2	$(\bar{1}1\bar{1})[\bar{1}12]_f$	0.471	C	0.433	
1-3	$(\bar{1}1\bar{1})[21\bar{1}]_f$	-0.236	T	0	T
1-4	$(\bar{1}1\bar{1})[21\bar{1}]_f$	-0.236	C	0	C
1-5	$(\bar{1}1\bar{1})[\bar{1}2\bar{1}]_f$	-0.236	C	-0.433	
1-6	$(\bar{1}1\bar{1})[\bar{1}2\bar{1}]_f$	-0.236	T	-0.433	T
2-1	$(111)[11\bar{2}]_f$			0.438	C
2-2	$(111)[11\bar{2}]_f$			0.438	
2-3	$(111)[\bar{2}11]_f$			-0.067	
2-4	$(111)[\bar{2}11]_f$			-0.067	C
2-5	$(111)[1\bar{2}1]_f$			-0.370	
2-6	$(111)[1\bar{2}1]_f$			-0.370	
3-1	$(1\bar{1}\bar{1})[1\bar{1}2]_f$			0.303	
3-2	$(1\bar{1}\bar{1})[1\bar{1}2]_f$			0.303	
3-3	$(1\bar{1}\bar{1})[\bar{2}1\bar{1}]_f$			-0.260	
3-4	$(1\bar{1}\bar{1})[\bar{2}1\bar{1}]_f$			-0.260	
3-5	$(1\bar{1}\bar{1})[12\bar{1}]_f$			-0.043	
3-6	$(1\bar{1}\bar{1})[12\bar{1}]_f$			-0.043	
4-1	$(\bar{1}\bar{1}1)[\bar{1}\bar{1}2]_f$			0.221	
4-2	$(\bar{1}\bar{1}1)[\bar{1}\bar{1}2]_f$			0.221	
4-3	$(\bar{1}\bar{1}1)[2\bar{1}1]_f$			-0.154	
4-4	$(\bar{1}\bar{1}1)[2\bar{1}1]_f$			-0.154	
4-5	$(\bar{1}\bar{1}1)[\bar{1}21]_f$			-0.067	
4-6	$(\bar{1}\bar{1}1)[\bar{1}21]_f$			-0.067	

Therefore, it is not easy to draw a decisive conclusion as to which effect is in fact more critical. In retrospect, such a difficulty is the main reason why the stress effect on the martensitic transformations has not been clearly understood until now. We will see below that this long-lasting difficulty can be overcome for the first time in the present study.

2.4.2. Fraction of transformed particles

The transformation curves in Fig. 2-4 will be discussed on the basis of the E_I values and Schmid factors in the previous section. First, the E_I values in Table 2-3 show that the absolute values for the [001] specimens is much larger in tension (–0.134) than in compression (0.030). Therefore, if the E_I value determines the transformability, tensile deformation should induce more martensites than compressive deformation. This is in contradiction to the result in Fig. 2-4(a). For the [419] specimens, the largest absolute E_I values are for the (1-3, 1-6) pair (–0.102) in tension and the (2-1, 2-4) pair (0.072) in compression. Again in this case, tensile deformation should induce more martensites than compressive deformation. However, as seen in Fig. 2-4(b), no significant dependence of the fraction of transformed particles on the sense of deformation was found.

Secondly, let us consider the Schmid factors in Table 2-4. For the [001] specimens, the largest Schmid factor in tension (– 0.236) is just one-half of that in compression (0.471). Therefore, compressive deformation is expected to induce more martensites than tensile deformation. For the [419] specimens, on the other hand, since the largest Schmid factors in tension (– 0.433) and in compression (0.438) are nearly the same, no significant difference is expected in the amount of transformed particles. These expectations are in fact in excellent agreement with the experimental results. It can therefore be concluded that as far as the results in Fig. 2-4 is concerned, the stress effect on the lattice change must be considered more significant than that on the shape deformation.

For polycrystalline specimens in Fig. 2-4(c), an average or smeared-out stress effect on many crystal grains with various orientations appears. This means that the difference in the stress effect between tensile and compressive deformations appears statistically as the effect on the volume change component alone. Since the $\gamma \rightarrow \alpha$ transformation in the present iron particles accompanies the volume expansion of about 3.7%, tensile deformation should induce more martensites than compressive deformation. This is exactly what we have seen in Fig. 2-4(c).

From the above discussion, it becomes clear now that in order to consistently explain both the preferentially formed martensite variants and the fraction of transformed particles as a function of plastic strain, the stress effect on the lattice change (the Bain deformation) must be considered to be predominant. From a series of studies on ferrous alloy single crystals to investigate stress-induced

martensitic transformations [8-12], it has been found that although the shape of martensites (lath-like, needle-like, spherical, plate-like) vary significantly with the alloy systems, preferentially formed KS variants are the same if stress is applied along the same direction on the parent f.c.c. phase. This fact cannot be explained if the stress effect on the shape deformation is considered to be essential. On the contrary, since the f.c.c. to b.c.c. lattice deformation, *i.e.*, the Bain deformation, is common regardless of the shape of the martensites, the above experimental results can be understood reasonably through the stress effect on the lattice change.

As mentioned before, the $\{111\}\langle 211\rangle_f$ double-shear mechanism was proposed by Bogers and Burgers [7] to explain the experimental results on the preferential formation of stress-induced martensite variants in Fe-Ni alloy single crystals. Olsen and Jesser [22] examined the crystallography of the $\gamma \rightarrow \alpha$ martensitic transformation in iron thin films deposited on copper or nickel substrates. They concluded that the interaction between misfit stresses and the lattice change determined the iron film epitaxy on the f.c.c. substrates. Moreover, Miyaji *et al.* [23, 24] investigated the texture caused by the preferential formation of martensite variants by rolling of Fe-Ni alloy polycrystals. They also concluded that the stress effect on the lattice change was critical. Therefore, although the stress effect on the total shape deformation still appears to be more widely accepted, some investigators have supported the idea of the stress effect on the lattice change.

For martensitic transformations in bulk crystals, transforming regions are constrained by the surrounding parent phase. When a martensite crystal is formed in a parent phase, its lattice deformation (the Bain deformation) is certainly too large to be accommodated elastically. Therefore, additional plastic accommodation (by slip or twinning, lattice invariant deformation) occurs in a martensite to reduce as much as possible the amount of total shape deformation. The twinned microstructure in the present α-iron particles is considered to be formed as a result of the above plastic accommodation. When an applied stress helps the formation of a certain martensite variant (say, the variant KS 1-6) by assisting its lattice deformation, the lattice invariant deformation should occur so as to cancel the shape change caused by the formation of the above favorable variant. As a result, the transformation strains of the twinned variant (say, KS 1-3) are often those which are against the sense of the applied stress. Therefore, physics involved in the stress effect on the shape deformation is rather ambiguous since the overall shape deformation due to the formation of not only favorable (KS 1-6) but also unfavorable (KS 1-3) variants is considered.

On the contrary, the stress effect on the lattice change can be understood naturally such that the formation of a favorable variant (KS 1-6) is strongly promoted by the applied stress and its twinned variant (KS 1-3) is formed as a result of the plastic accommodation.

2.5. Summary and conclusions

The stress-induced $\gamma \rightarrow \alpha$ martensitic transformation in small iron particles in a single-crystal copper matrix was investigated and the following results and conclusions were obtained.

(1) Depending on the direction ($[001]_f$ or $[419]_f$) and sense (tension or compression) of the applied stress, specific Kurdjumov-Sachs martensite variants out of crystallographically equivalent ones were formed preferentially.

(2) The fraction of transformed particles was examined as a function of plastic strain for specimens deformed at room temperature. When comparison is made at the same amount of plastic shear strain, compressive deformation was found to induce more martensites than tensile deformation for specimens deformed along $[001]_f$. On the other hand, for specimens deformed along $[419]_f$, no significant difference was found between tesile and compressive deformations. When polycrystalline specimens were used for this experiment, tensile deformation induced more martensites than compressive deformation.

(3) The above experimetal results can be explained reasonably and consistently if the applied stress is considered to play an important role in the $\gamma \rightarrow \alpha$ lattice change (the Bain deformation) in the early stage of the martensitic transformation.

References

[1] J. R. Patel and M. Cohen: *Acta Metall.*, **1** (1953), 531.

[2] A. J. Bogers: *Acta Metall.*, **10** (1962), 260.

[3] G. Stone and G. Thomas: *Met. Trans.*, **5** (1974), 2095.

[4] D. Goodchild, W. T. Roberts and D. V. Wilson: *Acta Metall.*, **18** (1970), 1137.

[5] G. F. Bolling and R. H. Richman: *Scripta Metall.*, **4** (1970),539.

[6] H. Onodera, H. Goto and I. Tamura: *Proc. 1st JIM Int'l Symp. on New Aspects of Martensitic Transformation*, The Japan Institute of Metals, (1976), 327.

[7] A. J. Bogers and W. G. Burgeres: *Acta Metall.*, **12** (1964), 255.

[8] Y. Higo, F. Lecroisey and T. Mori: *Acta Metall.*, **22** (1974), 313

[9] M. Kato and T. Mori: *Acta Metall.*, **24** (1976), 853.

[10] M. Kato and T. Mori: *Acta Metall.*, **25** (1977), 951.

[11] M. Kato, R. Monzen and T. Mori: *Acta Metall.*, **26** (1978), 605.

[12] A. Sato, M. Kato, Y. Sunaga, T. Miyazaki and T. Mori: *Acta Metall.*, **28** (1980), 367.

[13] M. S. Wechsler, D. S. Lieberman and T. A. Read: *Trans. AIME*, **197** (1953), 1503.

[14] J. S. Bowles and J. K. Mackenzie: *Acta Metall.*, **2** (1954), 129, 138, 224.

[15] J. B. Newkirk: *Trans. AIME*, **209** (1957), 1214.

[16] K. R. Kinsman, J. W. Sprys and R. J. Asaro: *Acta Metall.*, **23** (1975), 1431.

[17] E. S. Machhlin and M. Cohen: *Trans. AIME*, **191** (1951), 746.

[18] T. Saburi, S. Nenno, S. Kato and K. Takata: *J. Less-Common Metals*, **50** (1976), 223.

[19] H. Zijlstra: *Experimental Methods in Magnetism 1*, North-Holland, Amsterdam, (1967), p.145.

[20] R. Monzen, A. Sato and T. Mori: *Trans. JIM*, **22** (1981), 65.

[21] Z. S. Basinski, W. Hume-Rotherly, F. Rio and A. L. Sutton: *Proc. Roy.Soc.*, **A229** (1955), 459.

[22] G. H. Olsen and W. A. Jesser: *Acta Metall.*, **19** (1971), 1009, 1299.

[23] H. Miyaji, M. Nobuki, N. Sakuma, T. Mitsui, H. Nakajima and E. Furubayashi: *Proc. Int'l Conf. on Physical Metallurgy of Thermomechanical Processing of Steels and Other Metals*, The Iron and Steel Institute of Japan, **2** (1988), 815.

[24] H. Miyaji and E. Furubayashi: *Textures and Microstructures*, **12** (1990), 189.

Chapter 3.

Growth of α-Iron Particles in a Copper Matrix

3.1. Introduction

As mentioned in Chapter 1, when a solution-treated Cu-Fe alloy is aged, coherent γ-iron(f.c.c.) particles are formed in a copper matrix. Matsuura, Kitamura and Watanabe [1] have examined the growth and coarsening of γ-iron particles and estimated the γ-Fe/Cu interfacial energy using the Lifshitz-Slyozov-Wagner (LSW) [2, 3] theory of Ostwald ripening. On the other hand, Speich and Oriani [4] have examined the growth and coarsening of copper particles in an α-iron matrix and indirectly estimated the α-Fe/Cu interfacial energy. However, the growth and coarsening of incoherent α-iron particles in copper has not been examined. Consequently, the α-Fe/Cu interfacial energy has not been obtained directly by an experiment. Furthermore, the morphology of the α-iron particles after long annealing has not been examined in detail. In this study, the growth and coarsening of the α-iron particles in copper will be investigated and the α-Fe/Cu interfacial energy will be evaluated using the LSW theory.

Previous studies adopted alloy systems where a single type of precipitates exists. Thus, a single value of the interfacial energy could be assumed between a matrix and precipitates. Similarly, the shape of precipitates was uniform. Thus, the growth rate was constant and the normalized particle size distribution was independent of aging time as predicted by the LSW and modified LSW [5-10] theories. In a Cu-Fe alloy, a suitable combination of heat treatment and straining results in the coexistence of two types of particles; γ- and α-iron particles. In addition to the growth among the same type of particles, the solute transfer between the γ- and α-iron particles occurs. It is expected that this mixed-mode growth leads to a size distribution different from the usual one. The present study also examines this mixed-mode growth. It will be shown how particle growth and coarsening can be explained when two types of precipitates with different interfacial energies coexist.

In order to use the LSW theory to analyze the experimental results, it is necessary to clearly understand the physics and implications of the theory. Historically speaking, the diffusional growth and diminution of precipitated particles in a solid matrix, generally known as Ostwald ripening, was first considered by Greenwood [11]. Subsequently, LSW [2, 3] analyzed the problem more rigorously. It is now established that when there is a distribution in particle sizes, particles larger than the average size grow and the remainder shrink and eventually dissolve. The rate of

particle growth depends on the dimension of diffusion. If diffusion is three dimensional (3D), it is well known that the cube of the average particle radius increases linearly with time. On the other hand, for 2D diffusion, as in the case of the growth of grain boundary particles controlled by boundary diffusion, Speight has shown that the fourth power of the average particle radius varies linearly with time [12].

To derive these rate equations, the following Gibbs-Thomson-Freundlich equation has commonly been adopted as a starting point

$$C_r = C\exp(2\Gamma\Omega / rkT) \qquad (3\text{-}1)$$

where C_r is the concentration (number of atoms per unit volume) of solute atoms immediately adjacent to a spherical particle of radius r, C is the solute concentration in equilibrium with an infinitely large particle, Γ is the interfacial free energy per unit area of the particle/matrix interface, Ω is the atomic volume of a solute atom and kT has its usual meaning. From Eq. (3-1), it is found that the solute concentration near a large particle is smaller than that near a small particle. Therefore, in accordance with Fick's first law, solute atoms flow from the small particle to the large particle. As a result, large particles grow and small particles dissolve.

Although the Gibbs-Thomson-Freundlich equation is thermodynamically sound, it may not necessarily be easy to draw an intuitively understandable image of what is physically going on during the particle growth process. The driving force of the Ostwald ripening is, of course, the reduction of total surface free energy (and, therefore, the total surface area) of the particles. Then, it should be much easier to understand the physics involved in the growth process if the reduction in the total surface area is explicitly expressed in the analysis of deriving rate equations. Therefore, as a theoretical phase of the present study, a new derivation method which is not only simpler but also much easier to grasp the physical meaning of the Ostwald ripening processes will first be proposed.

3.2. Derivation of fundametal rate equations for Ostwald ripening

Let us consider the usual 3D problem. Suppose spherical particles of average radius $\bar{r}$ and average inter-particle separation L exist in a solid matrix. Interfacial diffusion around the periphery of the particles are assumed to be much easier than volume diffusion so that the particles always remain spherical in shape. The average number of particles at distance about L from a particular particle is denoted as N. If particles are arranged in the matrix in an ideally close-packed fashion, N

becomes 12.

We will pay our attention to a particular particle of radius r which is slightly larger than the average radius $\bar{r}$, as shown in Fig. 3-1. Recalling the self-consistent method which is often adopted in statistical physics, we can reasonably assume that there are N nearest-neighbor particles of radius $\bar{r}$ at equal distance L from the center particle. Since each of the N nearest-neighbor particles should also have N surrounding particles in itself, one-Nth of the total flow of atoms from each of these N particles contributes to the growth of the center particle. Therefore, from the conservation of the total volume V_T of the contributing particles, we have

$$dV_T = 4\pi r^2 dr + (1/N)\times N\times 4\pi \bar{r}^2 d\bar{r} = 0$$

or

$$r^2 dr + \bar{r}^2 d\bar{r} = 0 . \tag{3-2}$$

The change in the surface free energy dF of the particles when the center particle grow by dr (> 0) and the surrounding particles by $d\bar{r}$ (< 0) is written as

$$dF = 8\pi\Gamma(r dr + \bar{r} d\bar{r}) = 8\pi\Gamma r^2 dr\left(\frac{1}{r} - \frac{1}{\bar{r}}\right). \tag{3-3}$$

Here, to obtain the last expression, Eq.(3-2) was used. If the above change is brought about by the flow of dn solute atoms from the surrounding N particles to the center particle,

$$4\pi r^2 dr = \Omega dn \tag{3-4}$$

must be satisfied. From Eqs.(3-3) and (3-4), we obtain

$$dF = 2\Gamma\Omega dn\left(\frac{1}{r} - \frac{1}{\bar{r}}\right). \tag{3-5}$$

The diffusional flow of solute atoms shown by the arrows in Fig. 3-1 is regarded as a 3D radial flow. At the steady state, let $v(x)$ be the average velocity of solute atoms at distance x $(0 \le x \le L)$ from the center particle. The total volume of solute atoms Ωdn moving through an imaginary spherical wall of radius $r + x$ (Fig. 3-1) during a time interval dt is expressed as

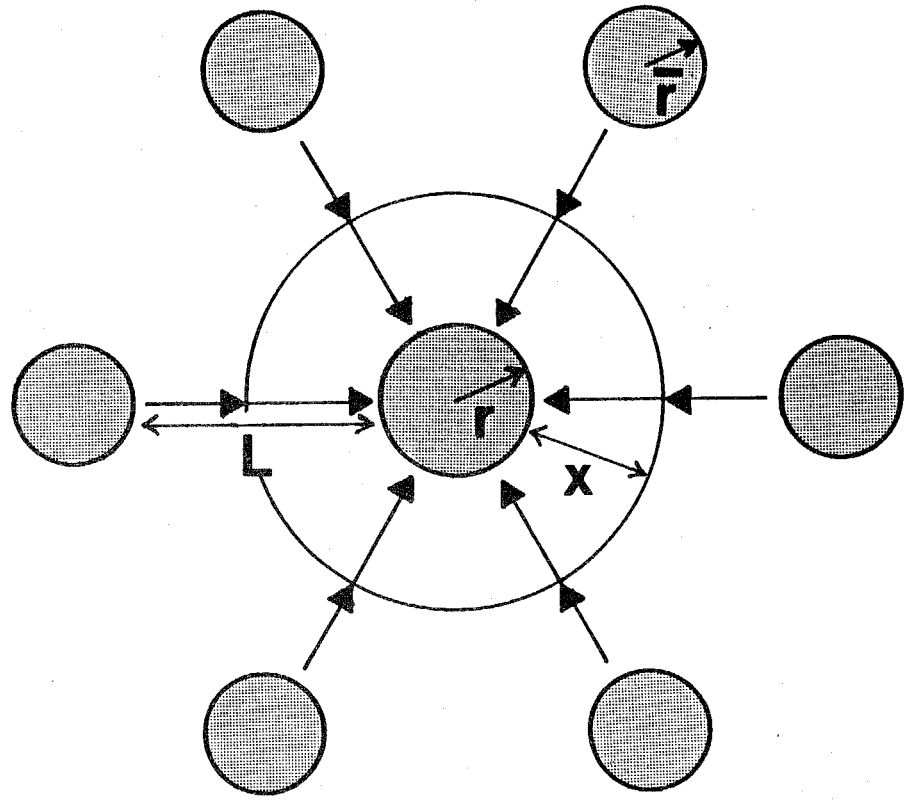

Fig. 3-1. Growth of a particle of radius r by the diffusional flow of solute atoms from the surrounding particles of radius $\bar{r}$.

$$\Omega \mathrm{d}n = 4\pi(r + x)^2 C\Omega v(x)\mathrm{d}t \qquad (3\text{-}6)$$

where the concentration of solute atoms is approximated as the equilibrium one and the factor $C\Omega$ is the volume fraction of solute atoms in the matrix. Since there is no sink or source of the atom flow other than the particle surfaces, Ωdn should not depend on x. Therefore, we have

$$4\pi(r + x)^2 C\Omega v(x) = \text{constant.}$$

From this, we find that $v(x)$ must have the following form:

$$v(x) = A / (r + x)^2 , \qquad (A\text{: a constant}) . \qquad (3\text{-}7)$$

From Einstein's equation, the average force $f(x)$ acting on a flowing solute atom can be defined as

$$f(x) = kTv(x) / D_v \qquad (3\text{-}8)$$

where D_v is the bulk diffusion coefficient of solute atoms. On the other hand, $f(x)$ is also defined as the gradient of the chemical potential μ (= dF/dn):

$$f(x) = -\,\mathrm{d}\mu / \mathrm{d}x = -\,\mathrm{d}^2F / \mathrm{d}n\mathrm{d}x. \qquad (3\text{-}9)$$

From Eqs. (3-7) to (3-9), we have

$$\mathrm{d}^2F = -\frac{AkT\,\mathrm{d}n}{D_V}\frac{\mathrm{d}x}{(r+x)^2} . \qquad (3\text{-}10)$$

Intergating Eq. (3-10) from $x = 0$ to $x = L$, and assuming for simplicity that L is much larger than r, we obtain

$$\mathrm{d}F = -\frac{AkT\,\mathrm{d}n}{D_V r} . \qquad (3\text{-}11)$$

Since Eqs. (3-5) and (3-11) must be the same,

$$A = \frac{2D_V \Gamma \Omega r}{kT}\left(\frac{1}{\bar{r}} - \frac{1}{r}\right) \tag{3-12}$$

is obtained. Substitution of Eq. (3-12) into Eq. (3-7) yields

$$v(x) = \frac{2D_V \Gamma \Omega r}{kT(r+x)^2}\left(\frac{1}{\bar{r}} - \frac{1}{r}\right). \tag{3-13}$$

From Eq. (3-6), the atom flow at the surface ($x = 0$) of the center particle should satisfy

$$\Omega \mathrm{d}n = 4\pi r^2 C \Omega v(0) \mathrm{d}t. \tag{3-14}$$

Combining Eqs. (3-13) and (3-14), we have

$$\frac{\mathrm{d}n}{\mathrm{d}t} = \frac{8\pi D_V \Gamma \Omega C r}{kT}\left(\frac{1}{\bar{r}} - \frac{1}{r}\right). \tag{3-15}$$

Therefore, we finally obtain the rate equation of the particle growth from Eqs. (3-4) and (3-15):

$$\frac{\mathrm{d}r}{\mathrm{d}t} = \frac{\mathrm{d}r}{\mathrm{d}n} \times \frac{\mathrm{d}n}{\mathrm{d}t} = \frac{2D_V \Gamma \Omega^2 C}{kT}\left(\frac{1}{r\bar{r}} - \frac{1}{r^2}\right). \tag{3-16}$$

It is delightful to know that this equation is identical to that derived by LSW [2, 3], as Voorhees and Schaefer [13] have shown.

The same analysis can be repeated to treat the case of a 2D problem. Although details will not be shown, from the consideration of a 2D radial flow as mentioned in Ref. [14], the growth rate of grain-boundary particles controlled by 2D grain-boundary diffusion can be obtained as

$$\frac{\mathrm{d}r}{\mathrm{d}t} = \frac{D_b W \Gamma \Omega^2 C}{kT \ln(L/r)}\left(\frac{1}{r^2\bar{r}} - \frac{1}{r^3}\right) \tag{3-17}$$

where D_b is the grain-boundary diffusion coefficient of solute atoms and W is the boundary thickness. Aside from numerical factors, Eq.(3-17) is again the same as that derived by Speight [12] using the Gibbs-Thomson-Freundlich equation. It can be shown [2, 3, 12] that the integration of Eqs. (3-16) and (3-17) results in the relationships $\bar{r}^3 \propto t$ and $\bar{r}^4 \propto t$, respectively. Now that the fundamental rate equations have been derived and the physics involved in the theories of the Ostwald ripening has become very clear, the resultant rate equations will be used to analyze the

results of the experimental phase of the present study.

3.3. Experimental

Single crystals of a Cu-1.06mass%Fe alloy were grown by the Bridgman method with a seed. Tensile specimens, 3×3×40 mm^3, with the $[419]_f$ stress axis were cut from the single crystals. These specimens were solution treated at 1273K in a vacuum for 4h, quenched into water, and aged at 973K for 1 day. After these treatments, γ-iron particles with the average radius of 29 nm were obtained.

The specimens were strained at 77K by either 5 or 20 % to induce the γ→α martensitic transformation in the iron particles. The 5 % straining caused the transformation in approximately 10 % of the iron particles, while the 20% straining led to the transformation in all the particles. The strained specimens were annealed at 973K between 30 min and 4 d and sliced parallel to the primary slip plane, $(\bar{1}1\bar{1})_{Cu}$, to form disks. Thin foils were prepared from the disks by the jet polishing technique using a nitric acid solution. The γ-iron and α-iron particles were observed on an electron microscope, Hitachi H-700, equipped with a 60° tilt goniometer, under an accelerating voltage of 200 kV.

3.4. Results and Discussion

3.4.1. Growth of α-iron particles

Figure 3-2 shows the growth of the α-iron particles during annealing at 973K after 20% straining. One can see in Fig. 3-2 that most of the α-iron particles elongate along $[110]_{Cu}$ as the particles become larger. Only a few particles grow along other $\langle 110\rangle_{Cu}$ directions. The diffraction analysis showed that the α-iron particles which are elongated along $[110]_{Cu}$ satisfied nearly the KS orientation relationship,

$$(\bar{1}1\bar{1})_{Cu} // (110)_{Fe}\ ,\ [\bar{1}\bar{1}0]_{Cu} // [\bar{1}1\bar{1}]_{Fe}$$
and $$(\bar{1}1\bar{1})_{Cu} // (110)_{Fe}\ ,\ [110]_{Cu} // [\bar{1}11]_{Fe},$$

to the copper matrix. These are the variants 1-3 and 1-6, respectively, in Chapter 2. The mean aspect ratio of the major to the minor axis, *a*/*b*, of the α-iron particles is plotted against annealing time in Fig. 3-3.

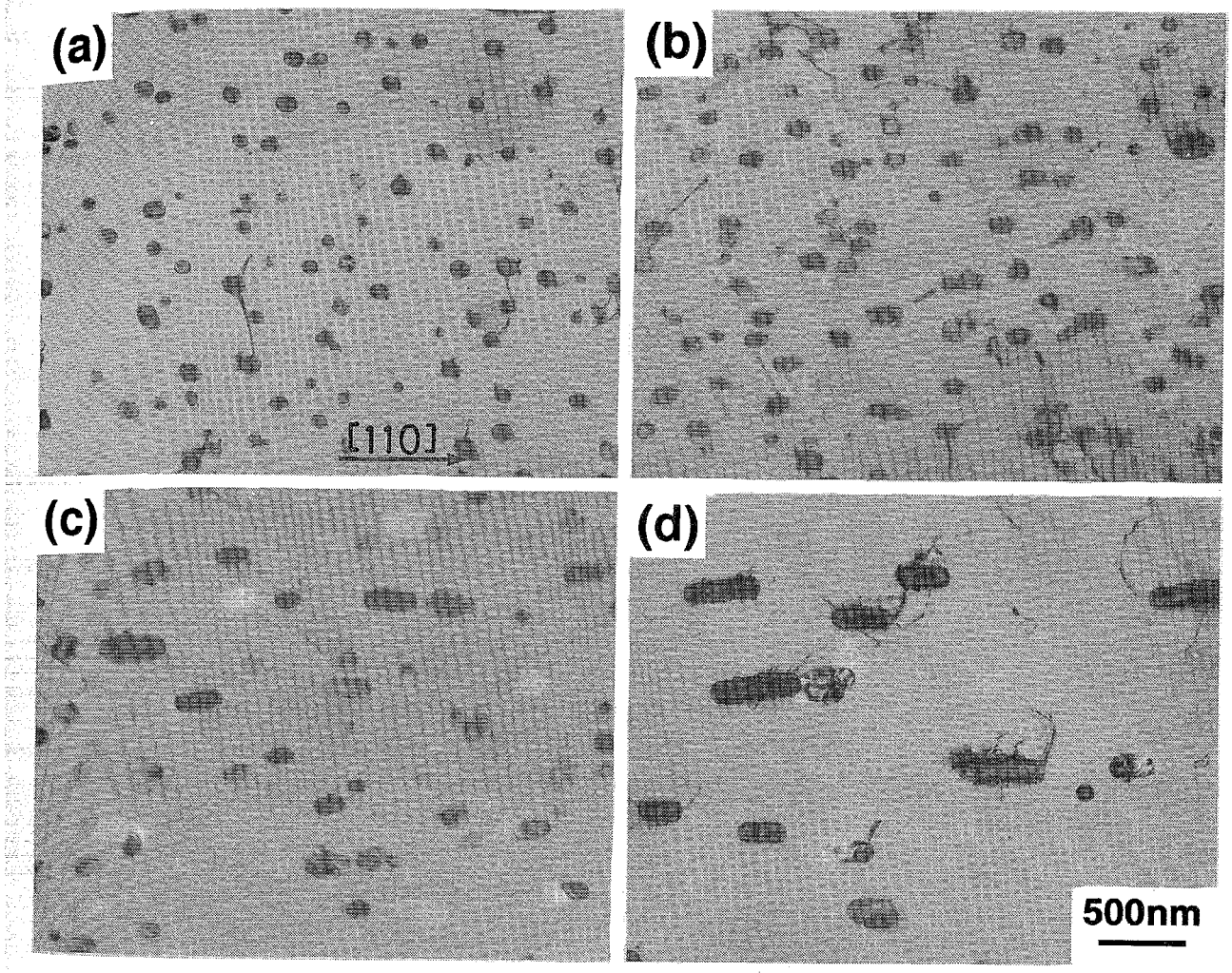

Fig. 3-2. Transmission electron micrographs of α-iron particles in a Cu-Fe alloy annealed at 973K for (a) 2h, (b) 8h, (c) 1d and (d) 2d. Before the annealing treatments, the specimens were aged at 973K for 1d and deformed by 20% in tension. The foil surface is parallel to the $(\bar{1}1\bar{1})$ primary slip plane of the copper matrix. Note that the α-iron particles elongate along [110] by annealing.

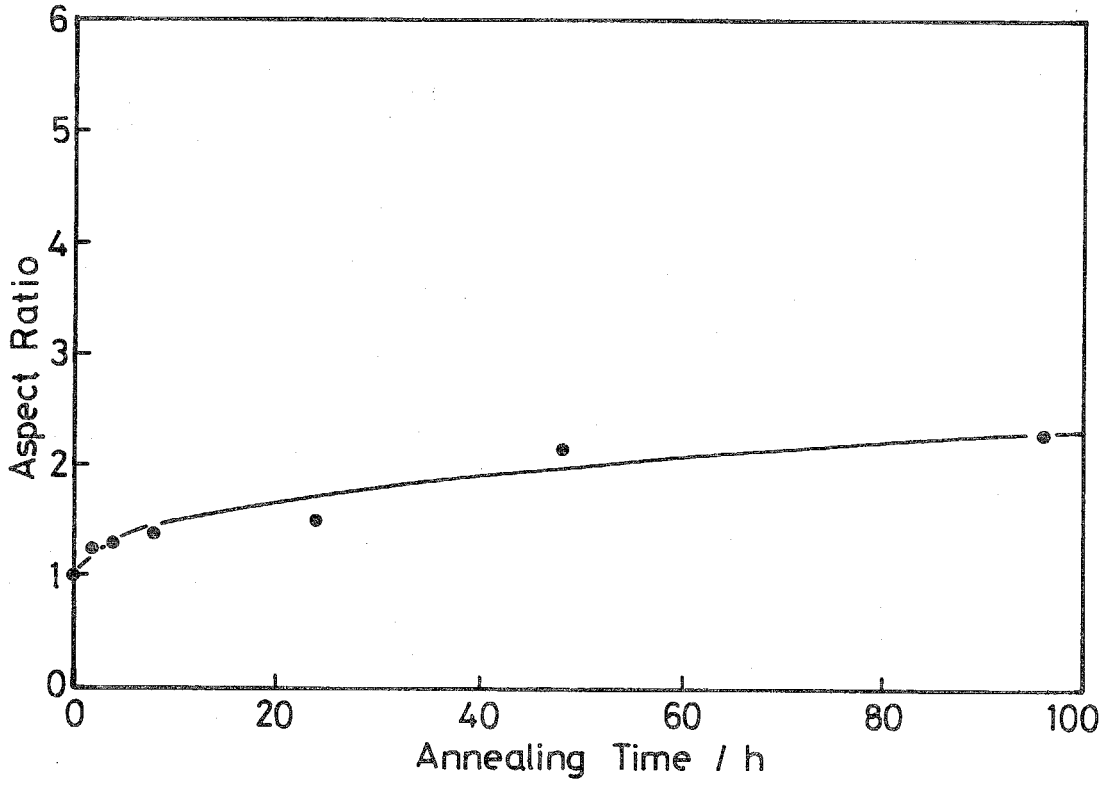

Fig. 3-3. Change in the mean aspect ratio of the α-iron particles in a 20% deformed specimen with annealing time.

The mean aspect ratio increases rapidly at the early stage of annealing and then slowly at the later stage. For simplicity, the shape of the γ-iron particles is assumed to be spheroidal described in the x-y-z coordinates by $x^2/a^2 + (y^2 + z^2) / b^2 \leq 1$. Further, the assumed spheroid is reduced to a sphere which has the same volume as the spheroid. The average volume of the particles is plotted against annealing time t in Fig. 3-4. Here, in order to conform to the usual plot, the ordinate is taken as $\bar{r}^3 - \bar{r}_0^3$. $\bar{r}$ is the average radius of the reduced sphere and $\bar{r}_0$ is that at the beginning of annealing. For comparison, the data of γ-iron particles obtained from unstrained specimens are also shown in Fig. 3-4. Similar to the study by Matsuura *et al.* [1], a good linearity between $(\bar{r}^3 - \bar{r}_0^3)$ and t is observed for the γ-iron particles, in agreement with the LSW theory. On the other hand, the strict linearity is absent in the growth of the α-iron particles. However, in the later stage of annealing, a good linearity is satisfied.

In order to obtain a rough value of the interfacial energy between α-iron and copper, the $(\bar{r}^3 - \bar{r}_0^3)$ - t curve of the α-iron particles was approximated by a straight line with the least-square method, as indicated by the dotted line.

The standard equations of the LSW theory of the Ostwald ripening has been obtained by the integration of Eq. (3-16) considering the statistical distribution of the particle size as [2, 3]

$$\bar{r}^3 - \bar{r}_0^3 = K(t - t_0), \tag{3-18}$$

where

$$K = 8\Gamma D_v C V_m^2 / 9RT. \tag{3-19}$$

Here, Ω^2/kT in Eq. (3-16) is rewritten as V_m^2/RT with V_m the molar volume of iron and R the gas constant. The values of some of these parameters are given in Table 3-1. From the slope of the straight lines in Fig. 3-4, K and thus Γ can be obtained. The straight line for the γ-iron particles in Fig. 3-4 results in 0.22J/m^2 as the γ-Fe/Cu interfacial energy Γ_γ. This is in exact agreement with the result obtained by Matsuura *et al.* [1]. The approximately drawn straight line for the α-iron particles in Fig. 3-4 gives 3.3J/m^2 as the α-Fe/Cu interfacial energy Γ_α. It is about fifteen (15) times as large as Γ_γ. Since the α-Fe/Cu interface is incoherent, the larger value of Γ_α is reasonably accepted.

In the analysis of the growth of copper precipitates in α-iron, Speich and Oriani assumed 0.5J/m^2 as Γ_α, using some reported values of the surface and grain boundary energies of copper.

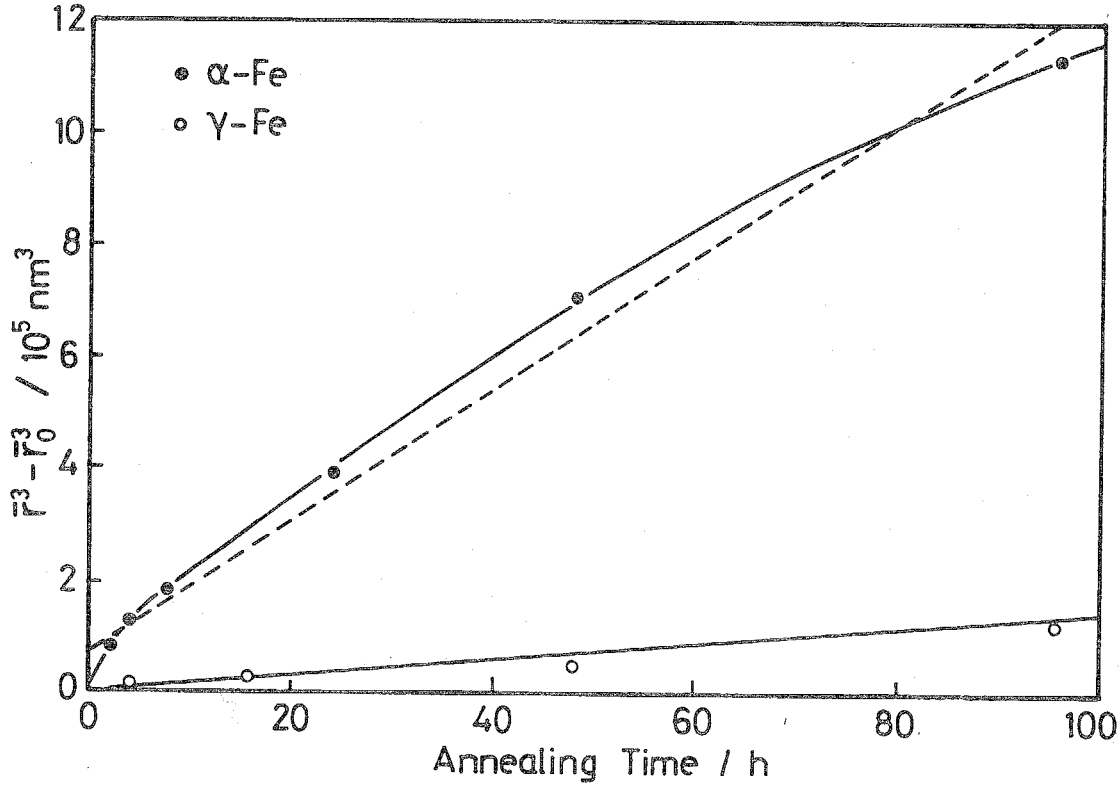

Fig. 3-4. Growth curves of the α-iron particles in a 20% deformed specimen and of the γ-iron particles in a nondeformed specimen. The straight lines were obtained by the least-square method.

Table 3-1. Numerical values used for the estimation of the interfacial energies between copper and iron particles.

Interface	T (K)	$D_v \times 10^6$ (m^2/s)	C (mol/m^3)	$K \times 10^{28}$ (m^3/s)	Γ (J/m^2)
γ-Fe/Cu	973	*3.68	**800	3.55	0.22
α-Fe/Cu	973	*3.68	***480	32.3	3.3

*[16], **[17], ***[18]

They found that the observed growth rate of the copper particles was much larger, approximately by a factor of eight (8), than that predicted by Eqs. (3-18) and (3-19) with $\Gamma_\alpha = 0.5 J/m^2$. If the present value of $\Gamma_\alpha = 3.3 J/m^2$ were used, better agreement would have been obtained between the theory and the experiment.

Of course, the above determined Γ_α is an average quantity. Since the crystal structure of α-iron differs from that of copper, the specific interfacial energy must depend on the orientation of the interface surrounding an α-iron particle, *i.e.*, anisotropy in the interfacial energy. The elongated shape along $[110]_{Cu}$ of the α-iron particles after prolonged annealing shows the existence of the anisotropy. That is, a particle takes a shape with which the total interfacial energy becomes smaller than that achieved when it would take a spherical shape with the identical volume. Then, the driving force for the growth, the decrease in the total interfacial energy, becomes smaller as the particles become larger. This qualitatively explains the convex shape of the $(\bar{r}^3 - \bar{r}_0^3)$ vs t curve for the α-iron particles in Fig. 3-4. The observed rapid growth rate with the rate constant $K_\alpha^e = 9.80 \times 10^{-27}$ m^3/s in the early stage of the annealing can also be explained. The copper matrix can dissolve less iron atoms when it coexists with α-iron particles than with γ-iron particles [17, 18]. Therefore, during the early stage of the annealing after the γ→α martensitic transformation in the particles, supersaturated iron atoms in the copper matrix tend to be captured by the α-iron particles. This would enhance the growth of the α-iron particles. Considering the fact that the solute concentration at the α-Fe/Cu interface is not in equlibrium at the ealier stage of the annealing, it may be better to estimate the interfacial energy using only the data obtained in the later stage of the annealing. The value of $\Gamma_\alpha = 3.0 J/m^2$ is obtained from the data for annealing longer than 8h.

The above observations suggest that the self-similarity predicted by the LSW theory is not obeyed in the α-Fe/Cu system. Figure 3-5 shows the change in the size distribution of the α-iron particles with annealing. The distribution becomes broader as the annealing proceeds, that is, the self-similarity is not strictly satisfied. This point is more clearly shown, using the standard deviation of the size distribution, in Fig. 3-6. This result might appear to contradict the observation that the growth rate of the α-iron particles decreases after longer annealing.

The growth rate constant K is also given by [9]

$$K = A \lim_{\rho \to \infty} \left\{ P_0(\rho) / \rho^2 \right\}, \qquad (3\text{-}20)$$

where A is a constant, ρ the normalized particle radius $(r / \bar{r})$ and $P_0(\rho)$ is the scaled size distribution function. The LSW theory can be applied very well when $P_0(\rho)$ is time independent. On the

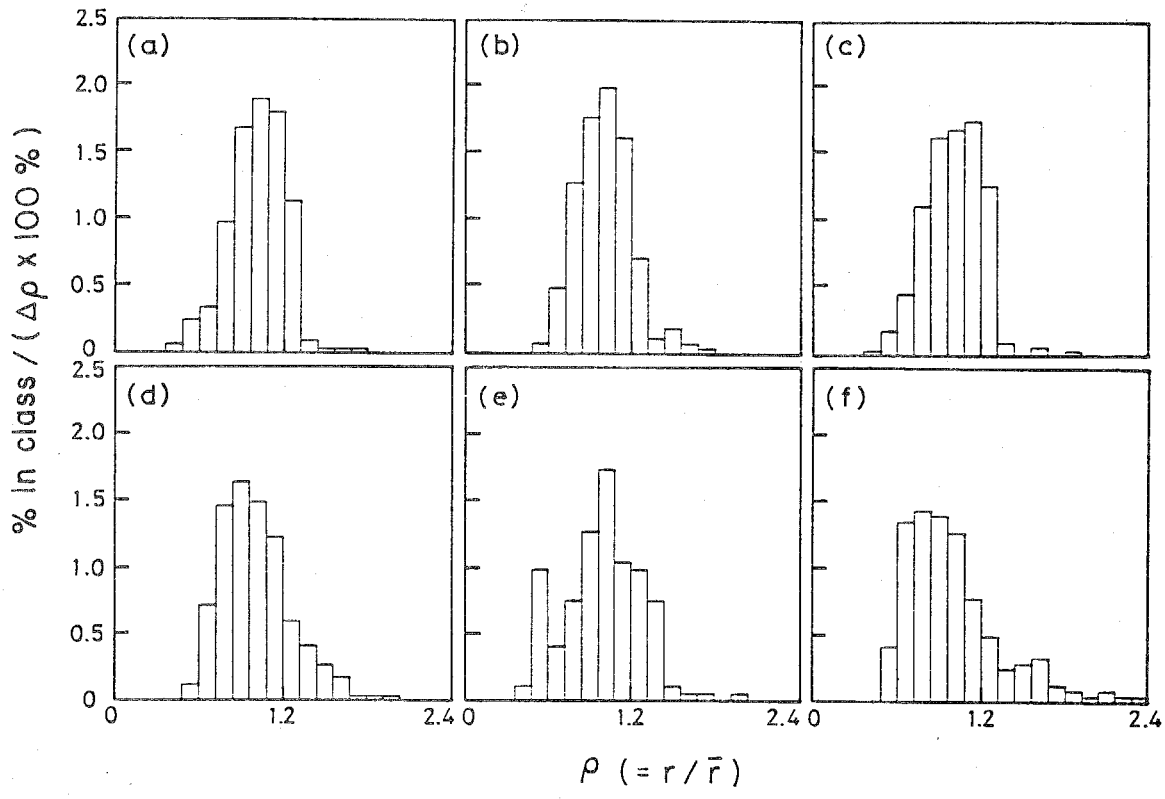

Fig. 3-5. Change in the size distribution of the α-iron particles in a 20 % deformed specimen with annealing time; (a) 2h, (b) 4h, (c) 8h, (d) 1d, (e) 2d and (f) 4d.

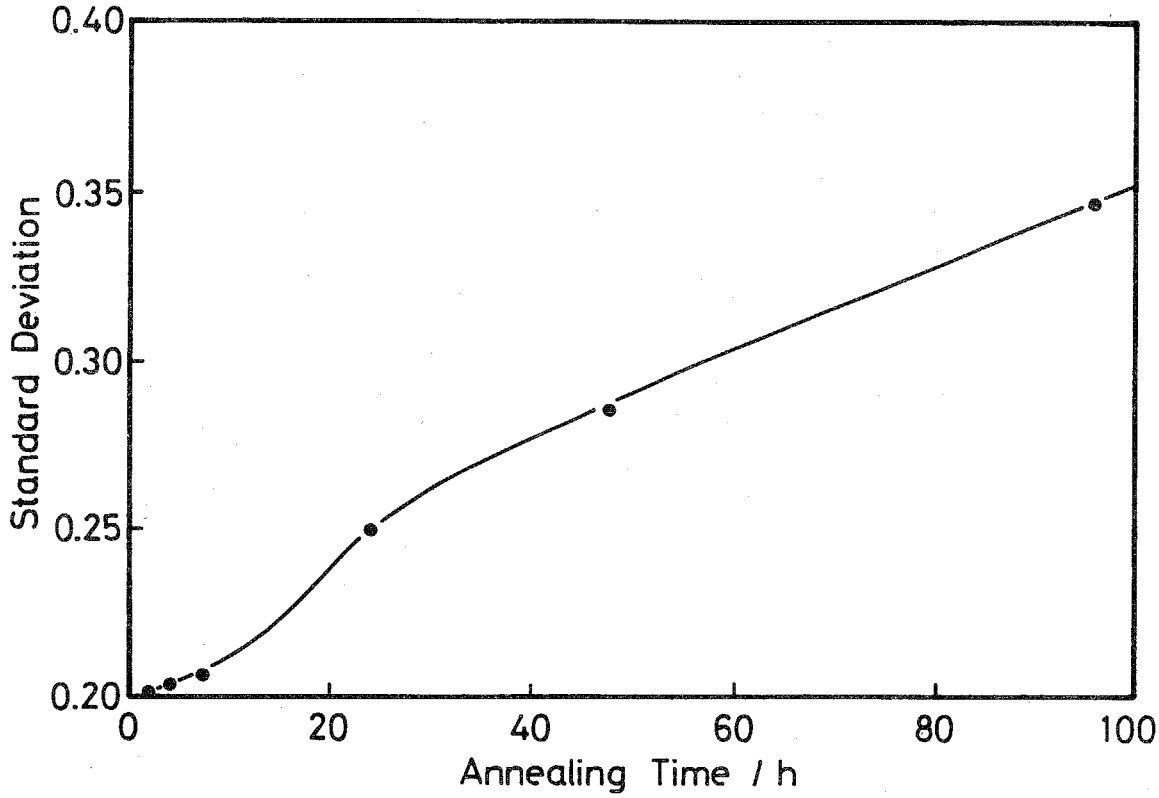

Fig. 3-6. Change in the standard deviation of the size distribution shown in Fig. 3-5 with annealing time.

contrary, Figure 3-6 shows that the time independence of P_0 (ρ) does not hold. The result in Fig. 3-6 can be understood by examining the change in the aspect ratio of the α-iron particles with annealing. Figure 3-7 shows the relation between the aspect ratio and the normalized particle radius. As seen in Fig. 3-7(a), the aspect ratio is confined in the narrow range irrespective of the normalized size during shorter annealing time. After longer annealing, however, the aspect ratio for the particles larger than the average size becomes larger, accompanying a large scatter, Fig. 3-7(b). From these results we can see the reason for the broadening of the particle size distribution by long time annealing. Some larger particles grow preferentially and increase their aspect ratios.

The essential cause for this behavior is the existence of the anisotropy of the specific interfacial energy. On the other hand, the growth rate of the particles with the average size decreases with annealing. Thus, in an overall aspect, the growth of the α-iron particles shows a tendency different from that predicted by the LSW theory.

3.4.2. Mixed-mode growth of α- and γ-iron particles

The mixed-mode growth was examined using specimens strained by 5%. Figure 3-8 shows the α- and γ-iron particles observed on annealing after the straining. Similar to the case where only the α-iron particles are present, the α-iron particles grow with annealing. On the contrary, the γ-iron particles dissolve back into the solution. They completely disappear after 1 day annealing, as seen in Fig. 3-8(d). This is quantitatively shown in Fig. 3-9 where the fraction of the α-iron particles to the whole particles is shown against annealing time.

The size distribution of the α- and γ-iron particles is also shown in Fig. 3-10. It can be seen that the growth of the α-iron particles which are primarily larger than the average-sized particles and constitute 10% of all the particles was compensated for by the dissolution of some of the γ-iron particles. The particle size distribution changes with annealing.

The average radius of the combined α- and γ-iron particles is plotted against annealing time in Fig. 3-11, in a similar manner to Fig. 3-4. Here, α- and γ-iron particles were not discriminated. The $(\bar{r}^3 - \bar{r}_0^3)$ vs t relation is not linear. Thus, the LSW theory cannot be used in its original form.

The growth rates of the α- and γ-iron particles were examined separately. The average radius of the α-iron particles and that of the γ-iron particles are shown against the annealing time in Fig. 3-12. Using the early-stage annealing data in Fig. 3-12, an attempt was made to evaluate the initial growth rate of γ-iron particles in the specimen for the mixed-mode growth. Surprisingly, the rate constant became $K_\gamma^e = 6.38\times10^{-27}$ m^3/s, which is much larger than $K_\gamma = 0.36\times10^{-27}$ m^3/s obtained from the straight line for γ-iron particles in Fig. 3-4 and naturally smaller than K_α^e

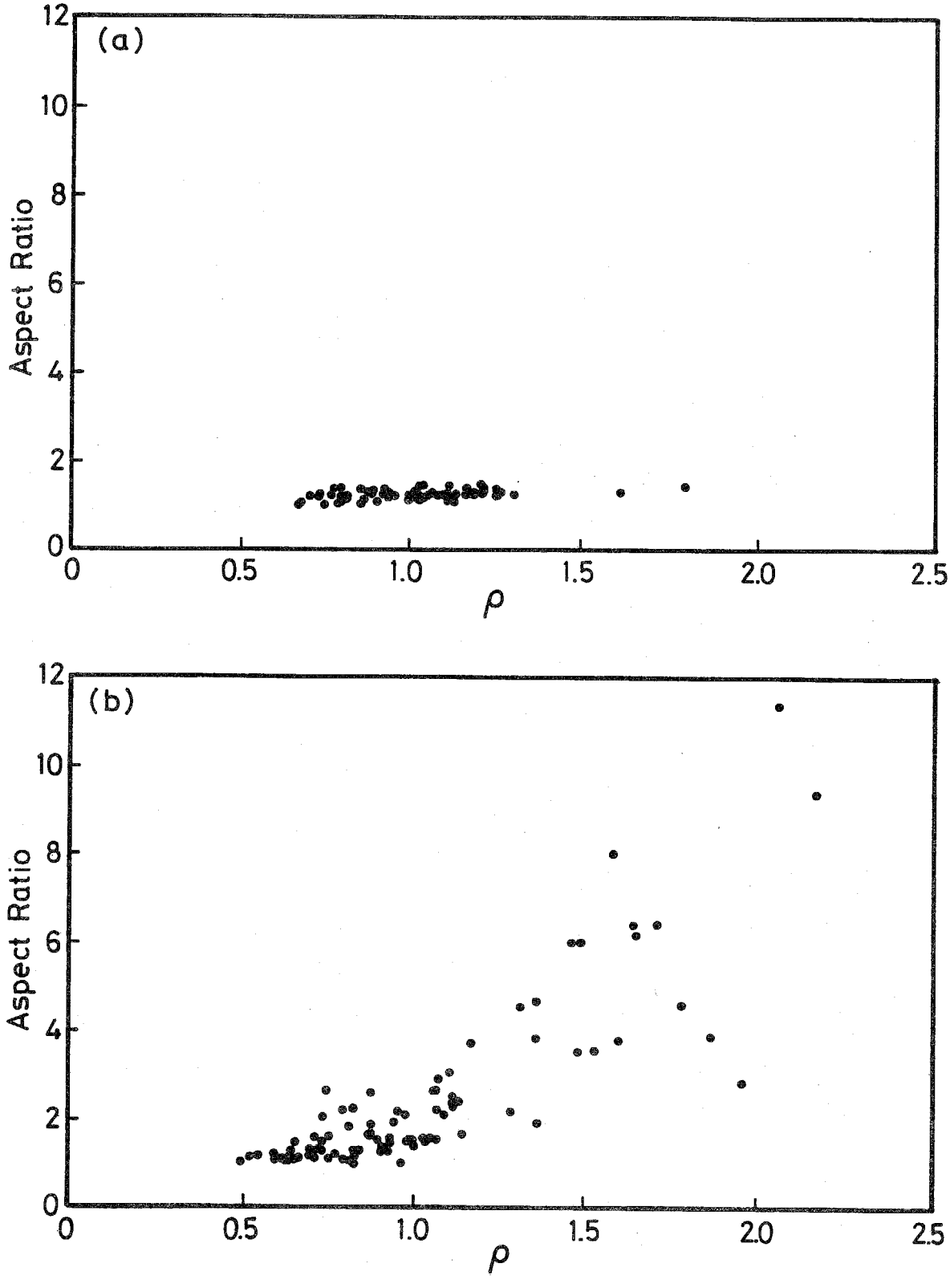

Fig. 3-7. Relationship between the aspect ratio and the normalized radius of the α-iron particles in specimens annealed at 973K for (a) 2h and (b) 4d.

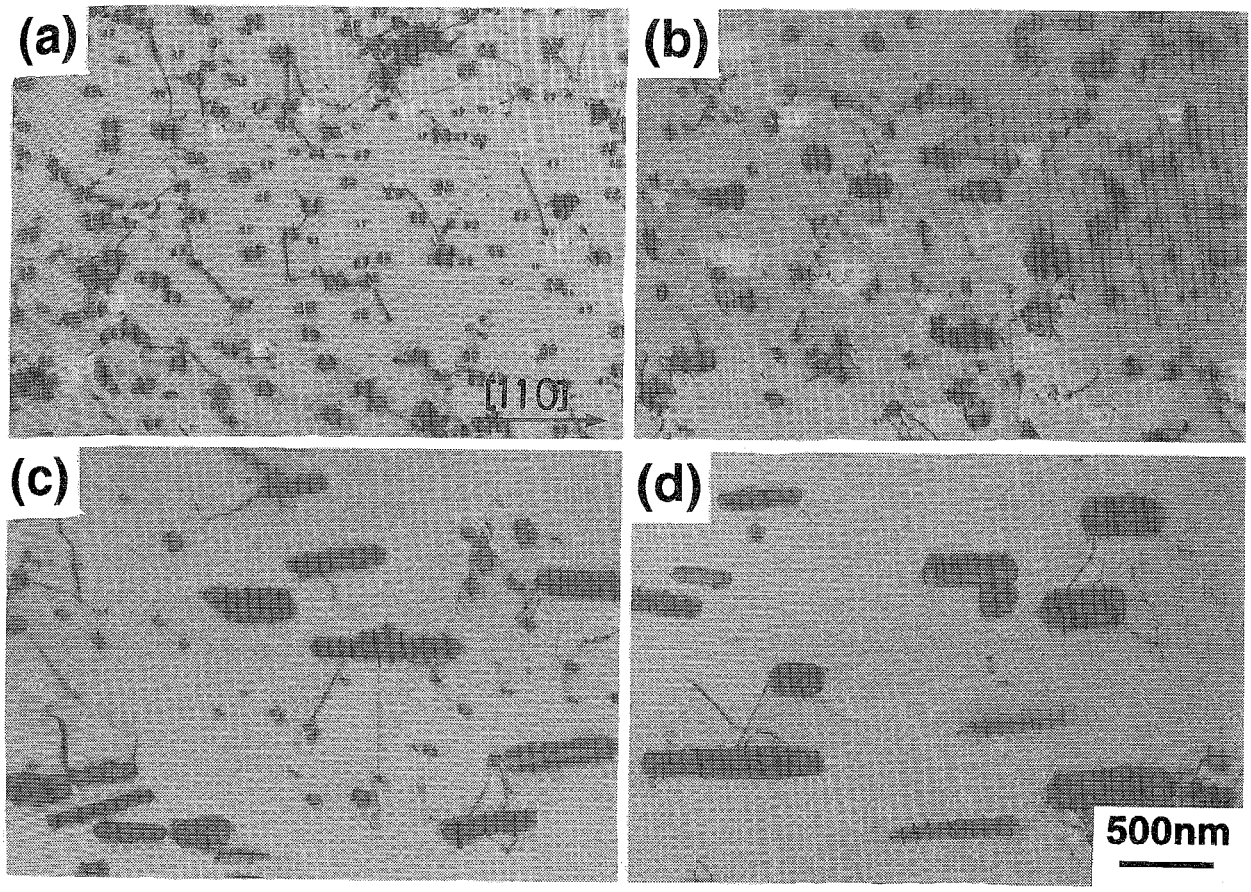

Fig. 3-8. Transmission electron micrographs of α- and γ-iron particles with coffee-bean like contrasts in a Cu-Fe alloy annealed at 973K for (a) 30min, (b) 4h, (c) 14h and (d) 4d. Before the annealing, the specimens were aged at 973K for 1d and deformed by 5% in tension. The foil surface is parallel to $(\bar{1}1\bar{1})$.

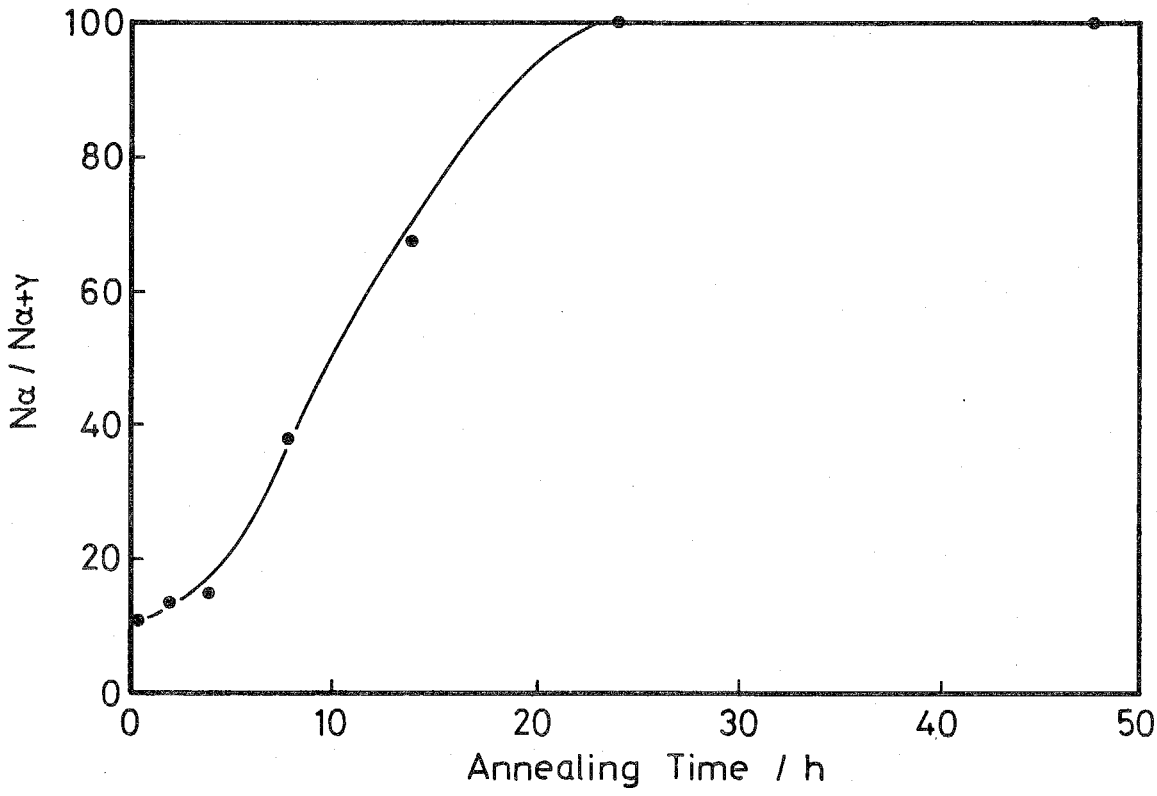

Fig. 3-9. Change in the fraction of the α-iron particles N_α to the whole iron particles $N_{\alpha+\gamma}$ with annealing time.

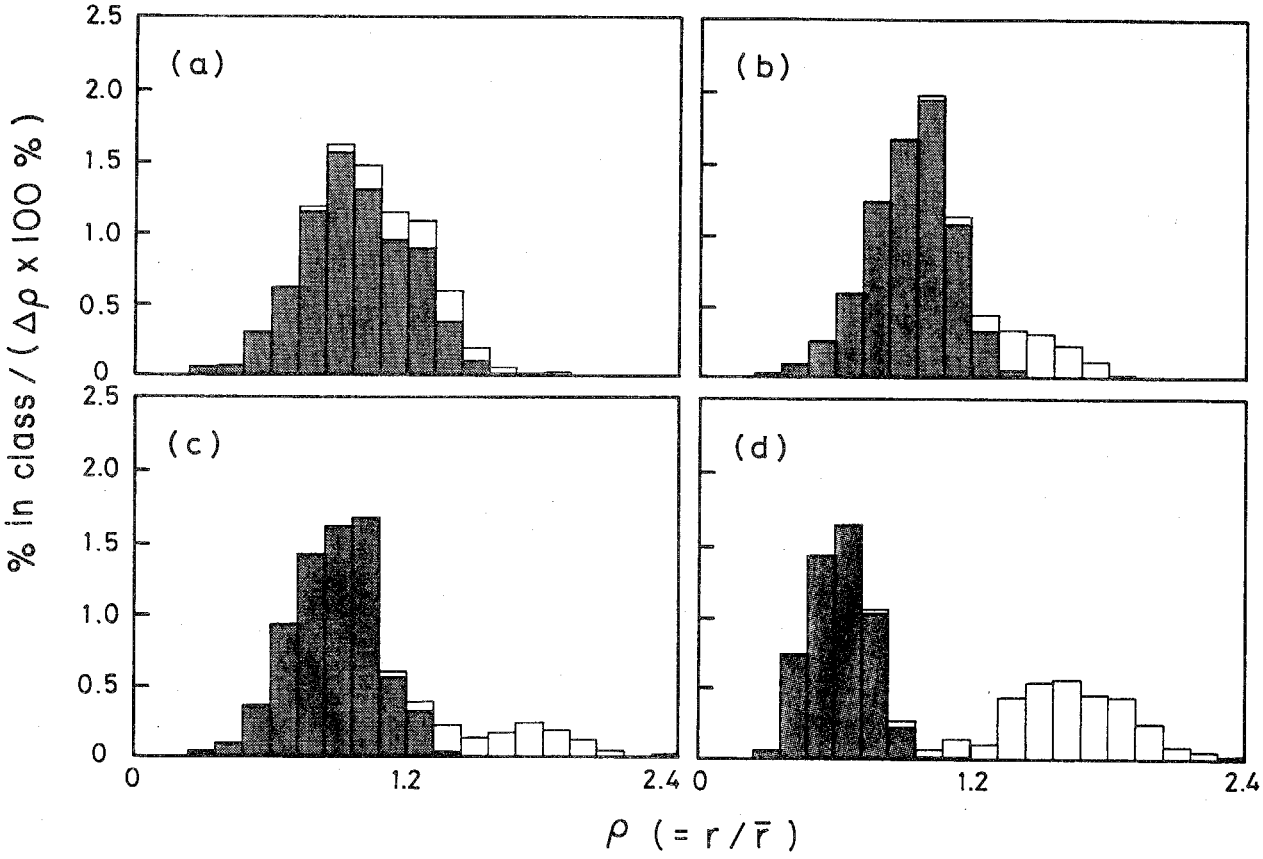

Fig. 3-10. Change in the size distribution of the α- and γ-iron particles in a 5% deformed specimen with annealing time; (a) 30min, (b) 2h, (c) 4h, (d) 8h, (e)14h, (f) 1d, (g) 2d and (h) 4d. The open and shaded areas represent α-and γ-iron particles, respectively.

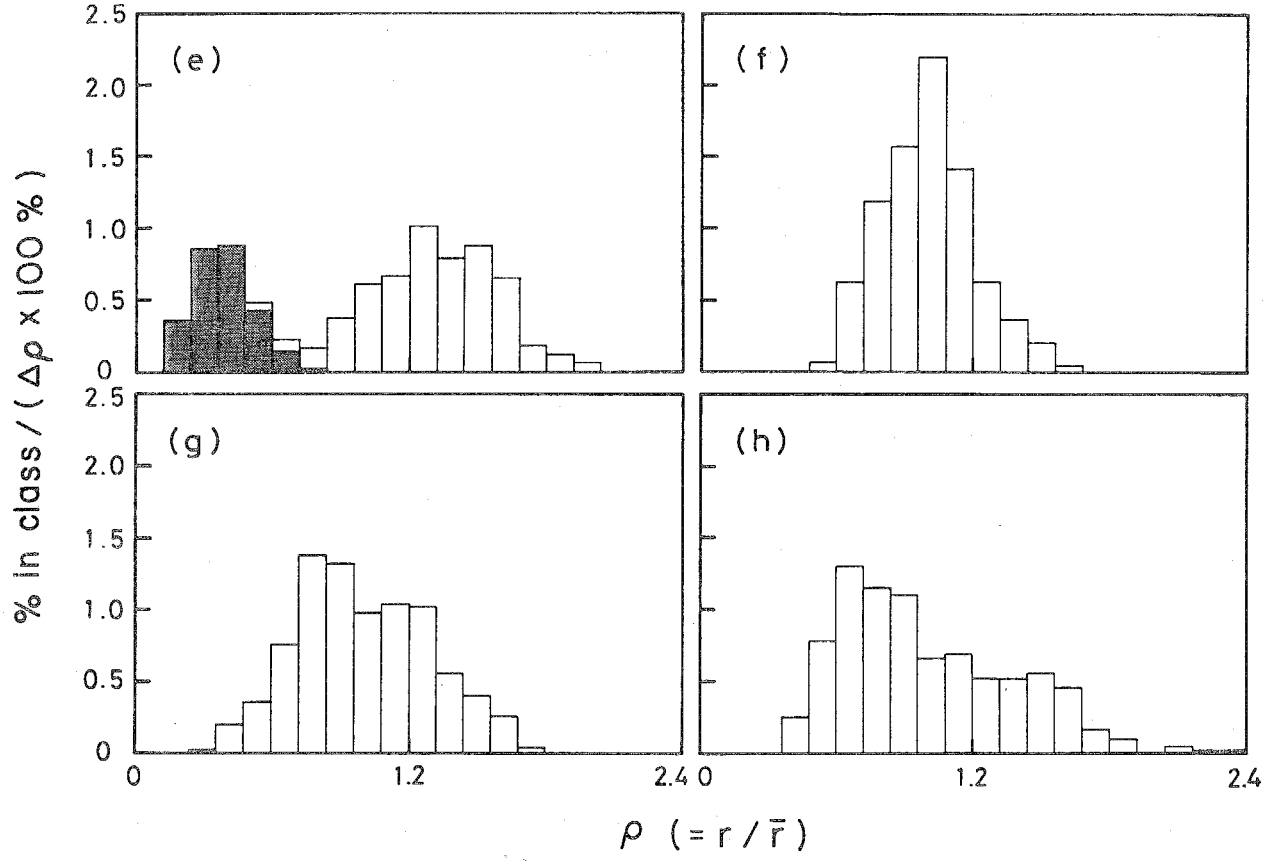

Fig. 3-10. Change in the size distribution of the α- and γ-iron particles in a 5% deformed specimen with annealing time; (a) 30min, (b) 2h, (c) 4h, (d) 8h, (e)14h, (f) 1d, (g) 2d and (h) 4d. The open and shaded areas represent α-and γ-iron particles, respectively.

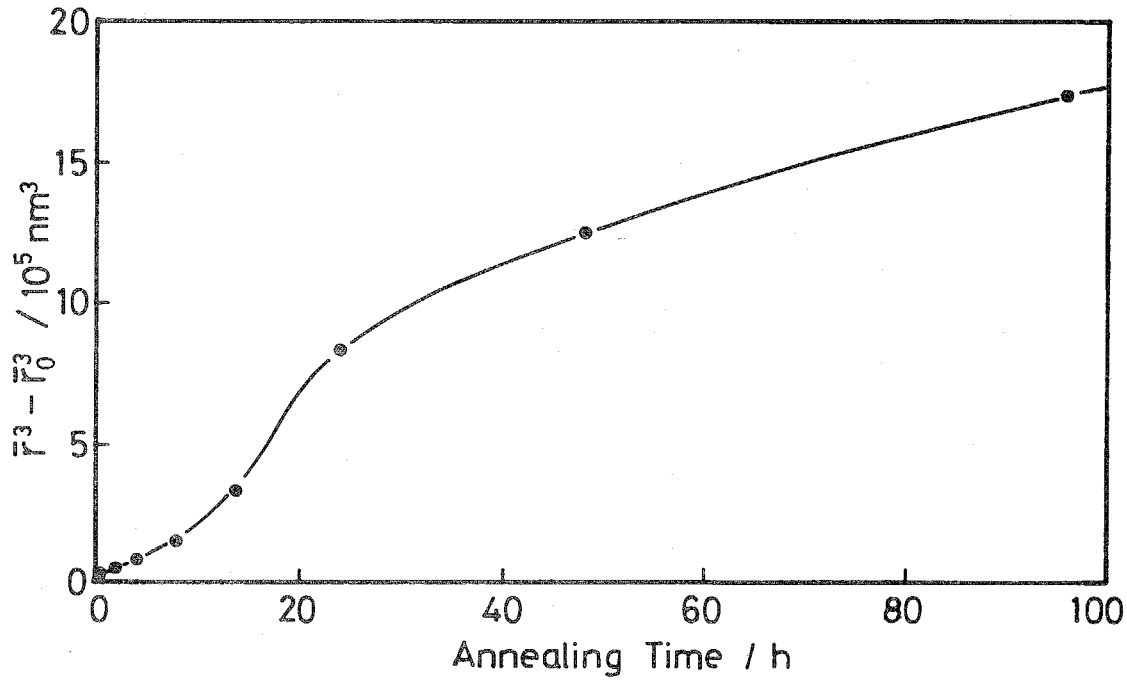

Fig. 3-11. Growth curve for all the iron particles including both α- and γ-iron in a 5% deformed specimen.

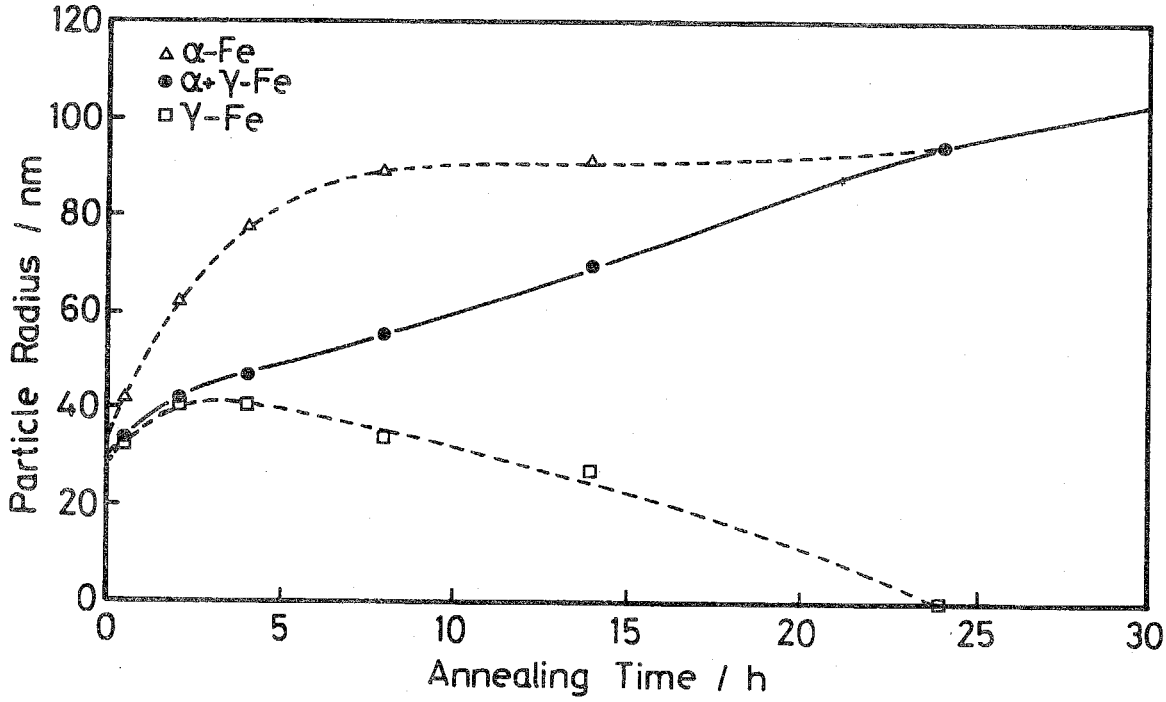

Fig. 3-12. Change in the average sizes of the α- and γ-iron particles (dotted lines) with annealing time. The data for the solid line are the same as those in Fig. 3-11.

obtained from the early-stage annealing data for α-iron particles in Fig. 3-4. This means that the initial growth of the γ-iron particles is significantly enhanced by the presence of the α-iron particles.

As mentioned earlier, the solubility of iron atoms in the copper matrix containing α-iron particles is smaller than that in the matrix containing γ-iron particles [17, 18]. Therefore, in the initial stage of annealing of a specimen with both γ- and α-iron particles, a thermodynamic driving force exists for the dissolved iron atoms in the copper matrix to migrate towards α-iron particles. During the course of their migration, however, some iron atoms may be captured by nearby γ-iron particles since the majority of particles are initially γ-iron. In other words, in addition to the iron atoms in smaller γ-iron particles, the dissolved iron atoms in the copper matrix can contribute to the growth of larger γ-iron particles. This would result in the observed larger growth rate of γ-iron particles in the mixed mode than in the single mode. When the growth is assumed to occur by bulk diffusion, Eq. (3-16) is applicable. In other words, when Eq. (3-16) is applied for $r \leq 1.5\bar{r}$ [2, 3], the larger the interfacial energy and the radius, the larger becomes the growth rate. The change in the size distribution of the α- and γ-iron particles (Fig. 3-10) and the result shown in Fig. 3-12 can be understood qualitatively using Eq. (3-16).

In the early stage of annealing, the average radius $\bar{r}_\gamma$ of the γ-iron particles increases with annealing. This is because a sufficient number of the γ-iron particles, larger than their average size $\bar{r}_{\alpha+\gamma}$, exist as shown in Fig. 3-10(a) and (b). The average radius $\bar{r}_\alpha$ of the α-iron particles, of course, increases since all of the α-iron particles are larger than $\bar{r}_{\alpha+\gamma}$. In this stage, the overall growth, shown in Fig. 3-11, is governed by the growth of the γ-iron particles which constitute the majority of the existing particles. However, the growth rate of the α-iron particles is larger than that of the γ-iron particles even during this stage; $\Gamma_\alpha > \Gamma_\gamma$ and $\bar{r}_\alpha > \bar{r}_{\alpha+\gamma}$. Thus, as the annealing proceeds, most of the γ-iron particles become smaller than $\bar{r}_{\alpha+\gamma}$ while all the α-iron particles grow. Eventually, clear splitting of the particle size distribution is observed as shown in Fig. 3-10(c), (d) and (e). That is, the number fraction of the α-iron particles becomes larger than that of the γ-iron particles after 10h annealing. The standard deviation of the particle size distribution reaches the maximum value at this stage as shown in Fig. 3-13. After this stage, the overall growth as well as the particle size distribution is governed by the growth of the α-iron particles. In and after this stage, those α-iron particles which are smaller than $\bar{r}_{\alpha+\gamma}$ exist and decrease their size. Thus, the average growth rate of the α-iron particles becomes smaller.

The single mode of the α-iron particle growth occurs when the γ-iron particles completely dissolve. After this stage, the growth and coarsening proceed in a manner similar to the case shown in the previous section. This is confirmed by the agreement of the later-stage growth rate constants;

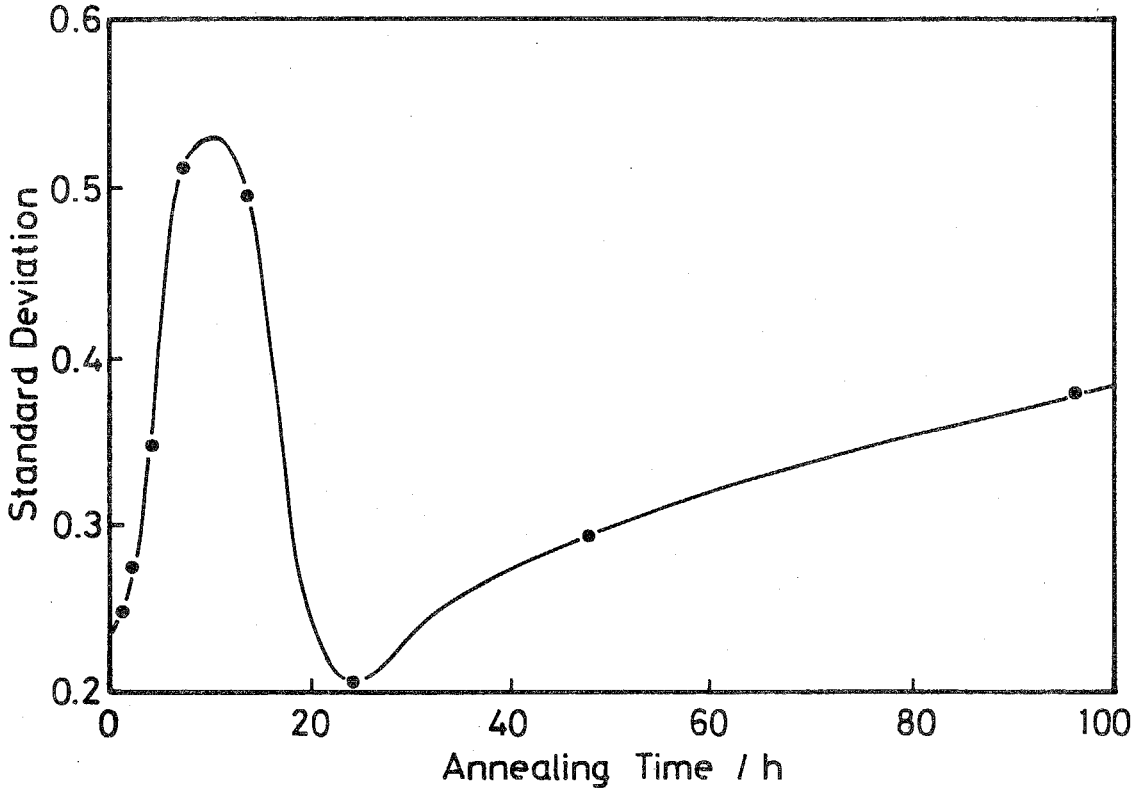

Fig. 3-13. Change in the standard deviation of the size distribution shown in Fig. 3-10 with annealing time.

$K_\alpha^1 = 3.43 \times 10^{-21}$ m^3/s in the mixed mode after annealing for 1d (Fig. 3-11) and $K_\alpha = 3.23 \times 10^{-21}$ m^3/s in the single mode after annealing for 2h (Fig. 3-4). The mean aspect ratio of the α-iron particles and its scatter are shown in Figs. 3-14 and 3-15, respectively. They are similar to Figs. 3-3 and 3-7 obtained in the single-mode growth. The difference in the absolute values of the mean aspect ratio in the late stages of annealing, as shown in Fig. 3-3 and Fig. 3-14, reflects the difference in the initial fraction and the size of the α-iron particles. That is, all the α-iron particles satisfy $r_\alpha > \bar{r}_{\alpha+\gamma}$ and they preferentially grow and elongate in the mixed mode of the growth.

The fact that all the α-iron particles grow in the beginning of the mixed-mode growth is because only larger γ-iron particles undergo the martensitic transformation by straining. If some particles, smaller than the average size, could be transformed by some means, they would become smaller and dissolve even in the early stage of annealing. The critical size, which determines the growth or shrinkage, is the average radius, see Eq. (3-16). In addition, the growth or shrinkage rate for the mixed-mode growth is controlled not only by interfacial free energy but also by the difference in chemical free energies between γ- and α-iron. Thus, a straightforward application of the LSW theory of Ostwald ripening is not possible for the overall discussion of the mixed-mode growth.

3.5. Summary and conclusions

As the theoretical phase of the present study, fundamental rate equations for Ostwald ripening were derived without using the Gibbs-Thomson-Freundlich equation as a starting point. Rather, the change (decrease) in the interfacial free energy is evaluated directly. This method enables us to image the physics involved very easily.

As the experimental phase, the growth of the α-iron particles in the copper matrix has been examined. The growth rate of the α-iron particles was not strictly constant with annealing because of the change in the shape of the α-iron particles and in the interfacial energy per unit area. Nevertheless, an approximate and average value of the α-Fe/Cu interfacial energy was obtained from the growth curve; $3.3 J/m^2$. The growth process was also studied when α- and γ-iron particles coexisted. Although γ-iron particles grew in the early stage of annealing, they eventualy shrunk and disappeared. The α-iron particles, on the other hand, grew during the entire stages of annealing. Naturally, the mixed-mode growth did not obey the usual Ostwald ripening theory. The particle size distribution also differed from that predicted by the theory. To understand the mixed-mode growth behavior, not only the average particle sizes and interfacial free energies but also the

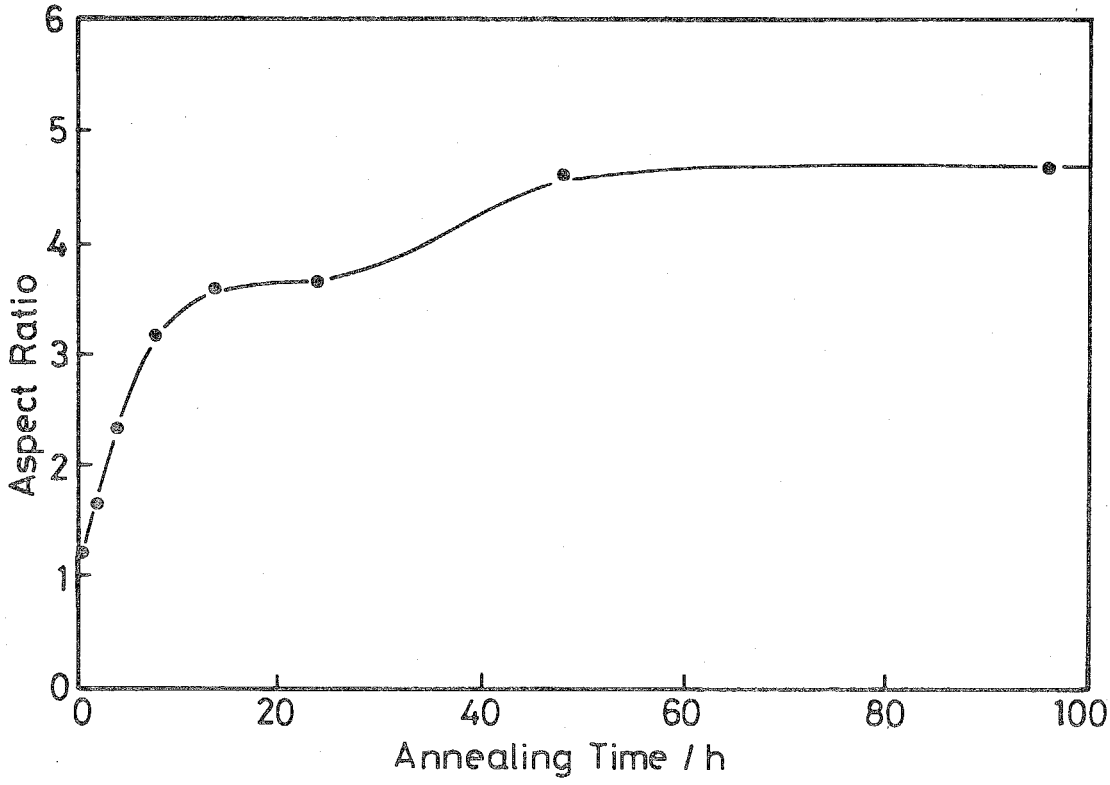

Fig. 3-14. Change in the mean aspect ratio of the α-iron particles in a 5% deformed specimens with annealing time.

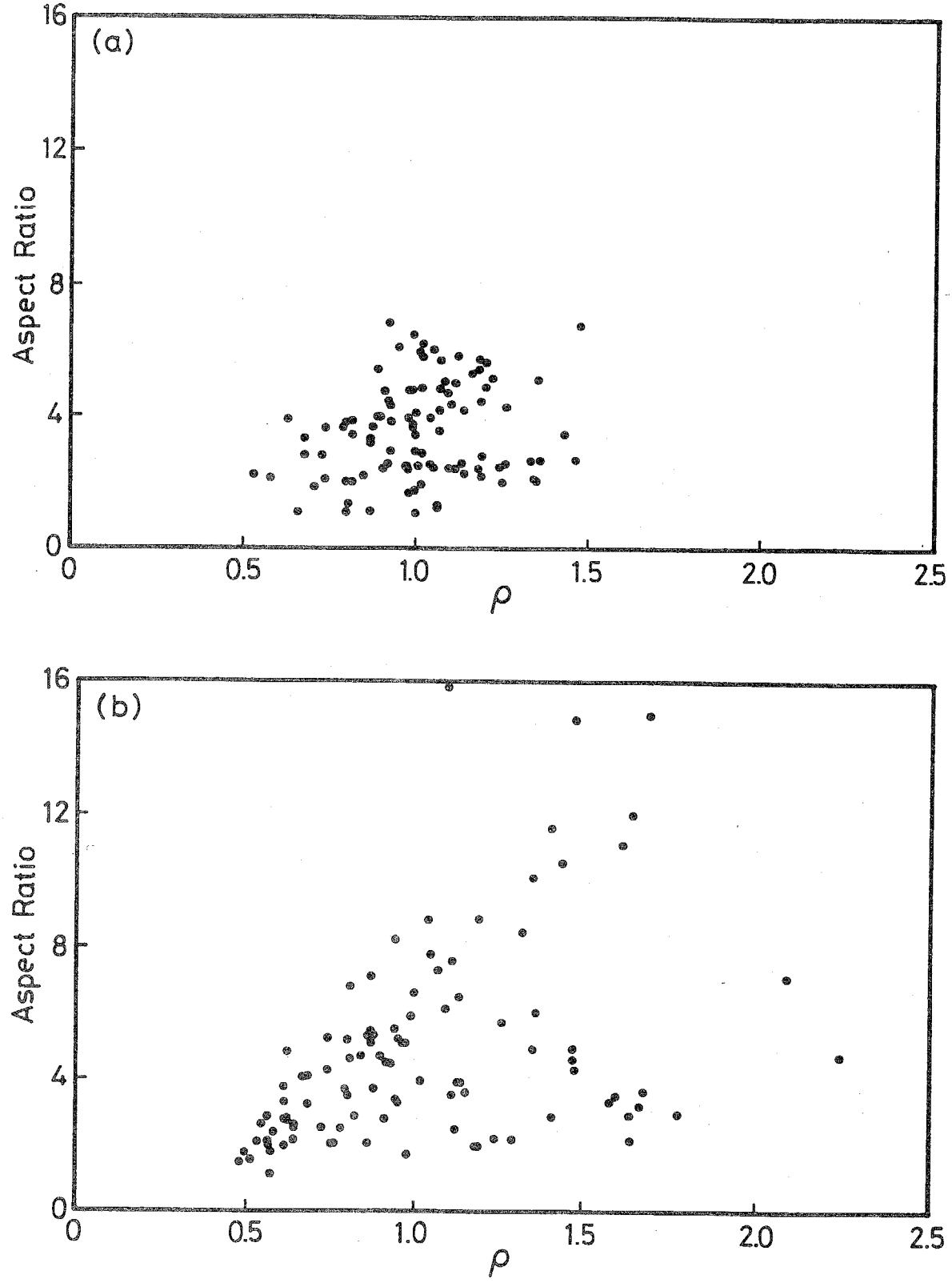

Fig. 3-15. Relationship between the aspect ratio and the normalized radius of the α-iron particles in specimens annealed at 973K for (a) 1d and (b) 4d.

difference in chemical free energies between γ- and α-iron has to be taken into account.

References

[1] K. Matsuura, M. Kitamura and K. Watanabe: *J. Japan Inst. Metals*, **41** (1977), 1285.

[2] I. M. Lifshitz and V. V. Slyozov: *J. Phys. Chem. Solids*, **19** (1961), 35.

[3] C. Wagner: *Z. Elektrochem.*, **65** (1961), 581.

[4] G. R. Speich and R. A. Oriani: *Trans. Met. Soc. AIME*, **233** (1965), 623.

[5] A. J. Ardell: *Acta Metall.*, **20** (1972), 61.

[6] A. D. Brailsford and P. Winblatt: *Acta Metall.*, **27** (1979), 489.

[7] C. K. L. Davies, P. Nash and R. N. Stevens: *Acta Metall.*, **28** (1980), 179.

[8] J. A. Marqusee and J. Ross: *J. Chem. Phys.*, **80** (1984), 536.

[9] P. W. Voorhees and M. E. Glicksman: *Acta Metall.*, **32** (1984), 2001.

[10] Y. Enomoto, M. Tokuyama and K. Kawasaki: *Acta Metall.*, **34** (1986), 2119.

[11] G. W. Greenwood: *Acta Metall.*, **4** (1956), 243.

[12] M. V. Speight: *Acta Metall.*, **16** (1968), 133.

[13] P. W. Voorhees and R. J. Schaefer: *Acta Metall.*, **35** (1987), 327.

[14] S. Onaka and M. Kato: *ISIJ Int.*, **31** (1991), 331.

[15] M. Kato, R. Monzen and T. Mori: *Acta Metall.*, **26** (1978), 605.

[16] Japan Inst. Metals: *Kinzoku Data Book*, Maruzen, Tokyo, (1974), p.25.

[17] A. G. H. Andersen and A. W. Kingsbury: *AIME Trans.*, **52** (1943), 38.

[18] G. Tammann and W. Oelsen: *Z. anorg. u. allg. Chem.*, **186** (1930), 257.

Chapter 4.

Magnetic Anisotropy Caused by the Formation of Stress-Induced Martensite in Small Iron Particles in a Copper Matrix

4.1. Introduction

As described in Chapter 2, applied stress helps (prohibits) the formation of specific martensite variants out of crystallographically equivalent ones. From detailed studies of the crystallography of stress-induced γ(f.c.c.)$\rightarrow\alpha$(b.c.c.) martensitic transformation in ferrous alloy single crystals, it has been found that preferentially-formed martensite variants are sensitive to the direction and sense (tension or compression) of the uniaxial applied stress [1-5]. To examine the crystallography of the preferentially-formed variants, X-ray diffraction and electron microscopy techniques have been adopted most commonly.

The purpose of the present study is to apply a new technique, magnetic anisotropy measurement, to investigate the preferentially-formed martensite variants. There are some advantages in this technique: the measurement can be performed easily and information from bulk specimens can be obtained very quickly. For this technique to be applicable it is essential that an alloy system should have a non-magnetic (paramagnetic) parent phase and magnetically anisotropic ferromagnetic martensites.

The Cu-Fe system is best suited for the above purpose. As mentioned in Chapter 2, the nearly spherical α-iron martensite particles are ferromagnetic and have cubic magnetic anisotropy. They exhibit internally-twinned layered structure and both of the twin-related variants are known to obey the Kurdjumov-Sachs (KS) orientation relationship to the copper matrix [4, 6, 7]. Since the γ-iron and the copper matrix are paramagnetic at room temperature, detectable spontaneous magnetization, if any, arises essentially from the transformed α-iron particles.

It has been found in the previous study [6, 8] as well as in Chapter 3 that annealing of the Cu-Fe alloy with transformed α-iron particles causes the spherical to ellipsoidal shape change of the particles [6, 8]. Associated with this change, the number of twin layers in the α-Fe particles gradually decreases to eventually become KS-oriented single-crystalline particles consisting of one of the originally-twinned KS variants. It should be pointed out here that the present magnetic anisotropy measurment technique can also detect such a morphological change in the α-iron particles. This is because the shape of ferromagnetic materials is responsible for another type of magnetic anisotropy known as the shape magnetic anisotropy [9]. Therefore, using the magnetic

anisotropy measurement technique, we can simultaneously obtain the crystallographic and morphological information on the existing martensite variants in bulk specimens.

4.2. Experimental

4.2.1. Specimen preparation

Single crystal of a Cu-1.53mass%Fe alloy were grown by the Bridgman method. Specimens for tensile (9×9×90mm) and compressive (9×9×20mm) tests were cut from the single crystals so as to make the $[419]_f$ direction parallel to the stress axis. This asymmetric stress axis was chosen in the light of the study described in Chapter 2 that only a few stress-induced martensite variants were preferentially formed out of 24 crystallographically equivalent KS variants.

After solution treatment at 1273K for 4h, these specimens were aged at 973K for 1d. The aging treatment caused the precipitation of spherical γ-iron particles in the copper matrix. The average diameter and volume fraction of the particles (estimated from the Cu-Fe phase diagram) are 75nm and 1.40vol%, respectively. To induce the γ→α martensitic transformation in the iron particles, the specimens were deformed in tension or in compression by more than 10% at 77K. It is known from previous studies [6, 10] that this deformation condition induces the martensitic transformation in practically all (over 90%) the particles. Therefore, we can reasonably assume without introducing significant errors that the volume fraction of transformed α-iron particles is 1.40%. Although this may be a slight overestimation, it will not change the discussion and conclusions of this study.

After the deformation, disk specimens (about 6 mm diameter and 1.5 mm thickness) for the magnetic anisotropy measurement were cut parallel to the $(\bar{1}1\bar{1})_f$ plane. To introduce the morphological change in the transformed α-iron particles, the disk specimens were annealed at 973K for various lengths of time and the magnetic anisotropy was measured.

4.2.2. Magnetic anisotropy measurement

The magnetic anisotropy of Cu-Fe specimens containing α-iron particles was examined by measuring magnetic torque using a Naruse TM-II torque meter [11]. Figure 4-1 is a schematic drawing of the torque meter and the set-up of a single crystal specimen. By applying a magnetic field of 1.25MA/m, the α-iron particles in the specimen are magnetized to saturation along the direction of the magnetic field. The applied magnetic field is rotated by 360° around the $(\bar{1}1\bar{1})_f$ plane of the specimen with the $[\bar{1}01]_f$ direction as the starting direction. Figure 4-2 shows the

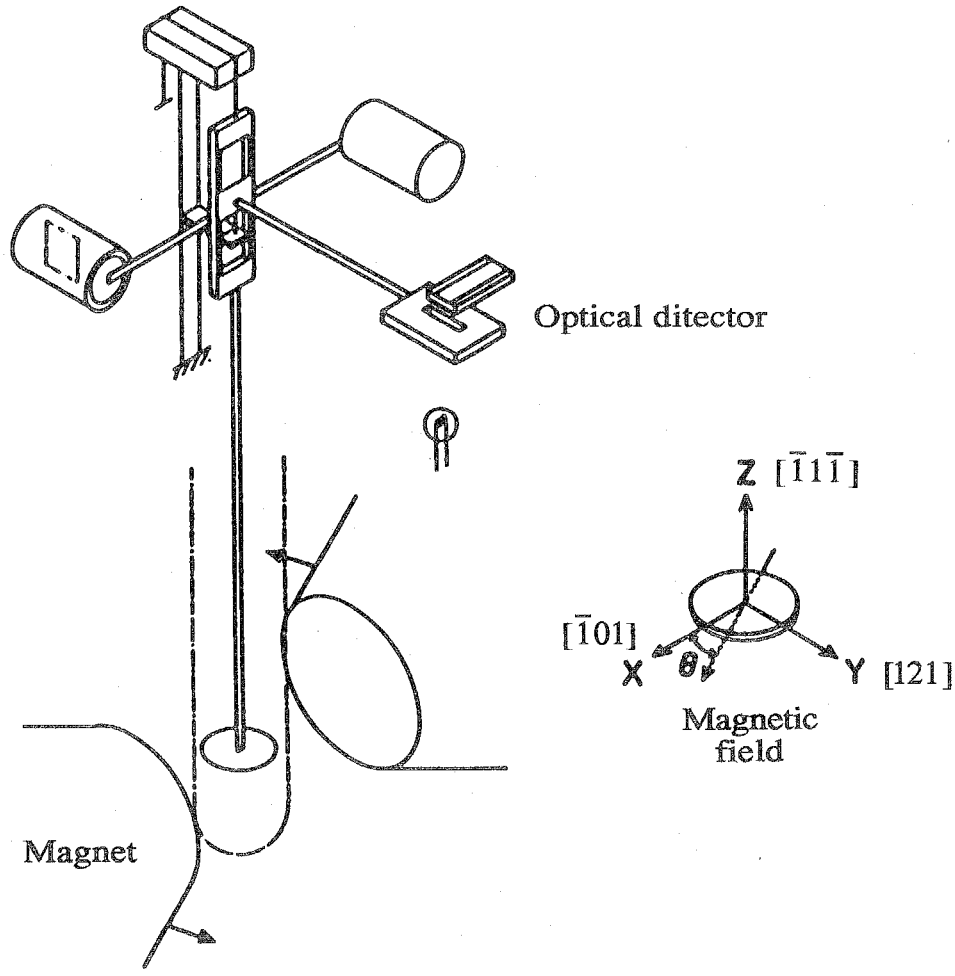

Fig. 4-1. Schematic drawing of the torque meter and the set-up of a single crystal specimen.

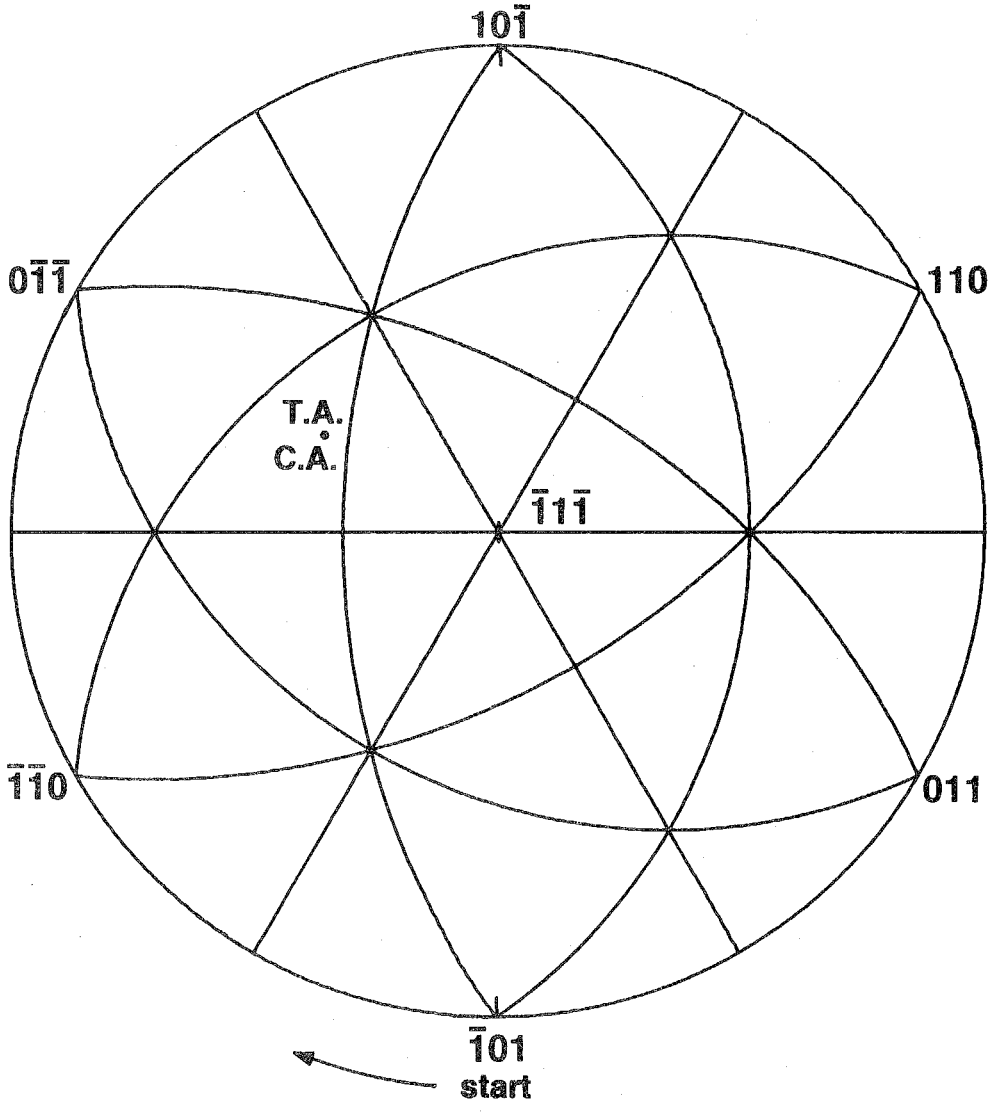

Fig. 4-2. $(\bar{1}1\bar{1})_f$ stereographic projection showing the $[419]_f$ axis for tension (T.A.) and compression (C.A.) and the orientation of disk specimens for the magnetic anisotropy measurement.

$(\bar{1}1\bar{1})_f$ stereographic projection indicating the orientation of the disk specimens for the magnetic anisotropy measurement. The magnetic anisotropy in the present specimens arises from two origins; (i) crystal anisotropy and (ii) shape anisotropy. The orientation-dependent part of the crystal magnetic anisotropy energy E_C per unit volume of α-iron with three $\langle 100 \rangle_b$ directions of easy magnetization can be written as [9]

$$E_C = K_1\left(\alpha_1^2\alpha_2^2 + \alpha_2^2\alpha_3^2 + \alpha_3^2\alpha_1^2\right) + K_2\alpha_1^2\alpha_2^2\alpha_3^2 \tag{4-1}$$

where $[\alpha_1, \alpha_2, \alpha_3]_b$ is the normalized magnetization direction and K_1 (= 4.72×10^4 J/m^3 for iron [12]) and K_2 (= -7.5×10^2 J/m^3) are the magnetic anisotropy constants of iron.

The shape magnetic anisotropy, on the other hand, depends on the shape of ferromagnetic domains. In this study, the elongated shape of α-iron particles caused by annealing is approximated as spheroids. If the z-axis in the x-y-z coordinate system is taken parallel to the longer axis, the orientation-dependent part of the magnetostatic energy E_S per unit volume can be written as [13]

$$E_S = \frac{1}{4\mu_0} I_S^2\left(3N_Z - 1\right)\cos^2\phi \tag{4-2}$$

where μ_0 is the magnetic permeability of vacuum, I_S the saturation magnetization and ϕ the angle between the magnetization direction and the z-axis. By defining the aspect ratio k (≥ 1) as the length of the longer axis divided by the shorter axis (cross-sectional diameter of the x-y circle), the demagnetizing factor N_z can be expressed as [13]

$$N_Z = \frac{1}{k^2-1}\left[\frac{k}{\left(k^2-1\right)^{1/2}}\ln\left\{k + \left(k^2-1\right)^{1/2}\right\} - 1\right] \tag{4-3}$$

When the applied magnetic field is rotated, two kinds of resolved torque components on the $(\bar{1}1\bar{1})_f$ plane, L_C and L_S are generated:

$$L_C = -(\partial E_C/\partial\theta) \tag{4-4}$$

and

$$L_S = -(\partial E_S/\partial\theta) \tag{4-5}$$

where θ is the rotation angle between the starting direction $[\bar{1}01]_f$ and the direction of the applied magnetic field. From Eqs. (4-1) to (4-5), theoretical torque curves as a sum of L_C and L_S can be calculated for given KS variants and the aspect ratio of the α-iron particles. Experimentally obtained torque curves can then be compared with the theoretical ones.

4.3. Results

Figure 4-3 shows the torque curves of a specimen deformed by 14% in tension at 77K. The annealing time at 973K after the deformation is indicated in each figure. The ordinate in the figure is normalized as a torque value per unit volume of α-iron by assuming that the volume fraction of α-iron is 1.40%. The abscissa is the rotation angle θ on the $(\bar{1}1\bar{1})_f$ plane with $\theta = 0°$ corresponding to $[\bar{1}01]_f$. Energetically stable zero-torque points are those where the torque values change from positive to negative as θ increases. The fact that all the curves have a 180° period is a natural result of the magnetic anisotropy.

It can be seen from Fig. 4-3(a) that the curve for the as-deformed (0 min annealed) specimen is rather complicated. However, as annealing time increases, the curves become simpler and sinusoidal-like. Moreover, the amplitude of the curves increases as annealing time increases.

A set of torque curves for a specimen deformed by 12% in compression at 77K are shown in Fig. 4-4. Comparison with Fig. 4-3 reveals that although the development of the shape and amplitude of the curves by annealing is similar, the phases (the phase angles) of the curves are different. In other words, the curves in Fig. 4-3 have maxima near $\theta = 0°$ and 180° whereas the curves in Fig. 4-4 have maxima near $\theta = 120°$ and 300°.

In order to examine the morphological changes of the α-iron particles by annealing, transmission electron microscopy (TEM) observation was performed. Figure 4-5 shows the bright-field micrographs of specimens from which data in Fig.4-4 were taken. It can be seen that initially spherical α-iron particles become elongated and larger as annealing time increases. It should also be noticed that all the particles in sight have elongated along the same $[10\bar{1}]_f$ direction. This is due to the fact that the $[419]_f$ external stress induces the preferential formation of certain KS variants out of 24 crystallographically equivalent ones, as mentioned previously. In the next section, the observed torque curves are analyzed in the light of the TEM observation and theoretical expectation.

4.4. Discussion

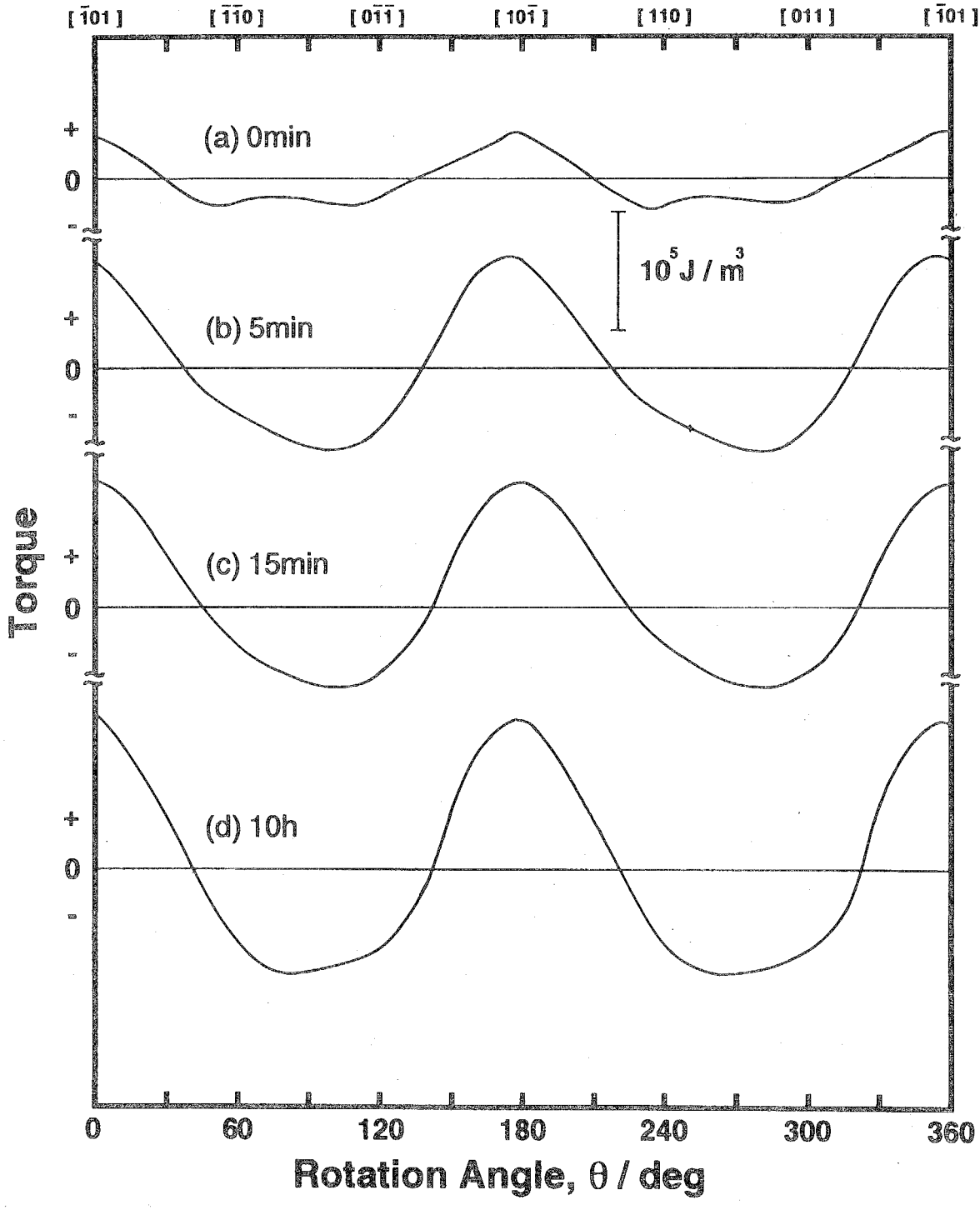

Fig. 4-3. Magnetic torque curves obtained from specimens deformed in tension by 14% at 77K and successively annealed at 973K for (a) 0min, (b) 5min, (c) 15min and (d) 10h. θ-rotation axis: $[\bar{1}1\bar{1}]_f$.

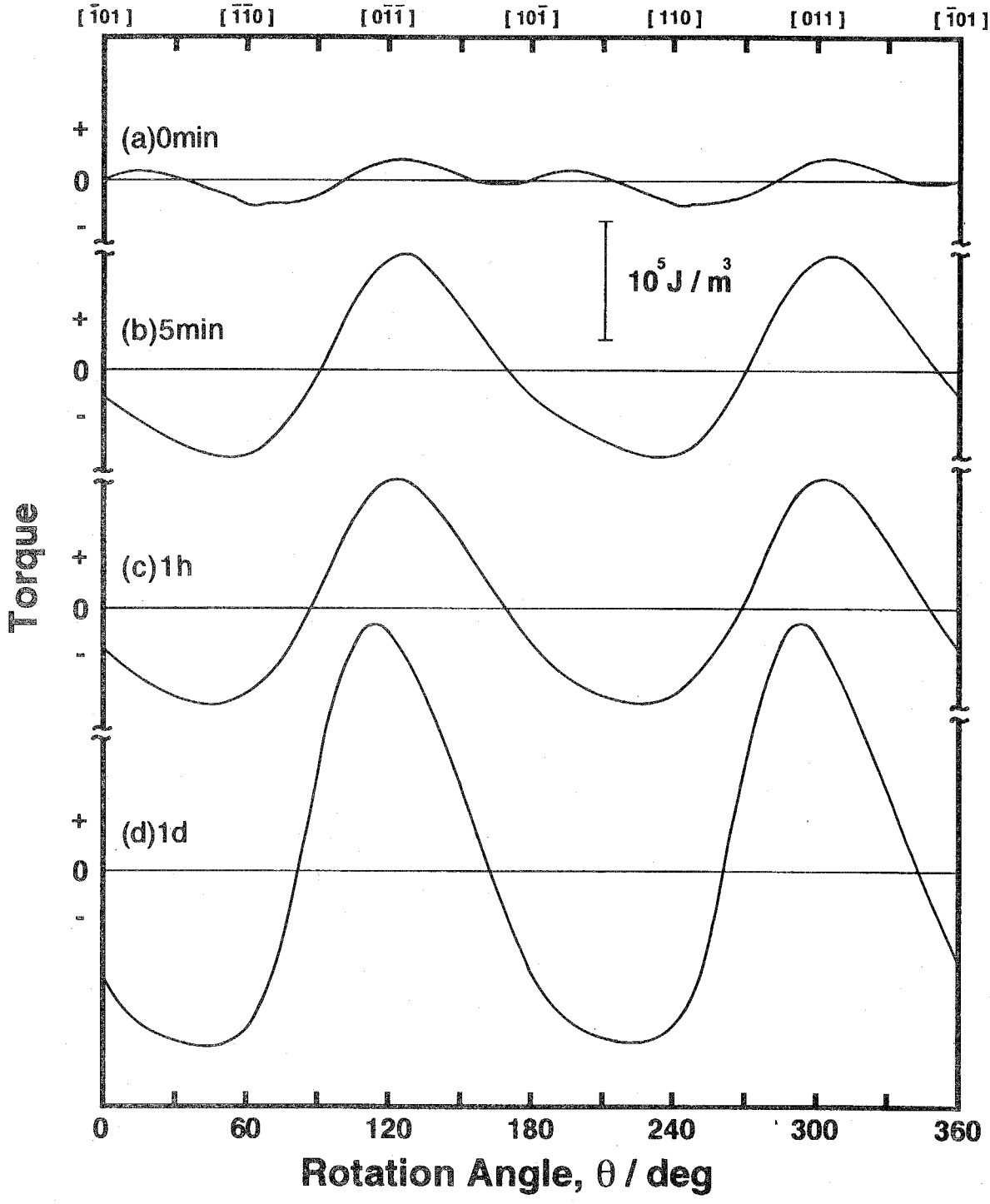

Fig. 4-4. Magnetic torque curves obtained from specimens deformed in compression by 12% at 77K and successively annealed at 973K for (a) 0min, (b) 5min, (c) 1h and (d) 1d. θ-rotation axis: $[\bar{1}1\bar{1}]_f$.

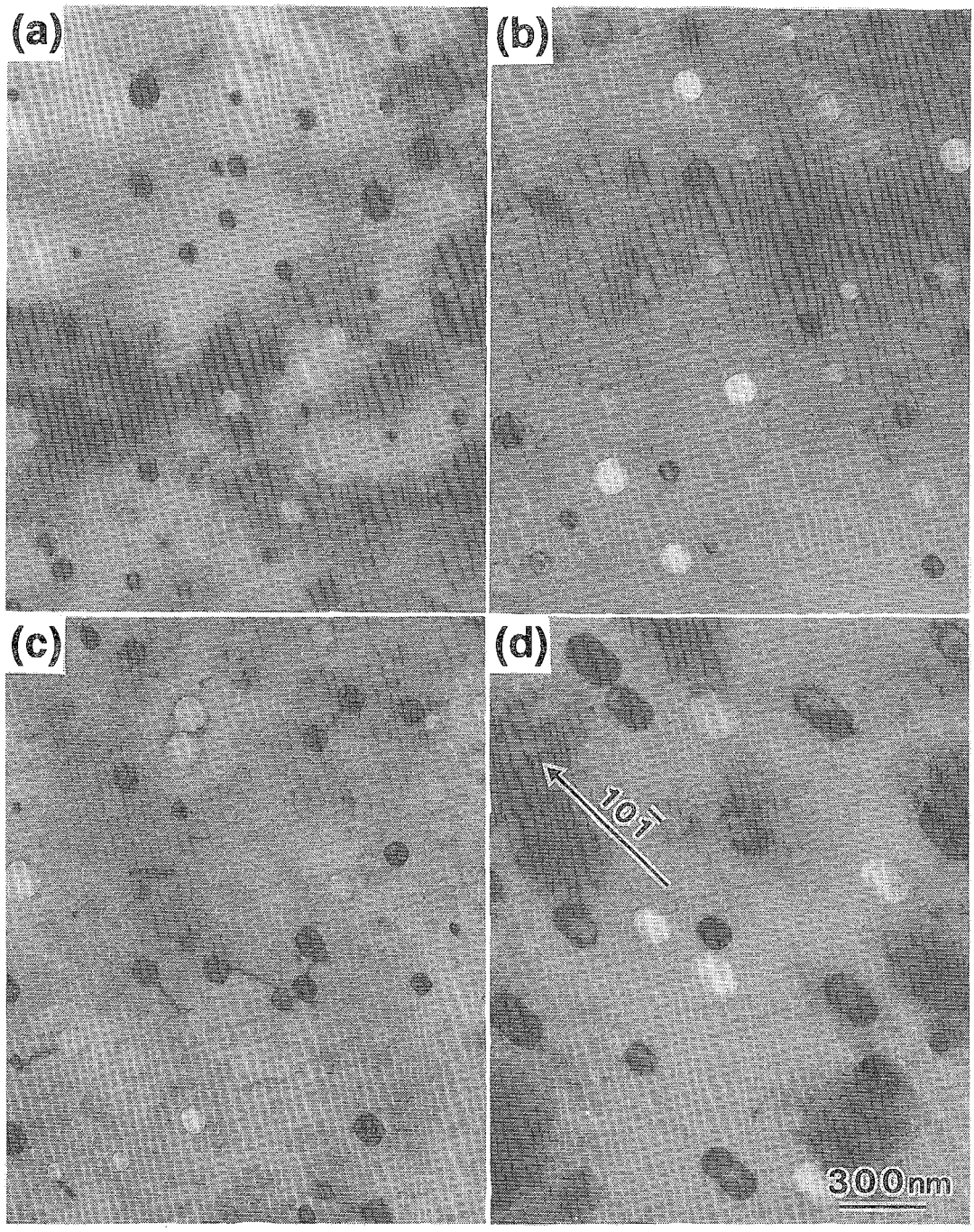

Fig. 4-5. TEM micrographs of specimens from which the torque curves in Fig. 4-4 were obtained.

For the following analysis, the notation of the 24 KS variants already listed in Table 2-1 in Chapter 2 will be used. It is known that the as-transformed α-iron particles are internally twinned and the two mutually-twinned KS variants (for example, variants 1-1 and 1-4) exist approximately in equal amounts [4]. It is also known that although annealing causes the disappearance of the twinned structure, the resultant single-crystalline particles belong to either one of the two twin-related variants with equal probabilities [6, 14]. Therefore, we can reasonably assume that the twin-related pairs of the KS variants exist in equal amounts in all the specimens. According to Fig. 4-5 as well as the previous TEM study [14], the α-iron particles by annealing are found to elongate approximately along $\langle 110 \rangle_f$ -type directions which describe the parallel relationship of respective KS variants. For example, as known from Table 2-1, particles belonging to the (1-1, 1-4) pair elongate along $[10\bar{1}]_f$ and particles belonging to the (1-3, 1-6) pair elongate along $[110]_f$. With the above experimental facts in mind, let us analyze the observed torque curves.

Figure 4-6(a) shows the theoretical torque curve L_C (Eq. (4-4)) caused by the appearance of the (1-1, 1-4) α-iron particles and Fig. 4-6(b) shows the theoretical torque curve L_S (Eq. (4-5)) of the same particles with the aspect ratio $k = 1.06$ and the elongation direction of $[10\bar{1}]_f$. The sum of these two curves (Fig. 4-6(c)) expresses the resultant overall theoretical curve. Although the L_S curve vanishes for spherical particles ($k = 1$), it can be seen from Fig. 4-5 that L_S becomes more dominant than L_C even for $k = 1.06$ which is only slightly larger than unity.

For the analysis of experimental torque curves, let us decompose the theoretical curves in Fig. 4-6 into Fourier components. If $f(\theta)$ is a function of the angle θ ($0 \le \theta \le 2\pi$), the Fourier decomposition of $f(\theta)$ becomes

$$f(\theta) = (A_0 / 2) + \sum_{n=1}^{\infty} \{A_n \cos(n\theta) + B_n \sin(n\theta)\} \tag{4-6}$$

where A_0, A_n and B_n are the Fourier coeffficients and they can be calculated as

$$A_n = \frac{1}{\pi} \int_0^{2\pi} f(\theta) \cos(n\theta)\, d\theta \tag{4-7}$$

$$B_n = \frac{1}{\pi} \int_0^{2\pi} f(\theta) \sin(n\theta)\, d\theta \tag{4-8}$$

The calculated Fourier coefficients of the curves L_C and L_S are listed in Table 4-1. Equation (4-1) predicts that the L_C curve consists of sinusoidal waves with periods 180° ($n = 2$), 90° ($n = 4$) and 60° ($n = 6$). However, since K_2 is much smaller than K_1, the Fourier coefficients A_6 and B_6 can be

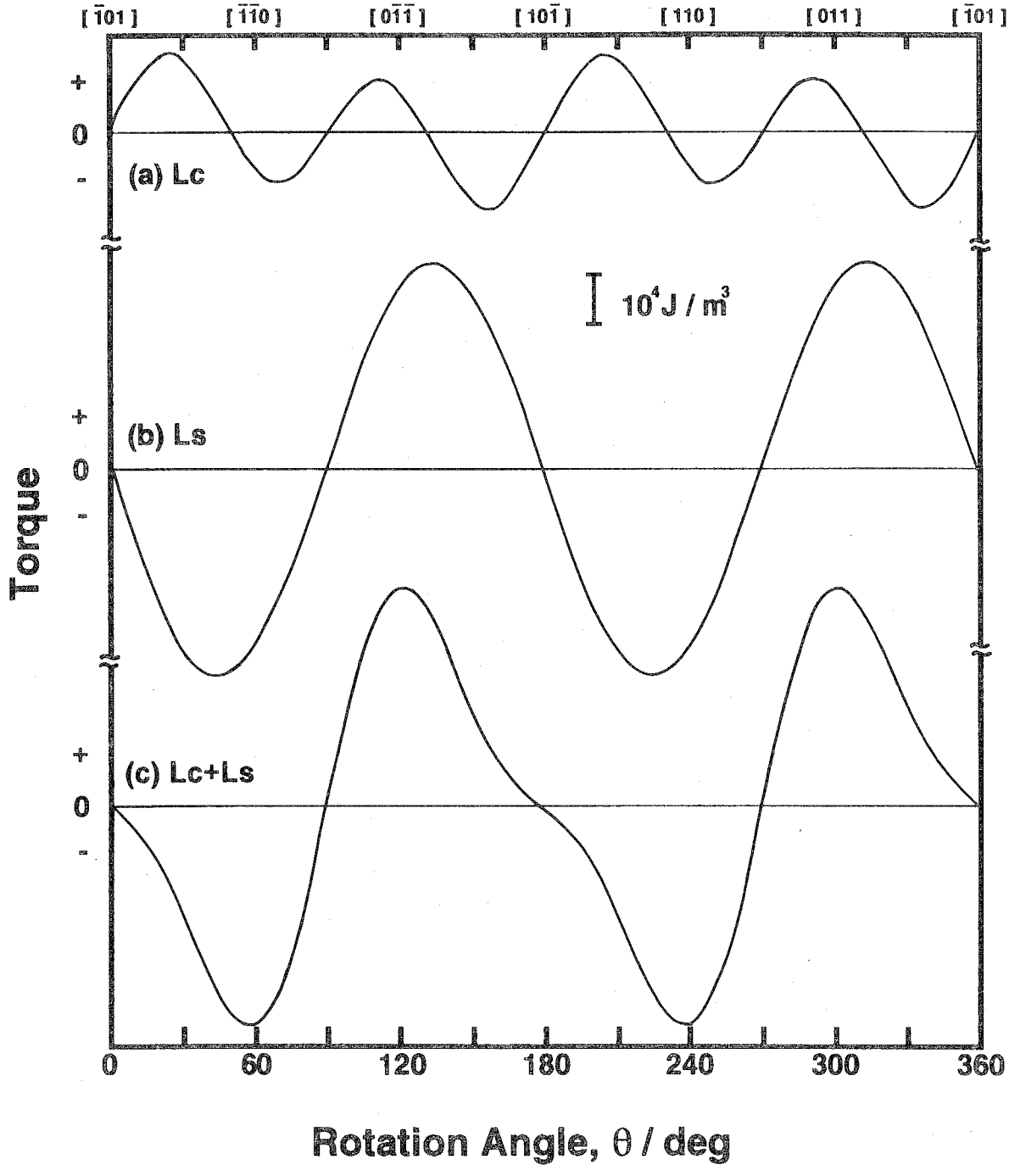

Fig. 4-6. Theoretically calculated magnetic torque curves for a unit volume of elongated (k=1.06) α-iron particles made of the (1-1,1-4) twin pair. (a) crystal magnetic anisotropy, L_C, (b) shape magnetic anisotropy, L_S and (c) total magnetic anisotropy, L_C+L_S.

Table 4-1. The calculated Fourier coefficients for the torque curves in Fig. 4-6(a) and (b).

Curve	Fourier coefficients			
	A_2	B_2	A_4	B_4
(a) L_c	0	3.93×10^3	0	13.73×10^3
(b) L_s	0	-42.82×10^3	0	0

neglected. The L_S curve, on the other hand, is much simpler and it consists of a single sinusoidal wave with a period 180° ($n = 2$).

Such an analysis has been conducted for all the 12 KS twin pairs. No matter what rotation axis of the applied magnetic field is taken, it can be found from the crystal symmetry that the theoretical torque curves of the twin pairs (1-1, 1-4) and (2-1, 2-4) are undistinguishable. The same situation was also found for other twin pairs. After all, the 12 KS twin pairs are further categorized into six (6) groups, #11 to #31, as shown in Table 4-2.

To find the existing variants and the morphology of α-iron particles in a given specimen, theoretical torque curves which can accurately reproduce the experimental curves must be found. The actual procedure to find the best-fit theoretical curves is as follows. First, theoretical L_C and L_S curves for all the six groups are decomposed into Fourier components. This enables us to express a theoretical torque curve by five parameters, *i.e.*, A_2, B_2, A_4, B_4 and k. Secondly, the experimental curve is also decomposed into Fourier components by a computer calculation. If A_n and B_n coefficients with $n \geq 6$ are found to exist, they are neglected since these components do not appear in the theoretical curves. Lastly, by comparing the Fourier components and the shape of theoretical and experimental curves, good-fit theoretical curves with certain combinations of the volume fraction and the aspect ratio of each group are selected from many candidates.

To evaluate the shape resemblance between the theoretical and experimental curves, each curve is normalized by dividing it by $(A_2^2+B_2^2)^{1/2}$. When the normalized theoretical and experimental curves are denoted as $g_T(\theta)$ and $g_E(\theta)$, respectively, it has been considered that the smaller the following D values, the better becomes the shape resemblance.

$$D = \sum_{\theta_i} \{g_T(\theta_i) - g_E(\theta_i)\}^2 \qquad (4\text{-}9)$$

The summation in Eq. (4-9) was performed by taking 18 values of θ_i with a 10° interval. To find candidate theoretical curves, the volume fraction of each group was varied from 0 to 1 with a 0.1 interval and the aspect ratio k (≥ 1) was changed with a 0.02 interval. For simplicity, the aspect ratios for all the groups were assumed to be the same. Using a computer, the D value for each theoretical curve was calculated and curves with small D values were searched. In the computer calculation, only theoretical curves whose maximum values agree with those of the experimental curves within ± 10% difference were printed out. If only the shape (not the magnitude) of the torque curves is noted, curves with much smaller D values could be obtained. However, since it is difficult to assign a physical meaning to this artificial curve fitting, this method was not adopted in

Table 4-2. Six twin-pair groups of the KS variants.

Group name	#11	#12	#13	#22	#23	#31
Belonging twin pairs	(1-1, 1-4) (2-1, 2-4)	(1-2, 1-5) (4-2, 4-5)	(1-3, 1-6) (3-3, 3-6)	(2-2, 2-5) (3-2, 3-5)	(2-3, 2-6) (4-3, 4-6)	(3-1, 3-4) (4-1, 4-4)

the analysis.

Table 4-3 lists the volume fractions of the groups #11 to #31 and the aspect ratios to best reproduce the experimental torque curves in Figs. 4-3 and 4-4. For each experimental curve, theoretical curves to give five smallest D values are listed. For comparison with Figs. 4-3 and 4-4, theoretical torque curves with the smallest D values shown in Table 4-3 are drawn in Figs. 4-7 and 4-8.

Although the theoretical curves for the as-deformed specimens (Fig. 4-7(a) and Fig. 4-8(a)) do not bear a striking resemblance to the corresponding experimental curves (Fig. 4-3(a) and Fig. 4-4(a)), reasonable agreement can be seen in the shape and magnitude of the theoretical and experimental curves for the annealed specimens. In the experimental torque curves of the as-deformed specimens, Fourier components with $n \geq 6$ were found to be unnegligible. This is the reason why the theoretical curves showed only poor reproducibility. The as-transformed α-iron particles consist of twinned layered structure which was not duly taken into account in the present analysis. Moreover, tangled dislocations as well as significant amount of elastic strains are generated in and around the particles upon the transformation [4, 15]. These may affect the magnetic anisotropy of the as-transformed α-iron particles in many ways. On the other hand, annealing causes the disappearance of twinned structure, tangled dislocations and elastic strains [6, 14, 15]. Therefore, simpler torque curves can reasonably be expected.

We find from Table 4-3 that the present analysis clearly shows the preferential formation of particular KS variants and the development of the shape change (from the values of k) of the α-iron particles. Although it is difficult to accurately determine the volume fraction of each group, it can be found easily that the tensile stress induces the preferential formation of group #13 and the compressive stress induces the preferential formation of group #11. It has been found in Chapter 2 that the (1-3, 1-6) twin pair is formed preferentially by the $[419]_f$ tension and (1-1, 1-4) and (2-1, 2-4) twin pairs are formed by the $[419]_f$ compression. Therefore, the present results are in good agreement with those of the previous study.

We have seen that the present unique method of the magnetic anisotropy measurement is useful. This method may have potential applications not only to find the martensite variants but also to know the texture in deformed or transformed specimens.

4.5. Summary and conclusions

Stress-induced γ→α martensitic transformation was introduced in iron particles in a copper

Table 4-3. Calculated aspect ratios and volume fractions of the twin-pair groups to reproduce the experimentally obtained torque curves in Figs. 4-2 and 4-3.

Aspect ratio	Volume fraction #11	#12	#13	#22	#23	#31	D value	Aspect ratio	Volume fraction #11	#12	#13	#22	#23	#31	D value
Specimens deformed in tension by 14% at 77K															
As-deformed (0 min annealed)								15 min annealed							
1.18	0.2	0	0.5	0	0.3	0	0.258	1.22	0.2	0	0.7	0.1	0	0	0.144
1.16	0.1	0	0.4	0.2	0.3	0	0.301	1.24	0.3	0	0.7	0	0	0	0.151
1.12	0.2	0	0.5	0.1	0.2	0	0.304	1.28	0.3	0	0.6	0	0	0.1	0.165
1.26	0.1	0	0.4	0.1	0.4	0	0.311	1.26	0.2	0	0.7	0	0.1	0	0.173
1.08	0.3	0	0.5	0.2	0	0	0.359	1.28	0.2	0	0.6	0.1	0.1	0	0.176
5 min annealed								10 h annealed							
1.28	0.3	0	0.6	0	0.1	0	0.241	1.32	0.3	0	0.6	0.1	0	0	0.175
1.22	0.3	0	0.6	0.1	0	0	0.242	1.42	0.3	0	0.6	0	0.1	0	0.181
1.22	0.2	0	0.5	0.3	0	0	0.252	1.54	0.3	0	0.5	0	0.1	0.1	0.202
1.28	0.2	0	0.5	0.2	0.1	0	0.257	1.40	0.3	0	0.5	0.1	0	0.1	0.204
1.24	0	0	0.4	0.5	0.1	0	0.260	1.30	0.2	0	0.6	0.2	0	0	0.223
Specimens deformed in compression by 12% at 77K															
As-deformed (0 min annealed)								1 h annealed							
1.04	0.6	0	0	0.3	0	0.1	2.864	1.24	0.7	0.2	0	0.1	0	0	0.091
1.04	0.5	0.1	0	0.4	0	0	3.067	1.22	0.8	0.2	0	0	0	0	0.101
1.04	0.6	0	0	0.4	0	0	3.268	1.20	0.8	0.1	0	0	0.1	0	0.105
1.04	0.5	0	0	0.5	0	0	3.348	1.24	0.7	0.1	0	0	0.1	0.1	0.111
1.06	0.5	0	0	0.3	0	0.2	3.384	1.30	0.7	0.1	0	0	0	0.2	0.114
5 min annealed								1 d annealed							
1.16	0.9	0.1	0	0	0	0	0.189	1.56	0.7	0.3	0	0	0	0	0.241
1.18	0.8	0.1	0	0.1	0	0	0.193	1.70	0.6	0.2	0	0	0.1	0.1	0.247
1.24	0.7	0.1	0	0.1	0	0.1	0.205	1.54	0.6	0.2	0	0	0.2	0	0.247
1.20	0.8	0.1	0	0	0	0.1	0.217	1.98	0.6	0.2	0	0	0	0.2	0.253
1.16	0.9	0	0	0	0.1	0	0.219	1.94	0.5	0.1	0	0	0.2	0.2	0.254

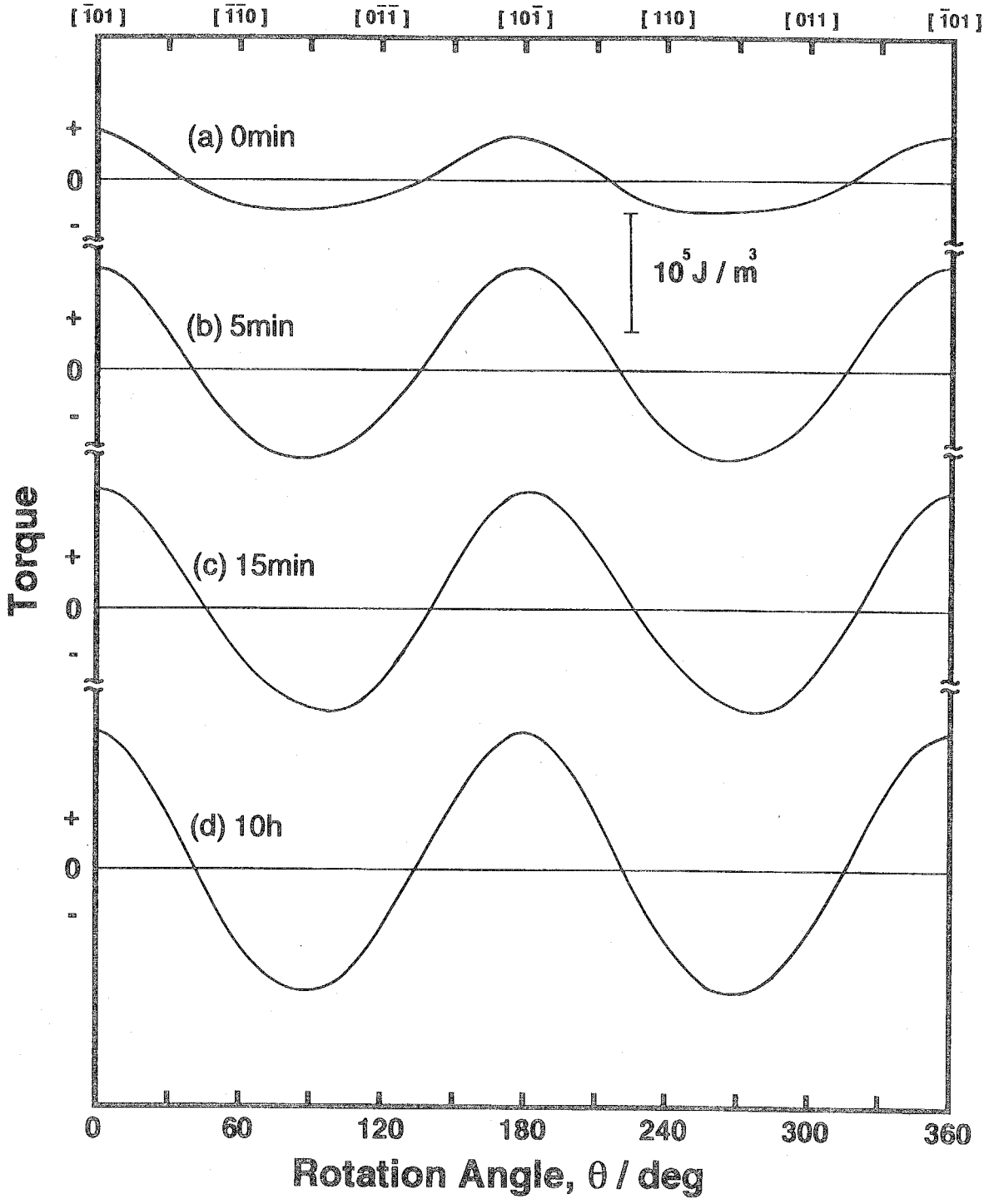

Fig. 4-7. Theoretically caluculated torque curves which best reproduce the experimentally obtained curves in Fig. 4-3.

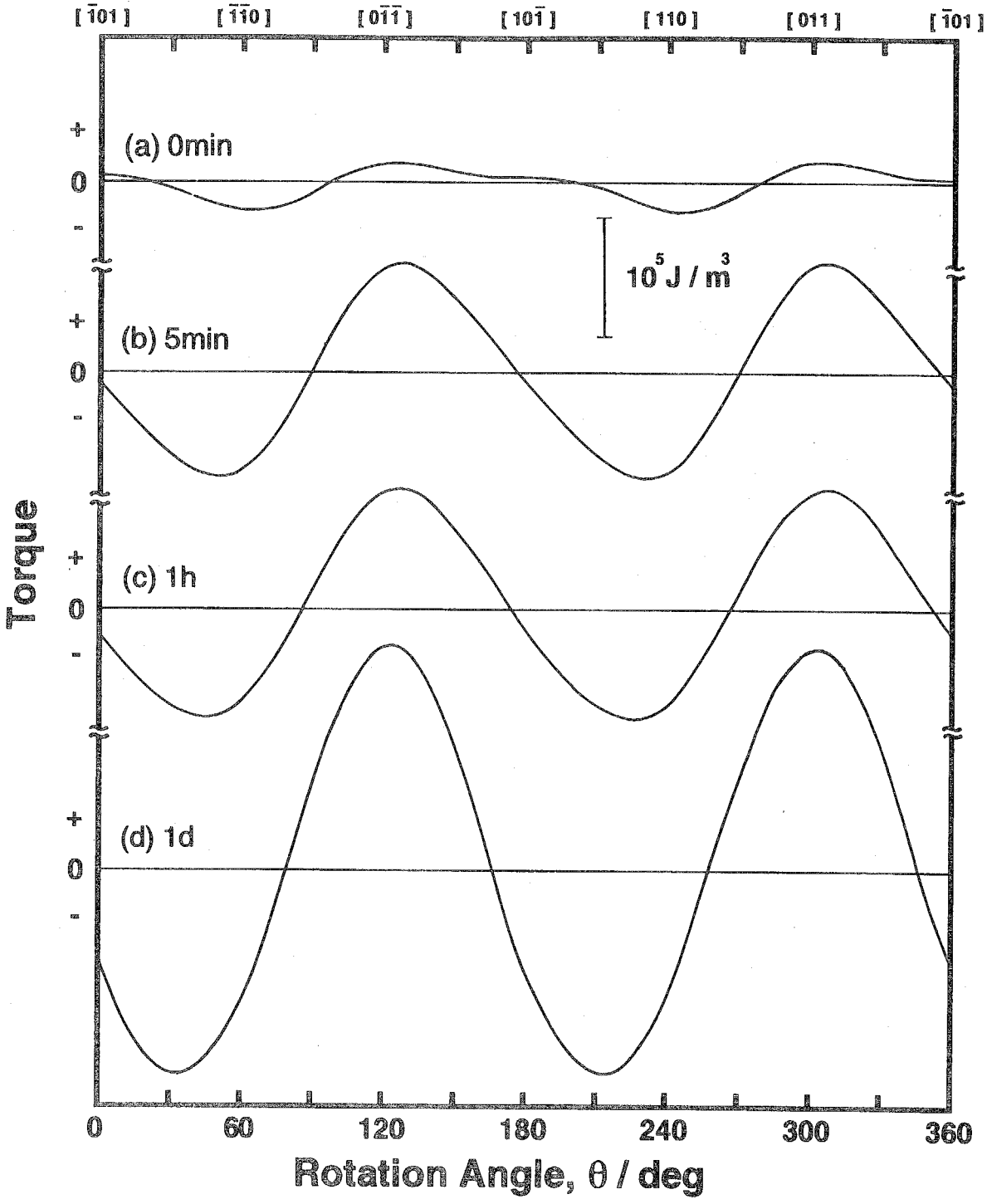

Fig. 4-8. Theoretically calculated torque curves which best reproduce theexperimentally obtained curves in Fig. 4-4.

matrix by applying tensile or compressive stresses along $[419]_f$. The magnetic anisotropy of the deformed and successively annealed specimens was examined by measuring magnetic torque around $(\bar{1}1\bar{1})_f$. The annealing caused the elongation of the α-iron particles to become ellipsoidal in shape. The magnetic anisotropy in the present specimens has two origins, the crystal anisotropy due to the symmetry of the α-iron crystal and the shape anisotropy due to the shape of the α-iron particles. By analyzing the magnetic torque curves, the following results were obtained.

(1) The shape (the phase angle) of the torque curves depends strongly on the sense (tention or compression) of the applied stress while the amplitude of the torque curves becomes larger as annealing time increases.

(2) The stress-dependent shape reflects the preferential formation of particlar stress-induced martensite variants out of crystallographically equivalent ones.

(3) The annealing time-dependent growth of the amplitude of torque curves reflects the spherical to ellipsoidal shape change of the α-iron particles.

(4) These results are in good agreement with those of the TEM observations in Chapter 2.

References

[1] Y. Higo, F. Lecroisey and T. Mori: *Acta Metall.*, **22** (1974),313.

[2] M. Kato and T. Mori: *Acta Metall.*, **24** (1976), 853.

[3] M. Kato and T. Mori: *Acta Metall.*, **25** (1977), 951.

[4] M. Kato, R. Monzen and T. Mori: *Acta Metall.*, **26** (1978), 605.

[5] A. Sato, M. Kato, Y. Sunaga, T. Miyazaki and T. Mori: *Acta Metall.*, **28** (1980), 367.

[6] R. Monzen, A. Sato and T. Mori: *Trans. JIM*, **22** (1981), 65.

[7] K. R. Kinsman, J. W. Sprys and R. J. Asaro: *Acta Metall.*, **23** (1975), 1431.

[8] T. Fujii, M. Kato and T. Mori: Mater. *Trans., JIM*, **32** (1991), 229.

[9] K. Hoselitz: *Physical Metallurgy*, ed. by R. W. Cahn, North-holland, Amsterdam, (1965), 1015.

[10] M. Kato, T. Fujii, Y. Hoshino and T. Mori: *J. Jap. Inst. Met.*, **56** (1992), 865.

[11] Y. Watanabe, H. Nozaki, M. Kato and A. Sato: *Acta Metall. Mater.*, **39** (1991), 3161.

[12] H. Gengragel and U. Hofmann: *Phys. Stat. Solid.*, **29** (1968), 91.

[13] R. M. Bozorth: *Ferromagnetism*, D. Van Nostrand Company, New York, (1951), 849.

[14] T. Fujii, T. Mori and M. Kato: *Acta Metall. Mater.*, to appear.

[15] R. Monzen and M. Kato: *ISIJ Int.*, **30** (1990), 226.

Chapter 5.

Crystallography and Morphology of Needle-like α-Iron Particles in a Copper Matrix

5.1. Introduction

Monzen *et al.* have found that annealing of a Cu-Fe alloy with transformed particles results in the disappearance of the twinned microstructure and the α-iron particles eventually become single crystals [1]. In Chapter 3, annealing experiments were conducted to examine the morphological changes and growth kinetics of the α-iron particles [2]. It has been found that prolonged annealing causes the preferential growth of the single-crystalline particles along certain crystallographic directions and they become needle-like with the aspect ratio as large as 15. In this study, the morphology and crystallography of the elongated α-iron particles will be investigated in more detail.

The microstructure of needle-like precipitate particles has been examined by transmission electron microscopy (TEM) for various alloy systems [3-9]. To explain the crystallography of precipitates such as growth directions and orientation relationships, geometrical analyses based on the invariant-line strain criterion have been found to be very effective. For example, Dahmen has shown that the needle directions of various h.c.p. precipitates in b.c.c. matrices lie along invariant lines [5]. Homogeneous deformation to transform a matrix lattice into a parent lattice results in the formation of a cone of unextended lines if two of the three principal distortions are greater or less than unity [5-8]. Taking into account the accommodation by the matrix slip, Dahmen *et al.* predicted that semicoherent needle-like precipitates grow along the intersections of the cone of unextended lines with matrix slip planes [6, 7]. Such slip accommodation is necessary to form a set of shear dislocation loops at the precipitate-matrix interface. However, when the growth of precipitates occurs at high enough temperatures for diffusional accommodation to take place, the matrix slip may not be an important factor in determining the growth directions.

Luo and Weatherly examined in detail the crystallography of needle-like chromium precipitates in nickel [8]. They concluded that the invariant-line criterion was excellently applicable to explain not only the observed growth directions but also the habit-plane orientations. However, in conducting the analysis, they assumed the exact KS relationship between the two crystals. With this assumption, the invaliant-line condition was realized only approximately.

In the present study, without assuming the role of matrix slip or the orientation relationship, the crystallography of the fully-grown needle-like α-iron precipitates in the copper matrix will be

examined and analyzed. For this purpose, the geometrical criteria, originally developed to explain epitaxial relationships at deposit-substrate interfaces [10], will be adopted and their applicability to the crystallography of precipitate-matrix interfaces will be examined.

5.2. Experimental

Tensile specimens of $3\times3\times40$ mm^3 in size with the tensile axis parallel to the [419] direction were spark-cut from single crystals of a Cu-1.0mass%Fe alloy. The specimens were solution treated at 1273K for 4h and quenched into water. The specimens were then aged at 973K for 1d. This treatment produced γ-iron precipitate particles with the average radius of 29nm. To introduce the γ→α martensitic transformation in all the particles, the specimens were deformed in tension by 20% at 77K.

Fully-elongated single-crystalline α-iron particles in the copper matrix were obtained by annealing the deformed specimens at 973K for 4d. From these specimens, thin foils for 200kV TEM (Hitachi H-700) were prepared so that the foil surfaces became parallel to either the $(\bar{1}1\bar{1})$ primary slip plane or the (110) plane of the copper matrix.

5.3. Results

5.3.1. Growth directions of α-iron precipitates

Figure 5-1 shows a TEM micrograph of elongated α-iron precipitates. As mentioned in Chapter 2, only a few KS variants out of 24 crystallographically equivalent ones are predominantly formed if a uniaxial stress is applied to induce the martensitic transformation in the iron particles [11]. This explains the fact that the elongated directions of most precipitates are well aligned along the $[110]_f$ direction. However, the detailed examination of more than 100 precipitates revealed that two distinct growth directions on the $(\bar{1}1\bar{1})_f$ plane, one parallel to $[110]_f$ and the other $8.5°\pm1°$ away from $[110]_f$, *i.e.* near $[16\ 19\ 3]_f$, exist in approximately equal amounts, as shown in Fig. 5-1. The precipitates belonging to the former and the latter will be referred to as variants I and II, respectively.

The selected-area diffraction pattern in Fig. 5-2(a) was taken from an area containing several variant I and II precipitates in Fig. 5-1. It can be seen from the schematic representation in Fig. 5-2(b) that two nearly KS variants which are twin-related to each other are present. An analysis using dark-field micrography revealed that these variants corresponded to the above variants I and II

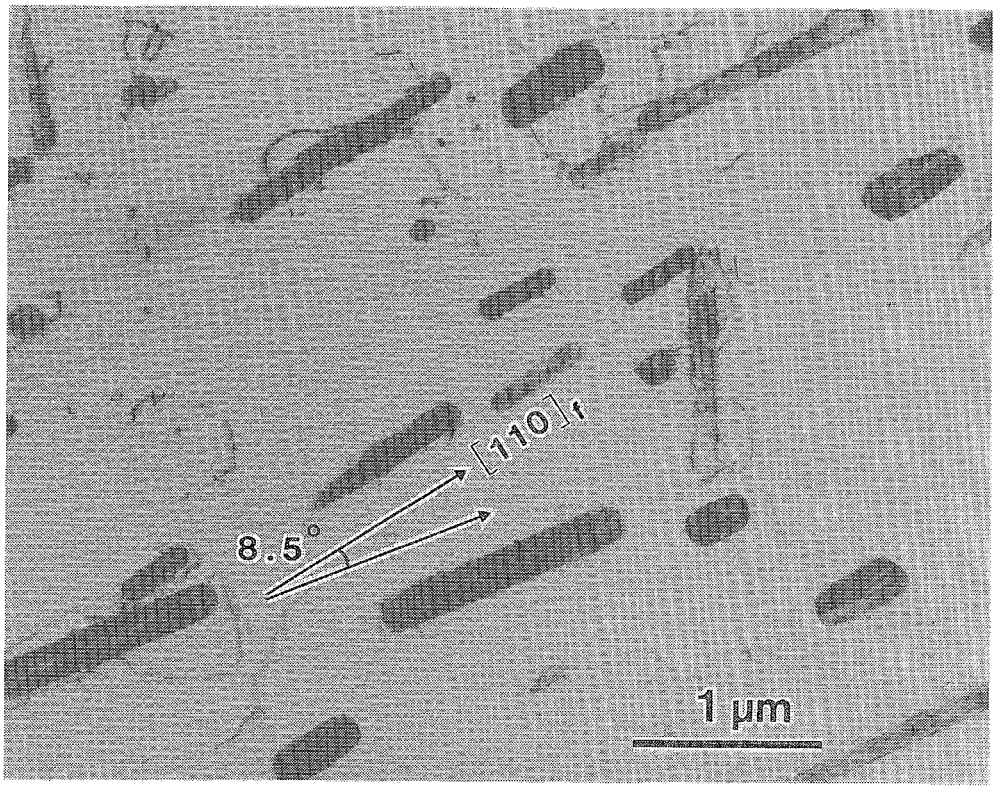

Fig. 5-1. Transmission electron micrograph of elongated α-iron precipitate particles in a copper matrix. Two growth directions, $[110]_f$ for variant I and $[16\ 19\ 3]_f$ for variant II, can be seen. zone axis: $[\bar{1}1\bar{1}]_f$.

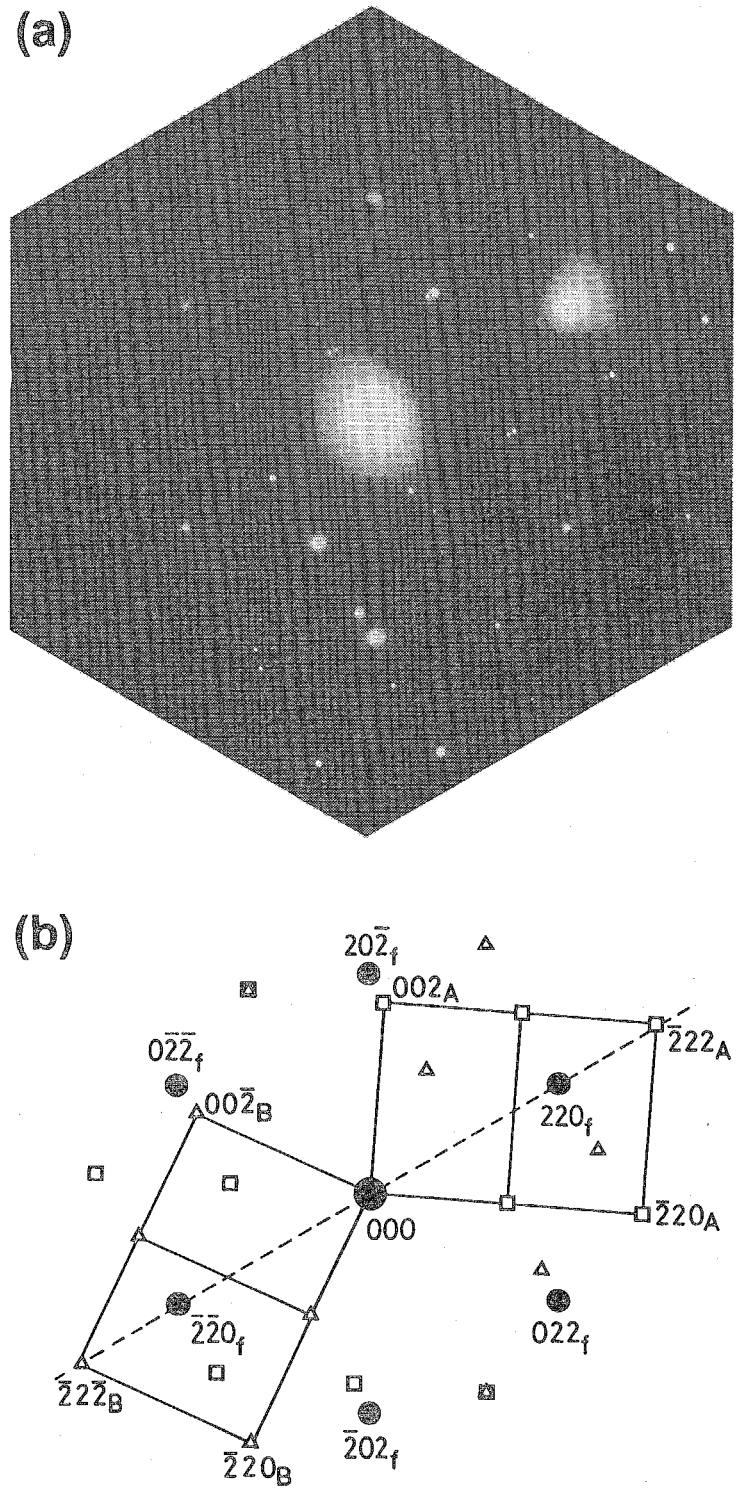

Fig. 5-2. Selected-area diffraction pattern (a) and its schematic representation (b) showing the superposition of the $Cu[\bar{1}1\bar{1}]_f$ pattern and two twin-related $Fe[110]_b$ patterns with KS orientation relationships.

with the orientation relationships described by:

$(\bar{1}1\bar{1})_f // (110)_b$, $[110]_f // [\bar{1}11]_b$ (variant I)

$(\bar{1}1\bar{1})_f // (110)_b$, $[\bar{1}\bar{1}0]_f // [\bar{1}1\bar{1}]_b$ (variant II).

The variant I is the same as the most predominantly formed 1-6 variant under a [419] uniaxial stress examined in Chapter 2 and the variant II is the same as the 1-3 variant. Hereafter, the variant notation defined in Table 2-1 in Chapter 2 will also be used in this chapter. These variants constitute the α-twins in the layered microstructure in the as-transformed state. It should be emphasized here that the above KS relationships are approximated ones. As already investigated in detail by Monzen and Kato [12, 13], the distribution of orientation relationships, or slight deviation (within 2°) from the exact KS relationship, was recognized when many α-iron precipitates were examined statistically. As particles elongate by the annealing, one of the twinned variants grow at the expense of the other to become single crystals and the growth directions depend on the variants, as shown above. Of course, the growth of particles is accompanied by the disappearance of some others.

5.3.2. Habit-plane orientations of α-iron precipitates

Figure 5-3 shows the cross-sectional view of the variant 1-6 precipitate. The elongation direction, $[110]_f$, is perpendicular to the micrograph. After the anealing at 973K for 4d, most precipitates have so elongated that their longitudinal dimension is larger than the $(110)_f$ foil thickness. As can be seen in Fig. 5-3, the precipitate-matrix interface consists of several facets of habit planes. Comparison with a selected-area difraction pattern revealed that the orientations of these facets were approximately described as $(\bar{1}1\bar{1})_f/(110)_b$, $(\bar{1}1\bar{2})_f/(321)_b$, $(\bar{1}11)_f/(\bar{1}4\bar{5})_b$ and $(3\bar{3}\bar{2})_f/(0\bar{1}1)_b$. Among them, the $(\bar{1}1\bar{1})_f/(110)_b$ and $(\bar{1}1\bar{2})_f/(321)_b$ habit planes were confirmed to be accurately edge-on when viewed from the exact $[110]_f$ growth direction. These two habit planes were universally observed in all the precipitates examined. Therefore, these habit planes are considered to be predominant for the variant 1-6 precipitates.

The formation of structural ledges at the precipitate-matrix interface can be detected in the upper-right portion of Fig. 5-3. Furthermore, the periodic arrays of strain-field contrasts can be seen in the copper matrix near the precipitate. These are indicative of the existence of interface dislocations.

Although habit-plane facets were also observed in some variant 1-3 precipitates, their

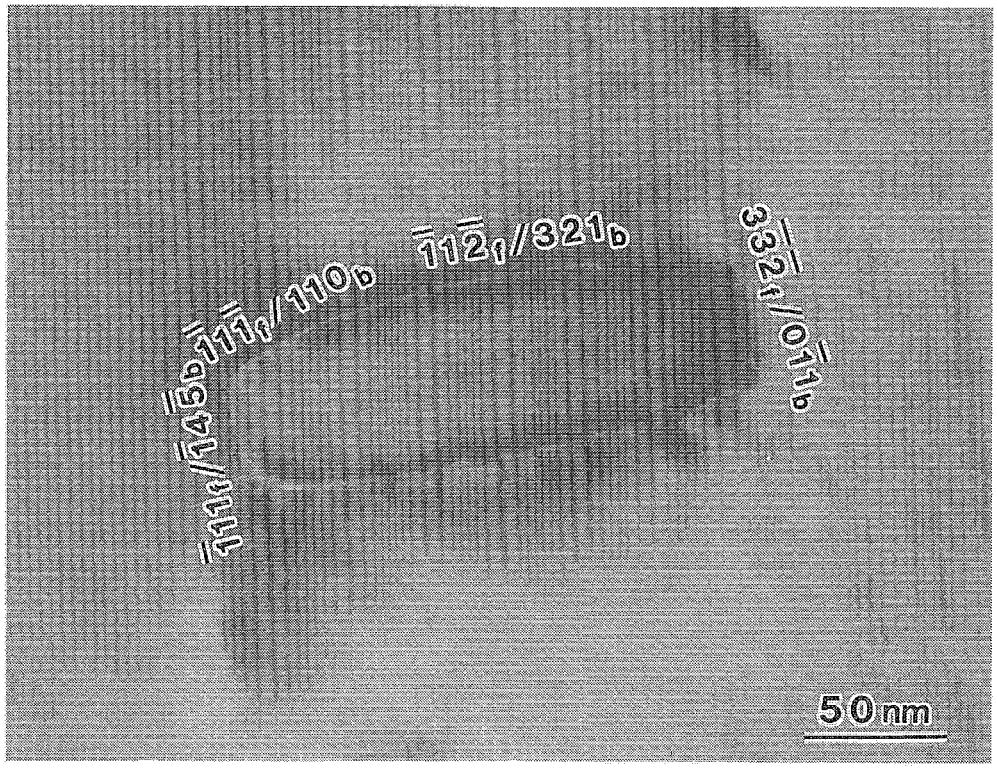

Fig. 5-3. Cross-sectional view of a variant 1-6 precipitate. The $[110]_f$ zone axis is parallel to the growth direction of the precipitate. The Orientations of habit-plane facets are indicated.

orientations were not identified. This is because they became high-index planes and, more importantly, because habit-plane orientations varied from precipitate to precipitate.

Figure 5-4 summarizes the observed crystallographic features of the elongated α-iron precipitates in a stereographic projection. These features will be discussed below.

5.4. Discussion

5.4.1. Orientation relationship

As seen in Fig. 5-2, the KS relationship was observed between the α-iron precipitates and the copper matrix. Here, let us discuss factors determining the orientation relationship. For this purpose, geometrical criteria proposed by Kato *et al.* [14] to predict and explain interface crystallography will be adopted. These criteria were originally developed to discuss the epitaxial relationships between deposit thin films and substrates [14-17] and can be summarized as follows [10].

(i) The f.c.c. and b.c.c. planes to form an interface are related to each other by the Bain correspondence.

(ii) On each plane, two mutually perpendicular directions (x_f and y_f on the f.c.c. plane and x_b and y_b on the b.c.c. plane) can be found uniquely so that x_f and x_b as well as y_f and y_b correspond to each other by the Bain correspondence.

(iii) The orientation relationship is considered to be determind by the invariant-line criterion [5]. Using the lattice parameters of f.c.c. (a_f) and b.c.c. (a_b), the atomic arrangement of the f.c.c. plane can be converted into that of the b.c.c. plane by a homogeneous transformation with the principal distortions η_x and η_y defined as $\eta_x = |x_b|\, a_b/|\, x_f|\, a_f$ and $\eta_y = |y_b|\, a_b/|\, y_f|\, a_f$. With this transformation, the originally circular region on the f.c.c. plane changes into an elliptic region on the b.c.c. plane, as shown in Fig. 5-5. Then, the rotation angle θ to realize the invariant-line condition can be found as [5]

$$\cos\theta = (1 + \eta_x \eta_y)/(\eta_x + \eta_y). \qquad (5\text{-}1)$$

The angle α between the x_f-direction and the invariant line satisfies

$$\tan\alpha = \pm \{(1 - \eta_x{}^2)/(\eta_y{}^2 - 1)\}^{1/2}. \qquad (5\text{-}2)$$

(iv) The relative preference between different orientation relationships can be evaluated by comparing

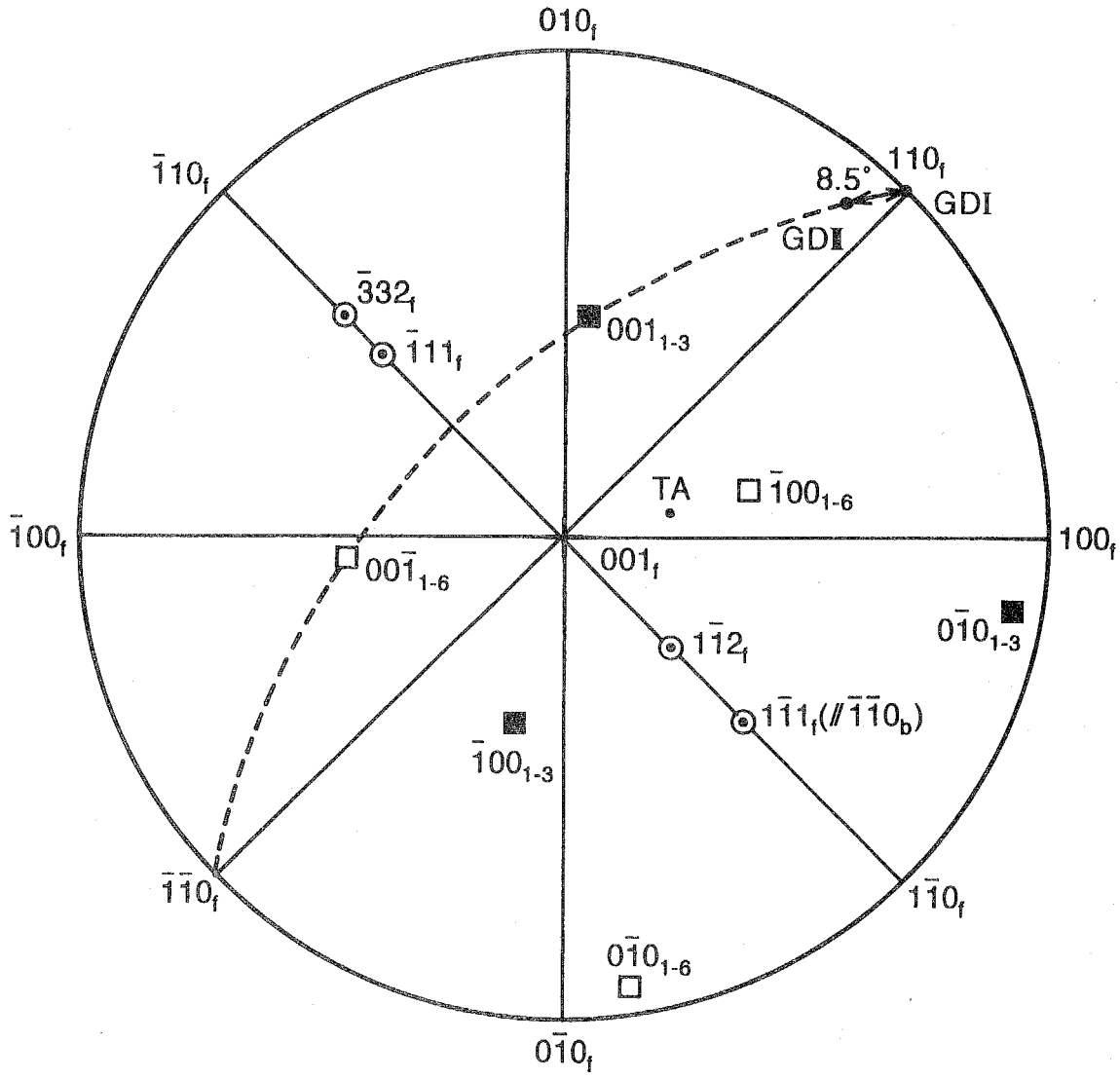

TA : tensile axis $[419]_f$

GDI : growth direction of variant 1-6

GDII : growth direction of variant 1-3

⊙ : habit plane nomals for variant 1-6

□ : 100-type poles for variant 1-6 KS relationship

■ : 100-type poles for variant 1-3 KS relationship

Fig. 5-4. 001_f stereographic projection showing the crystallographic features of the elongated α-iron precipitates in the copper matrix.

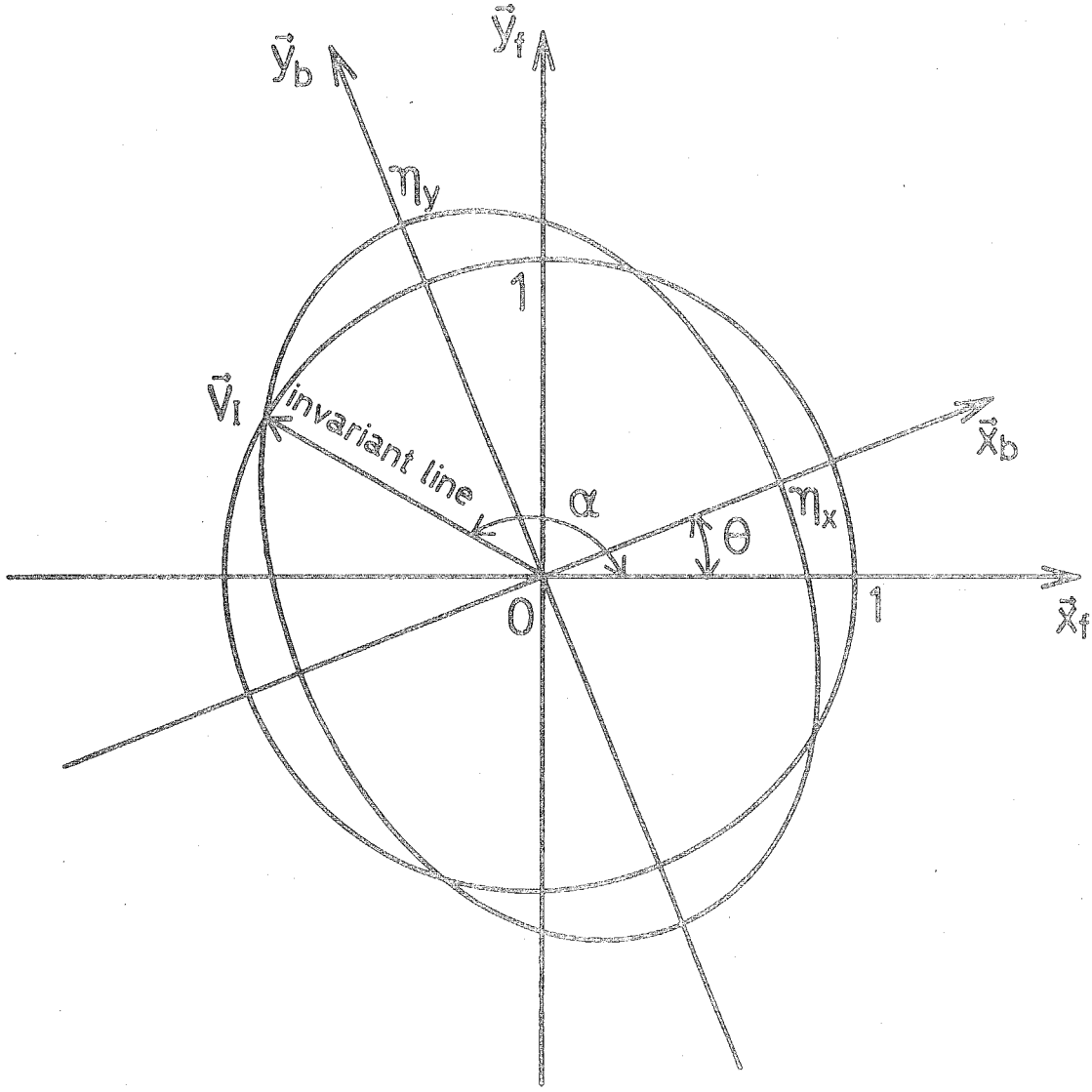

Fig. 5-5. Homogeneous deformation with principal distortions η_x and η_y changes the circular region of an f.c.c. plane into the elliptic region of a Bain-corresponding b.c.c. plane. The invariant-line direction parallel to V_I appears by the θ rotation of the ellipse with respect to the circle.

the following M parameter values. This parameter is approximately proportional to the strain energy density due to the lattice misfit between the two crystal planes at the interface: The relationship with a smaller M value is more preferable.

$$M = \varepsilon_x^{\,2} + \varepsilon_y^{\,2} + (2/3)\varepsilon_x \varepsilon_y, \tag{5-3}$$

where $\varepsilon_x = \eta_x - 1$ and $\varepsilon_y = \eta_y - 1$.

Although the above criteria were constructed to treat the crystallography of two-dimensional flat interfaces, they were found to be excellently applicable even for three-dimensional problems if the atomic arrangements of various local planes on a curved inteface were considered [18, 19]. Therefore, it is physically sound and worthwhile to adopt these four criteria to the present study. To do so, a pair of crystal planes to describe an orientation relationship must first be determined. It is assumed that the α-iron precipitates can grow most easily if the growth directions lie on a pair of optimum matching planes. Among numerous possibilities, we will consider the three lowest-index planes, *i.e.* (100),(110) and (111), as the orientations of the f.c.c. and b.c.c. planes. Then, the Bain correspondence leads to four different candidate orientations of the f.c.c. and b.c.c. planes. They are shown in Table 5-1. It is seen from Table 5-1 that these four orientations are sufficient to describe such familiar relationships as KS, Nishiyama-Wassermann (NW), Pitsch (P) and Bain (B).

On each orientation, a set of principal directions, x_f, y_f, x_b and y_b can be found uniquely using Table 1 in Ref. [10]. From these and $a_f = 0.3615$nm for copper and $a_b = 0.2867$nm for iron, η_1 and η_2 can be calculated. The values of θ (criterion (iii)) and M (criterion (iv)) are thus obtained from Eqs. (5-1) and (5-3). They are also listed in Table 5-1.

By comparing the M values for the four orientations, it can be found that the M value (0.0151) for $(111)_f/(110)_b$ is much smaller than the M values for the other three orientations. According to criterion (iv), this means that the $(111)_f/(110)_b$ orientation is most preferable. Moreover, the rotation angle $\theta = 5.75°$ to realize the invariant-line condition for this orientation is very close to $\theta = 5.26°$ for the exact KS relationship and is by far different from $\theta = 0°$ for the NW relationship. Therefore, the present analysis concludes that approximately the KS relationship should be realized between the iron particles and the copper matrix. This is in agreement with the experimental observation. Since actual orientation relationships vary slightly from precipitate to precipitate, the relevance of the predicted 0.49° deviation from the exact KS relationship cannot be discussed in the light of experimental results. However, the deviation is thought to be small enough to show the

Table 5-1. Orientations of Bain-corresponding low-index f.c.c. and b.c.c. planes. On each orientation, a set of principal directions and their calculated values of η_x, η_y, M and θ for the Cu-Fe system are shown. The belonging familiar orientation relationships are also listed together with their θ values.

	$(100)_f$ / $(100)_b$	$(100)_f$ / $(110)_b$	$(110)_f$ / $(100)_b$	$(111)_f$ / $(110)_b$
x_f	$[001]_f$	$[001]_f$	$[002]_f$	$[1\bar{2}1]_f$
y_f	$[010]_f$	$[010]_f$	$[\bar{1}10]_f$	$[\bar{1}01]_f$
x_b	$[0\bar{1}1]_b$	$[001]_b$	$[002]_b$	$[2\bar{2}0]_b$
y_b	$[011]_b$	$[\bar{1}10]_b$	$[020]_b$	$[002]_b$
Cu-Fe System				
η_x	1.1216	0.7931	0.7931	0.9158
η_y	1.1216	1.1216	1.1216	1.1216
θ	——(0°)	9.30°	9.30°	5.75°
M	0.0394	0.0408	0.0408	0.0151
Belonging familiar orientation relationship	B(θ=0°)	P(θ=9.74°)	NW(θ=9.74°)	NW(θ=0°) KS(θ=5.26°)

excellent applicability of criterion (iii) in the present study.

5.4.2. Growth directions

Now that we have seen the excellent applicability of the above four criteria to explain the observed orientation relationship, they will also be adopted to analyze the observed growth directions. As shown before, the two distinct growth directions, $[110]_f$ for the variant 1-6 and $[16\ 19\ 3]_f$ for the variant 1-3, were observed. The former direction is parallel to the $[\bar{1}11]_b$ direction of the variant 1-6 and, therefore, this growth direction may be understood if we intuitively assume that preferential growth occurs along the common close-packed direction. This assumption may be justified since the lattice misfit along $[110]_f/[\bar{1}11]_b$ is only 3%.

On the other hand, the growth direction for the variant 1-3 cannot be understood intuitively. According to previous studies in literature [5-8], such high-index growth directions often coincide with the directions of invariant lines. To examine whether the same invariant-line criterion is applicable for the present variant 1-3 precipitates, criterion (iii) will be considered. We have seen in the previous section that the $(\bar{1}1\bar{1})_f/(110)_b$ orientation holds. Figure 5-6 shows the superposition of $(\bar{1}1\bar{1})_f$ and $(110)_b$ planes satisfying the rotation angle $\theta = 5.75°$ calculated from Eq. (5-1) and shown in Table 5-1. The direction of the invariant line, or the angle α between x_f and the invariant-line direction, can then be calculated from Eq. (5-2) as $\alpha = 141.66°$. Therefore, it is easy to find from Fig. 5-6 that the invariant-line direction is 8.34° away from $[110]_f$. This is in excellent agreement with the observed angle, 8.5° ± 1°.

The applicability of the invariant-line criterion to explain the growth direction is not limited to precipitate-matrix systems. Kato *et al.* have shown that the growth direction of deposit thin films of iron on Cu and Cu-Ni substrates can also be explained by the invariant-line criterion [10, 14-17]. Since no lattice misfit exists along the invariant line, the growth of precipitates and thin films is considered to take place easily.

A question then arises as to why the growth direction of the variant 1-6 precipitates did not coincide with the invariant-line direction. At present, it isdifficult to answer this question clearly. However, it is worth mentioning that although the 1-6 and 1-3 precipitates have crystallographically equivalent orientation relationships to the copper matrix, the variants 1-6 and 1-3 are different from the viewpoint of stress-induced martensite products. As investigated in Chapter 2, the variant 1-6 precipitates are those which are preferentially formed by the applied stress. On the other hand, the variant 1-3 precipitates are formed as a result of plastic accommodation by twinning in the α-iron particles due to the constraint of the surrounding copper matrix [11, 20]. Such a difference in the

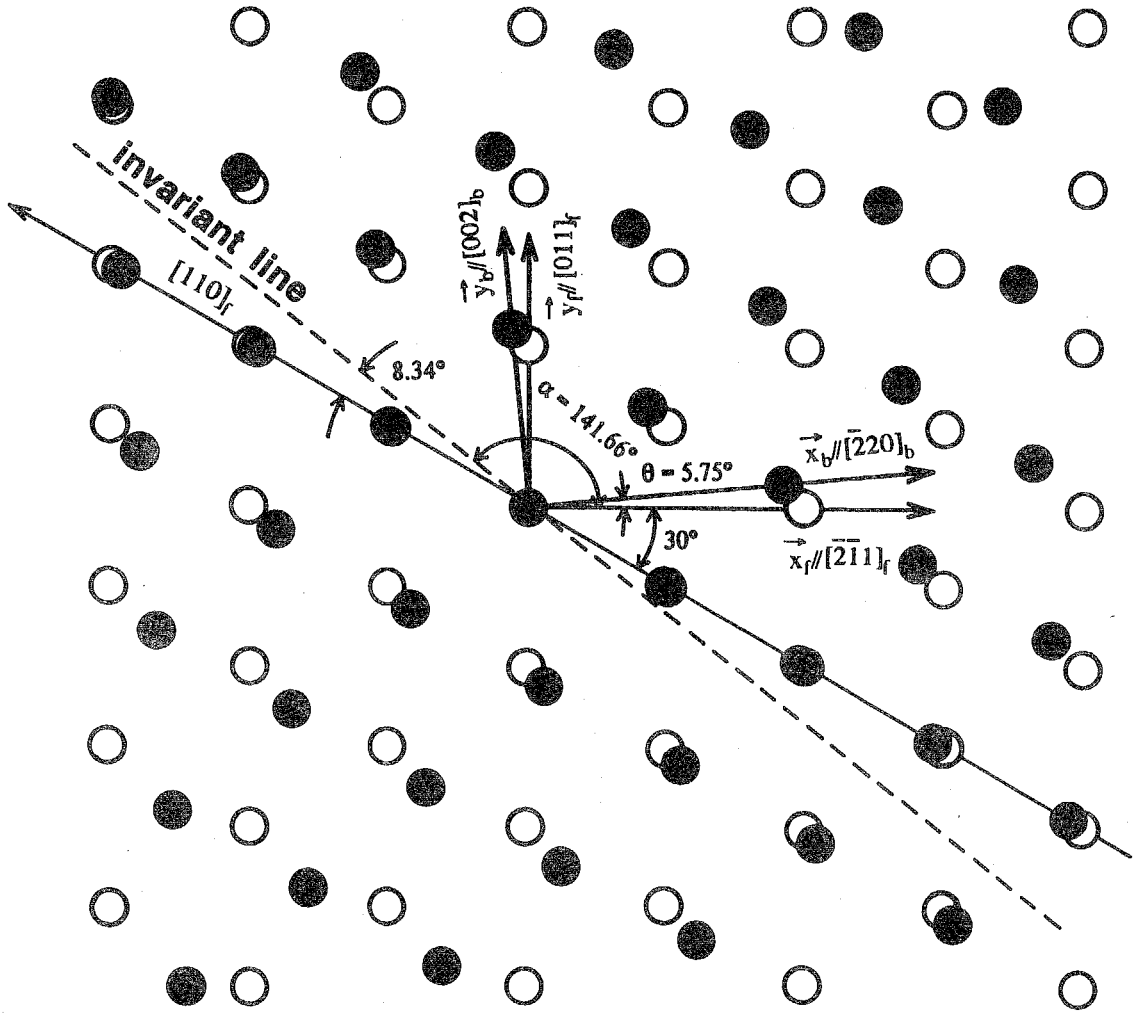

Fig. 5-6. Superposition of the $(\bar{1}1\bar{1})_f$ and $(110)_b$ planes so as to satisfy the invariant-line condition. ○: f.c.c. atoms, ●: b.c.c. atoms.

initial formation process of the two variants may affect the morphological changes during the annealing.

5.4.3. Habit-plane orientations

As shown in Section 5.3.2, the main habit-plane orientations observed for the variant 1-6 precipitates were $(\bar{1}\,1\,\bar{1})_f/(110)_b$ and $(\bar{1}\,1\bar{2})_f/(321)_b$. Adopting criteria (i) to (iv), we will discuss the reason why these two habit planes are predominant.

Figure 5-7 shows the superposition of 110_f and 111_b stereographic projections to indicate the observed KS relationship for the variant 1-6. It should be noted that the $[110]_f/[\bar{1}\,11]_b$ direction is the growth direction of the variant 1-6 precipitates and, therefore, the habit plane poles should lie on the peripheral great circle in the stereographic projection.

Let us assume that $(hkl)_f$ and $(pqr)_b$ are a pair of Bain-corresponding planes containing $[110]_f$ and $[\bar{1}\,11]_b$. Criterion (iv) will be adopted to find preferable $(hkl)_f/(pqr)_b$ pairs to form habit planes. It is of course true that the $(hkl)_f$ and $(pqr)_b$ planes are uniquely determined as $(\bar{1}\,1\,\bar{1})_f$ and $(110)_b$, respectively, for the exact KS relationship. This is because these are the only pair of Bain-corresponding planes which are exactly parallel to each other. In other words, if δ is defined as the angle between $(hkl)_f$ and $(pqr)_b$, $\delta = 0°$ for the KS relationship is satisfied only for $(\bar{1}\,1\,\bar{1})_f$ and $(110)_b$. Therefore, the observed $(\bar{1}1\bar{1})_f/(110)_b$ habit plane is a very natural one for the variant 1-6 precipitates. However, if we allow a small deviation from the exact KS relationship, which may well be the case for the present Cu-Fe system, many other candidate pairs of planes can be considered.

We asume rather arbitrarily that if δ is smaller than 1°, the two planes may constitute a habit plane with nearly the KS relationship. We further assume that extremely high-index planes are unlikely to form an interface for the variant 1-6 precipitates.* Therefore, we limit ourselves to the planes satisfying $h^2+k^2+l^2<30$ and $p^2+q^2+r^2<30$, where all the indices are integers. With the above in mind, possible pairs of Bain-corresponding planes were searched and only three pairs as listed in Table 5-2 were found. Using criteria (iii) and (iv), the M values for these pairs were

*It is true that high-index habit planes satisfying the invariant-plane condition are often observed for plate martensites. During diffusionless martensitic transformations, the relaxation of a constraint imposed by the matrix occurs entirely by plastic deformation. This inevitably makes the martensite crystallography rather complicated as discussed in the phenomenological crystallographic theories [21, 22]. On the other hand, since the diffusional rearrangement of atoms occurs easily during the growth of precipitates, extensive plastic deformation as a relaxation mechanism is not needed. Therefore, much simpler crystallography is expected to be realized.

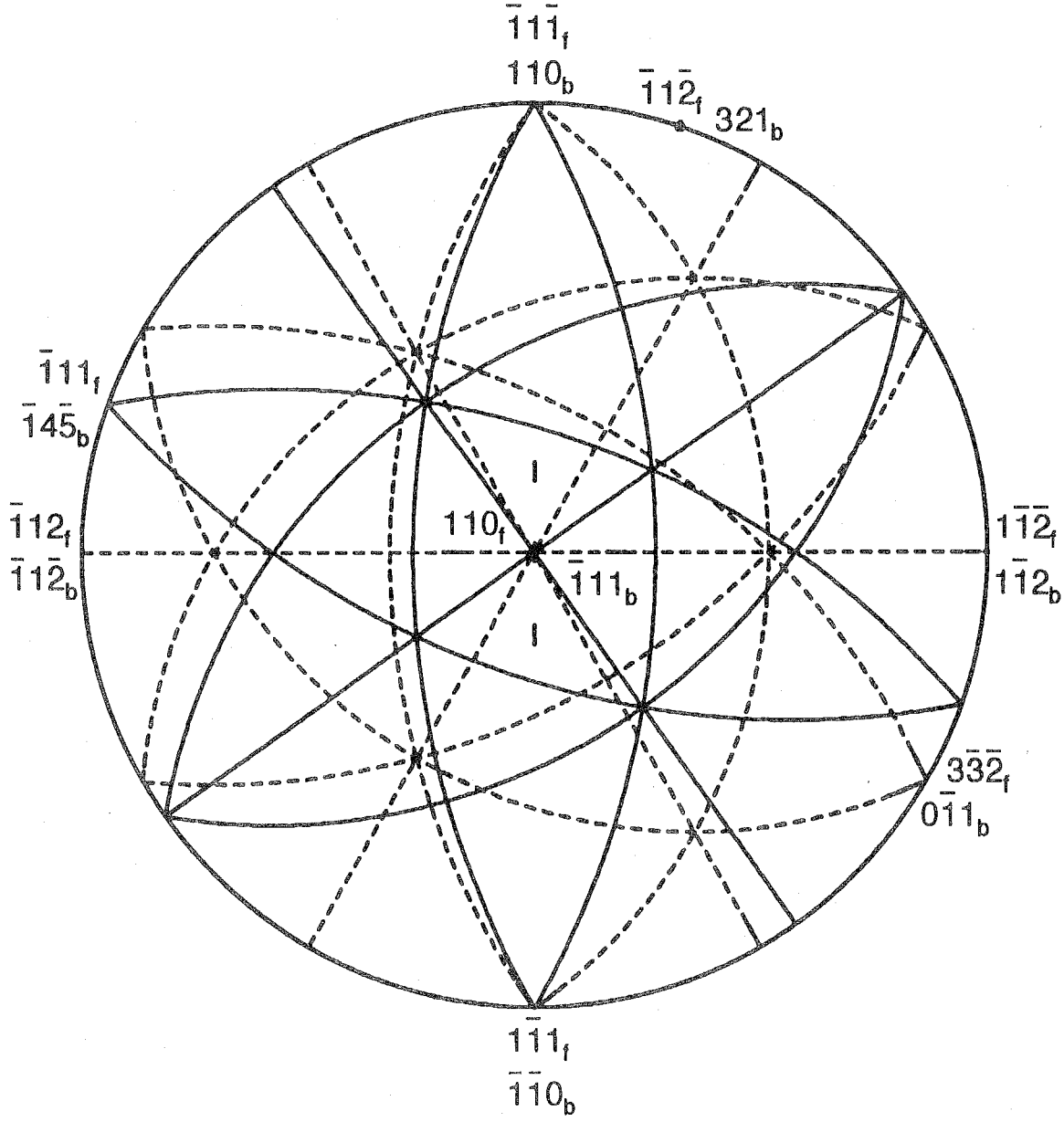

Fig. 5-7. Superposition of 110_f (solid lines) and $\bar{1}11_b$ (dotted lines) stereographic projections indicating the observed KS relationship for variant 1-6.

Table 5-2. Possible combinations of Bain-corresponding f.c.c. and b.c.c. planes which can nearly satisfy the KS relationship for variant 1-6. Calculated values of M and δ, the deviation angles from the exact KS relationship, are shown for each combination.

$(h\,k\,l)_f$ / $(p\,q\,r)_b$	δ	M
$(\bar{1}1\bar{1})_f$ / $(110)_b$	0°	0.0151
$(\bar{1}1\bar{2})_f$ / $(321)_b$	0.36°	0.0237
$(\bar{1}1\bar{3})_f$ / $(211)_b$	0.50°	0.0303

calculated and they are also shown in Table 5-2. It can be seen that the $(\bar{1}\,1\,\bar{1})_f/(110)_b$ and $(\bar{1}\,1\,\bar{2})_f/(321)_b$ pairs have smaller M values than the $(\bar{1}\,1\,\bar{3})_f/(211)_b$ pair. Therefore, criterion (iv) predicts that the former two pairs are more favorable habit planes. This is again in agreement with the observed two main habit plane orientations.

As mentioned in Section 5.3.2, no common habit plane was found for the variant 1-3 precipitates. However, the above analysis predicts that the $(\bar{1}\,1\,\bar{1})_f/(110)_b$ interface can also be a favorable habit plane for this variant since this plane contains the $[19\ 16\ 3]_f$ growth direction. Further studies are necessary to understand why this plane did not become a common habit plane.

5.4.4. Comparison with other studies

As we have seen, the proposed criteria (i) to (iv) for interface crystallography are excellently applicable. Although the invariant-line criterion also plays an important role, the basic idea behind the present analysis is, to some extent, different from those proposed by Dahmen *et al.* [6, 7]. As mentioned in Section 5.1, they have predicted that the growth directions of semicoherent precipitates should coincide with the intersections of the cone of unextended lines and matrix slip planes. Of the two observed growth directions, $[16\ 19\ 3]_f$ for the variant 1-3 is in agreement with this prediction since this direction lies on both the cone of unextended lines and the $(\bar{1}\,1\,\bar{1})_f$ slip plane. However, since $[110]_f$ was also observed, we did not explain the growth directions in connection with the accommodation by matrix slip. Rather, we have simply assumed that the growth of precipitates is easy along certain directions on the optimum matching interface plane, $(\bar{1}\,1\,\bar{1})_f/(110)_b$. It is true that the periodic arrays of strain-field contrasts, indicative of the existence of interface dislocations, were in fact observed, as shown in Fig. 5-3. However, we do not believe that the matrix slip played a crucial role in accommodating the lattice misfit. This is because the growth of the α-iron particles occurred at 973K for 4d. Under such growth conditions, diffusional accommodation would occur easily.

In discussing the crystallography of needle-like chromium precipitates in a nickel matrix, Luo and Weatherly conducted a three-dimensional crystallographic analysis by assuming the exact KS relationship between the two crystals [8]. With this assumption, one has an impression that the orientation relationship is pre-determined by some unknown causes and then other crystallographic features are realized so that they are consistent with the given orientation relationship. On the other hand, in this study, it has been considered that the orientation relationship is determined as a result of finding an optimum matching pair of two crystal planes. In fact, by conducting the same analysis as in Section 5.4.1 with $a_f = 0.3524$nm for Ni and $a_b = 0.2880$nm for Cr, we find that the

$(\bar{1}1\bar{1})_f/(110)_b$ combination with $\theta = 5.24°$ is most preferable. Since this angle is almost the same as that for the exact KS relationship (5.26°), there is no need to assume the KS relationship in conducting the crystallographic analysis.

5.5. Summary and conclusions

The crystallography and morphology of needle-like α-iron precipitates in a copper matrix were examined. Simple geometrical criteria for interface crystallography were applied to explain the experimental results. The main findings are summarized as follows.

(1) The Kurdjumov-Sachs orientation relationships were observed between the precipitates and the matrix.

(2) Depending on the Kurdjumov-Sachs variants, two growth directions, $[110]_f$ and $[16\ 19\ 3]_f$, were observed.

(3) The precipitate-matrix interface consisted of several facets of habit planes. The predominant habit plane orientations for the $[110]_f$ needles were $(\bar{1}1\bar{1})_f/(110)_b$ and $(\bar{1}1\bar{2})_f/(321)_b$.

(4) The observed crystallography and morphology of the α-iron precipitates were explained excellently by combining the invariant-line deformation criterion and the strain-energy minimization criterion.

References

[1] R. Monzen , A. Sato and T. Mori: *Trans. JIM*, **22** (1981), 65.

[2] T. Fujii, M. Kato and T. Mori: *Mater. Trans., JIM*, **32** (1991), 229.

[3] G. C. Weatherly, P. Humble and D. Borland: *Acta Metall.*, **27** (1979), 1815.

[4] A. Crosky, P. G. McDougall and J. S. Bowles: *Acta Metall.*, **28** (1980), 1495.

[5] U. Dahmen: *Acta Metall.*, **30** (1982), 63.

[6] U. Dahmen and K. H. Westmacott: *Proc. Int. Conf. Solid-Solid Trans.*, TMS-AIME, New York, (1982), p.433.

[7] U. Dahmen, P. Ferguson and K. H. Westmacott, *Acta Metall.*, **32** (1984), 803.

[8] C. P. Luo and G. C. Weatherly: *Acta Metall.*, **35** (1987), 1963.

[9] C. P. Luo and G. C. Weatherly: *Phil. Mag.*, **A58** (1988), 445.

[10] M. Kato: *Mater. Sci. Eng.*, **A146** (1991), 205.

[11] M. Kato, R. Monzen and T. Mori: *Acta Metall.*, **26** (1978), 605.

[12] R. Monzen and M. Kato: *ISIJ Int.*, **30** (1990), 226.

[13] R. Monzen and M. Kato: *Mater. Sci. Eng.*, **A146** (1991), 181.

[14] M. Kato, M. Wada, A. Sato and T. Mori: *Acta Metall.*, **37** (1989), 749.

[15] M. Kato and T. Mishima: *Phil. Mag.*, **A56** (1987), 725.

[16] M. Kato, T. Kubo and T. Mori: *Acta Metall.*, **36** (1988), 2071.

[17] M. Kato, M. Wada, M. Shibata-Yanagisawa and T. Mori: *J. Phys. (Paris)*, Colloq. C1, **51** (1990), 849.

[18] M. Wada, S. Uda and M. Kato: *Phil. Mag.*, **A59** (1989), 31.

[19] M. Wada, A. Fujii, T. Yoshida and M. Kato: *Phil. Mag.*, **B64** (1991), 485.

[20] T. Mura, T. Mori and M. Kato: *J. Mech. Phys. Solids*, **24** (1976), 305.

[21] M. S. Wechsler, D. S. Lieberman and T. A. Read: *Trans. AIME*, **197** (1953), 1503.

[22] J. S. Bowles and J. K. Mackenzie: *Acta Metall.*, **2** (1954), 129, 138, 224.

Chapter 6.

Growth of Grain-Boundary Precipitates in Cu-Fe-Co Bicrystals

6.1. Introduction

Grain boundaries often become preferential sites for the precipitation and growth of second-phase particles. As a result, grain-boundary particles are in general larger than in-grain particles. It is, however, well known that the distribution and morphology of boundary particles vary with grain boundaries [1-9]. This is because such factors as grain-boundary segregation and grain-boundary diffusion depend on the boundary character.

The growth of boundary precipitate particles has been studied theoretically by many investigators. For example, Speight [10] has shown, as mentioned in Chapter 3, that the average particle radius $\bar{r}$ increases with aging time t as $\bar{r} \propto t^{1/4}$. This result was obtained from the assumption that solute atoms diffuse two-dimensionally on a grain boundary. On the other hand, assuming that solute-atom diffusion occurred along intrinsic grain-boundary dislocations, Kreye [11] and Ardell [12] independently derived the relationship of $\bar{r} \propto t^{1/5}$.

In spite of the development of such theoretical studies, only a few experiments have been reported on the growth of boundary particles. Butler and Swann [2] examined the growth of boundary $MgZn_2$ particles in an Al-Zn-Mg alloy. They obtained the relationship of $\bar{r} \propto t^{1/n}$, where n varied between three (3) and just over four (4) depending on the misorientation angle of the two abutting grains separating the boundary. Recently, using the same alloy system, Czurratis *et al.* [3] showed that $\bar{r}$ is proportional to $t^{1/4}$ for particles on random high-angle boundaries.

The kinetics for the development of precipitate free zones (PFZs) along grain boundaries has also been studied. Sanders *et al.* [13] have shown that the PFZ width increases with $t^{1/3}$ during aging. On the other hand, Jensrud and Ryum [14] and Jha *et al.* [15] have found that the PFZ width is proportional to $t^{1/2}$. However, the usage of polycrystalline specimens in the above experimental studies has prohibited us from knowing how the particle and PFZ growth kinetics are related to the grain-boundary character .

In the present study, the growth of α-Fe-Co particles on [011] symmetric tilt boundaries of copper will be examined using orientation-controlled bicrystals. When a solution-treated Cu-Fe-Co alloy is aged, γ-Fe-Co (f.c.c.) particles precipitate in the copper matrix and α-Fe-Co (b.c.c.) particles which precipitate on grain boundaries of copper are known to exibit the KS orientation relationship to one of the two grains [8]. At the same time, PFZs are formed near the boundaries as a result of

the exhaustion of solute atoms. The Cu-Fe-Co alloy rather than the Cu-Fe alloy was chosen since ternary addition of Co to the Cu-Fe alloy is known to significantly enhance the grain-boundary precipitation [8].

6.2. Experimental

Bicrystals, 3mm thick, of a Cu-0.77mass%Fe-0.84mass%Co alloy containing various [011] symmetric tilt boundaries (with misorientation angles of $\theta = 5°$, 10°, 15°, 20° and 50.5°) were grown by the Bridgman method using seeds. The bicrystals were solution-treated at 1273K for 6h, quenched into water and subsequently aged at 873K for 1h to 96h in a vacuum.

The shape and size of the precipitated α-Fe-Co particles on various grain boundaries were examined on a 200kV TEM (Hitachi H-700) after making thin-foil specimens. For each boundary, over 100 particles were observed along the direction perpendicular to the [011] tilt axis and parallel to the grain boundary, as shown schematically in Fig. 6-1. As will be shown below, most α-Fe-Co particles were not nearly spherical but elongated. Therefore, their shape was approximated as spheroids expressed by $x^2/a^2+(y^2+z^2)/b^2 \leq 1$ with the aspect ratio a/b on an x-y-z coordinates. Furthermore, the assumed spheroid was reduced to an equivalent sphere of the same volume and its radius was defined as the particle radius. The PFZ width was measured at ten different locations and the average value was obtained.

6.3. Results

6.3.1. TEM Micrographs

Hereafter, a bicrystal with the misorientation angle θ and its grain boundary will be referred to as a θ bicrystal and a θ boundary, respectively. Figure 6-2 shows the TEM micrograph of the 5° boundary. This specimen was prepared from the aged 5° bicrystal at 873K for 8h. The coffee-bean like lobe contrasts in both grains indicate that coherent γ-Fe-Co particles precipitate finely in the copper matrix. On the other hand, very few α-Fe-Co particles were observed on the grain boundary. Although periodic arrays of larger strain-field contrasts can be seen on one side of the grain boundary, these are caused by the precipitation of coherent γ-Fe-Co particles on the boundary. Therefore, it is found that the precipitation of the equilibrium α-Fe-Co particles is difficult on such small-angle boundaries as the 5° boundary. This is consistent with the observation by Monzen *et al.* [9] that α-Fe-Co particles were not nucleated on small-angle boundaries with misorientation

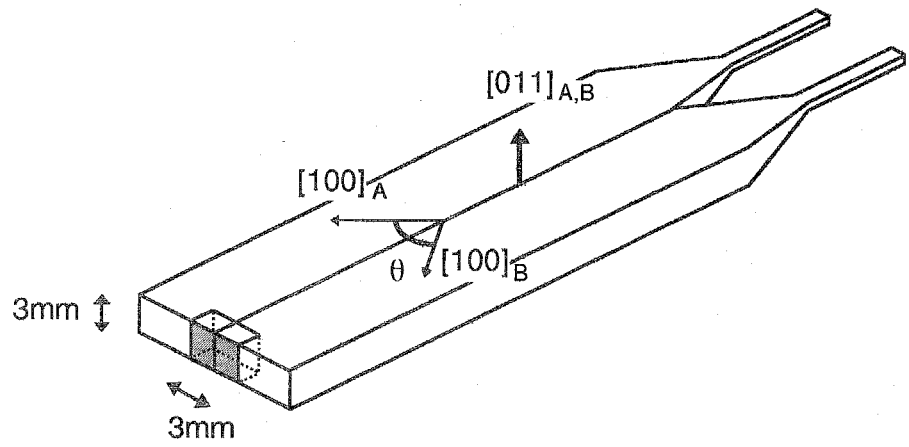

Fig. 6-1. Schematic illustration of a Cu-Fe-Co bicrystal with an [011] symmetric tilt boundary.

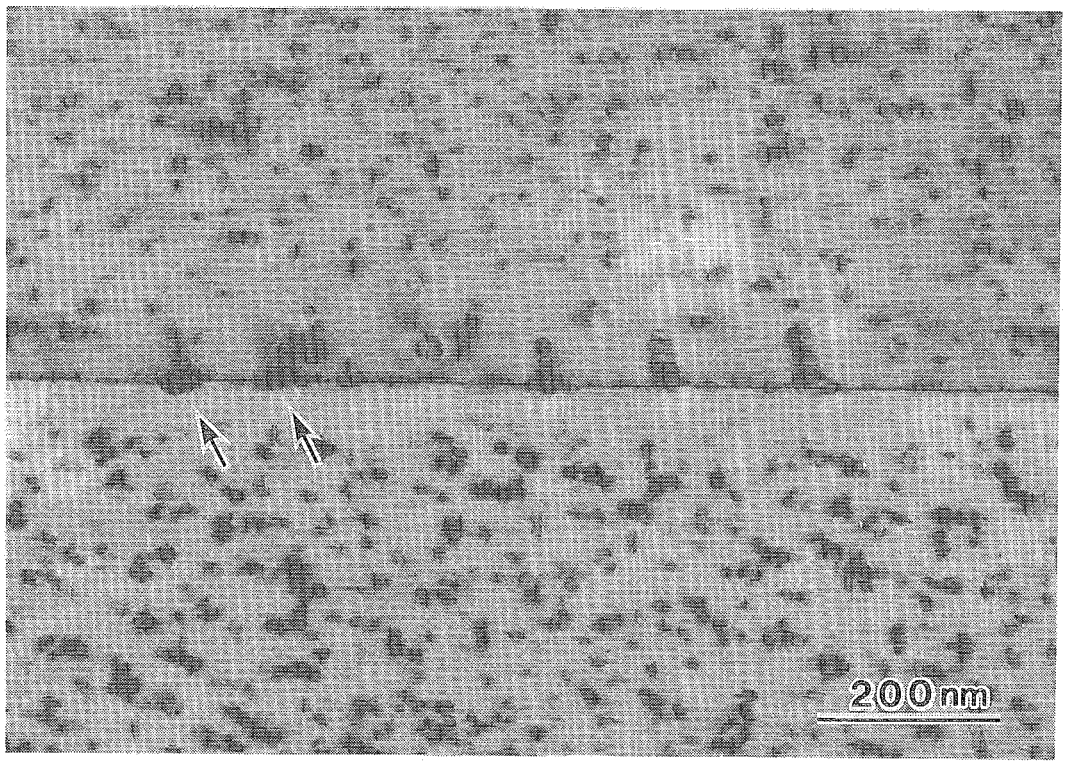

Fig. 6-2. TEM micrograph of a 5° boundary aged at 873K for 8h. The α-Fe-Co particles on the boundary are marked by the arrows.

smaller than 3°. In coincidence with the rare boundary precipitation, the PFZ width is also very narrow on either side of the 5° boundary.

For a 10° boundary, the precipitation and growth of the boundary α-Fe-Co particles occurs much more easily as shown in Fig. 6-3. As a result, clear PFZs are also observed on both sides of the boundary. It was found that upon further aging of the 10° bicrystal, the shape of the boundary α-Fe-Co particles remained rather spherical with a constant aspect ratio of about 1.4 although the volume of individual particles became larger. The same observation was performed for a 15° bicrystal. It was found that the morphology of the boundary particles and the PFZ width were very similar to those of the 10° bicrystals.

Figure 6-4 shows the α-Fe-Co particles on 20° boundaries. Compared with the particles on 10° and 15° boundaries, all the particles elongate significantly along [011] and become rod-like. It is interesting to know that this elongation direction is parallel to the [011] tilt axis of the symmetric boundary. In fact, this [011] direction was found to be the direction to describe the KS orientation relationship to one of the two abutting grains. In Chapter 3, it was found that in-grain α-Fe particles also grow and elongate along ⟨011⟩ by annealing. Therefore, regardless of the in-grain or boundary particles, the preferential growth direction of α-iron or α-Fe-Co particles appears to be determined at least partly by the crystallography (orientation relationship) of the particles in the copper matrix.

As aging time increases from 8h (Fig. 6-4 (a)) to 48h (Fig. 6-4 (b)), two major changes could be noted. First, the size and aspect ratio of the particles became larger. Secondly, the width of PFZs became larger. Similar characteristics were also found in specimens with a 50.5° boundary.

6.3.2. Growth of boundary α-Fe-Co particles

The change in the aspect ratio *a/b* of the grain-boundary particles was examined as a function of aging time at 873K and the results are shown in Fig. 6-5. Since the 5° boundary did not contain enough particles, the data could not be obtained. It can be seen that as misorientation becomes larger, the aspect ratio becomes larger. As mentioned above, for particles on the 10° and 15° boundaries, the aspect ratio is nearly constant and independent of aging time. On the other hand, the aspect ratio increases by aging for particles on 20° and 50.5° boundaries.

Figure 6-6 shows the variation of the mean particle radius $\bar{r}$ (as defined by the equivalent sphere, see Section 6.2) with aging time t. The only one data could be obtained for particles on a 5° boundary. It can be seen from Fig. 6-6 that for all the boundaries almost linear relationship exists between $\bar{r}$ and t when they are plotted on logarithmic scales. This means that $\bar{r}$ is essentially

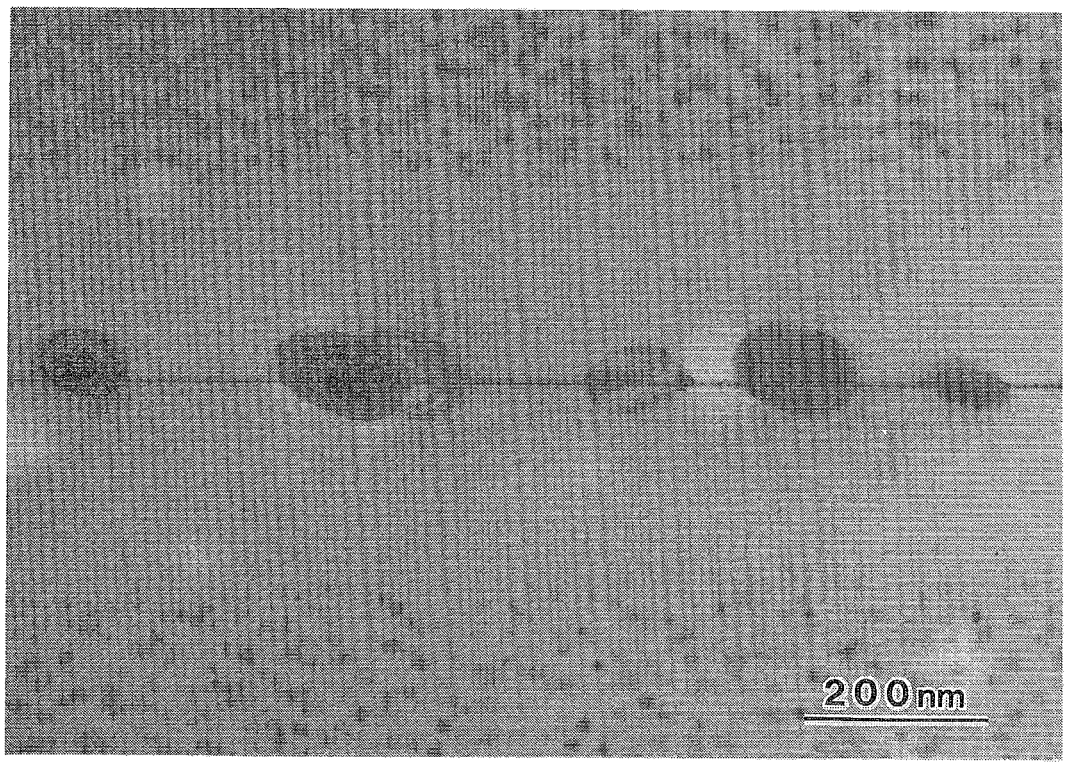

Fig. 6-3. TEM micrograph of a 10° boundary aged at 873K for 8h. Spherical boundary α-Fe-Co particles and clear PFZs are observed.

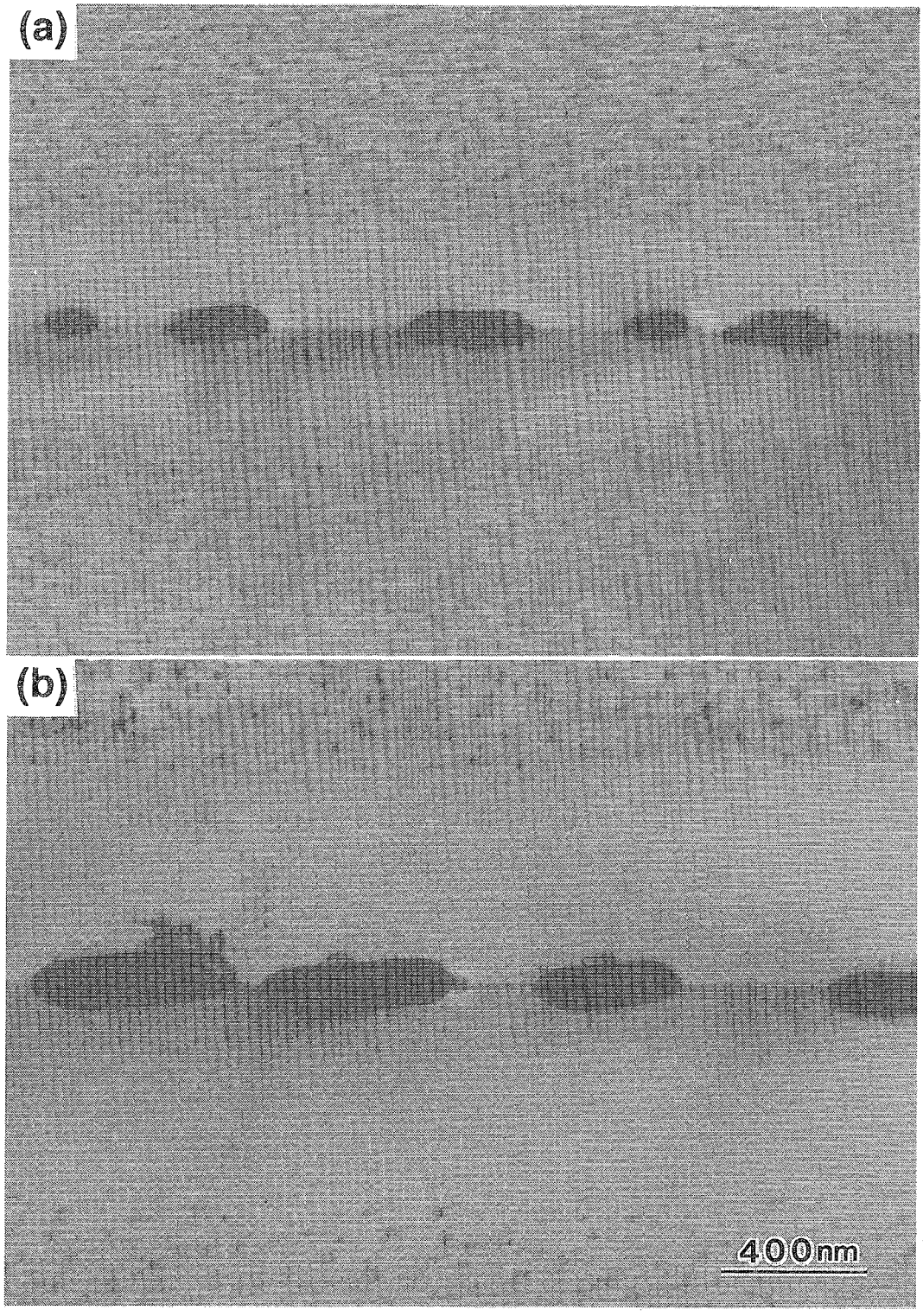

Fig. 6-4. TEM micrographs of a 20° boundary aged at 873K for (a) 8h and (b) 48h. The α-Fe-Co particles elongate along [011].

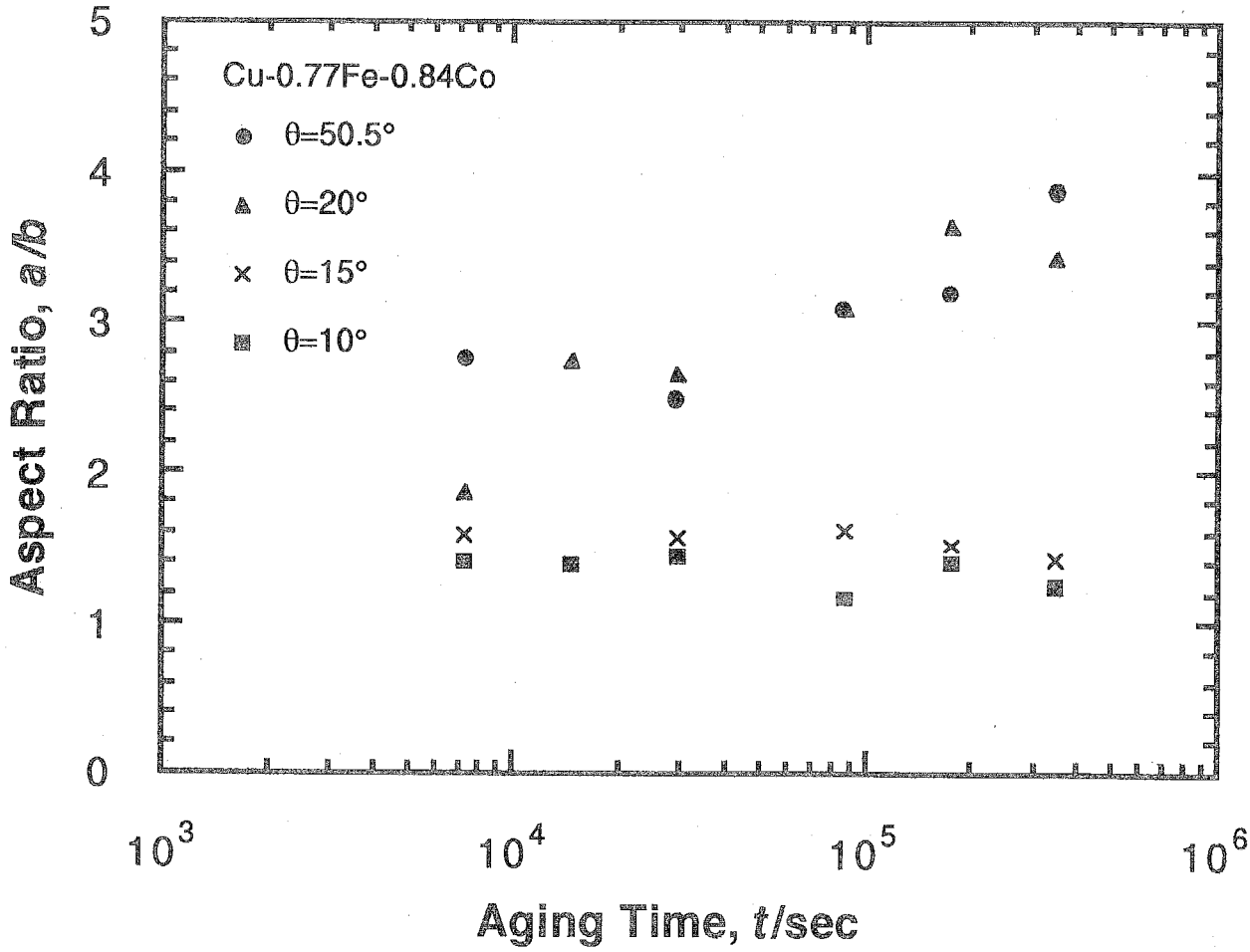

Fig. 6-5. Change in the aspect ratio of the grain-boundary particles with aging time.

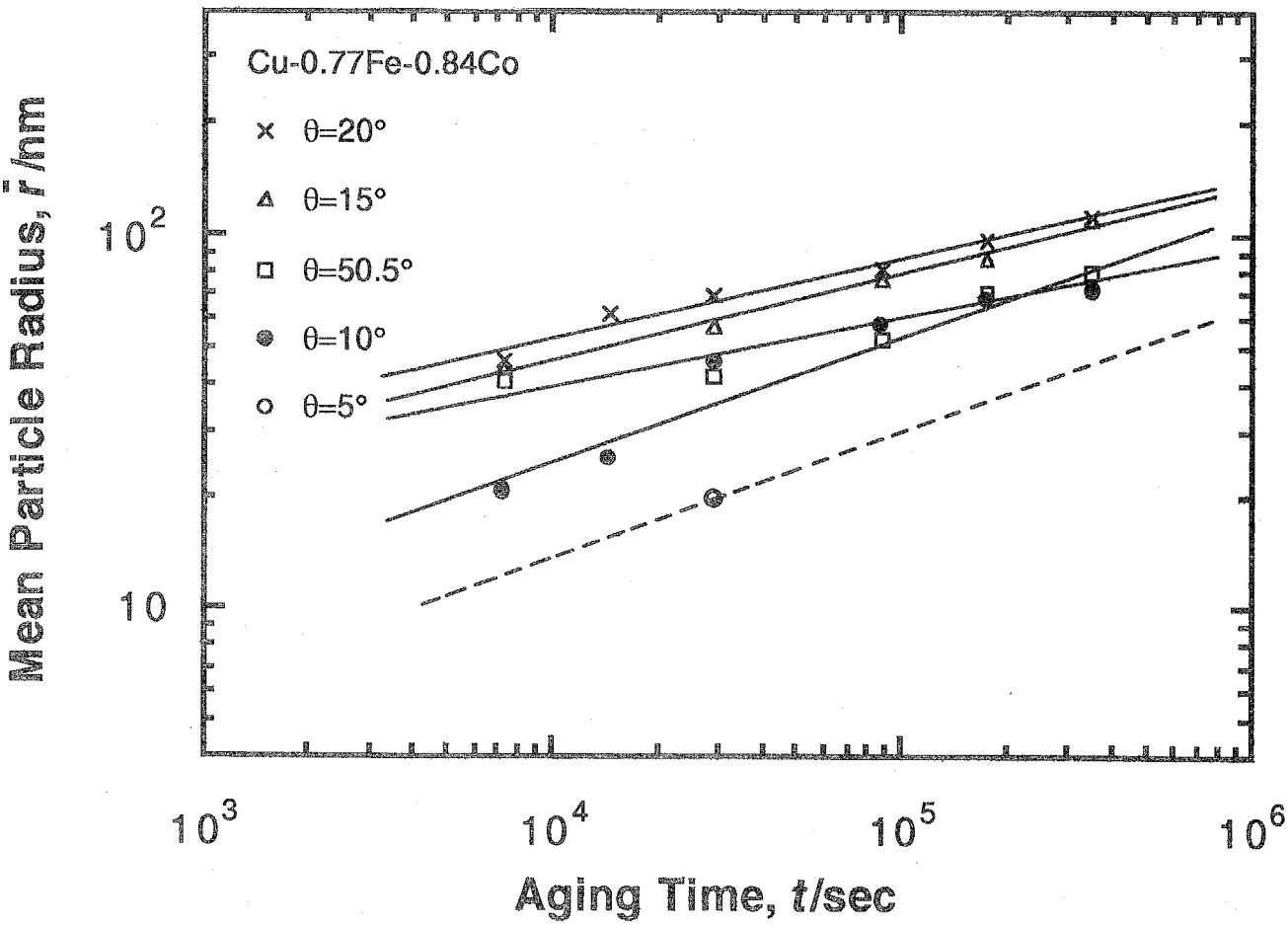

Fig. 6-6. Change in the mean particle radius with aging time. The straight lines were obtained by the least-square method.

proportional to $t^{1/n}$. The straight lines in the figure were drawn by the least-square method. From the slope of the straight line, n can be obtained for each bicrystal. The calculated results are shown in Table 6-1. (The value $n = 3$ for the 5° boundary is an expected one from a theoretical consideration in Section 6.4.2.) As found from this table, n increases from about three (3) to five (5) as misorientation increases from 10° to 50.5°. The implication of this result will be discussed later.

6.3.3. Development of PFZs during aging

Figure 6-7 shows the measured width d of the PFZ as a function of aging time t. Again in this figure, linear relationship is found to exist between log d and log t. However, different from the particle radius (Fig. 6-6), the PFZ width at any aging time does not depend significantly on misorientation. Therefore, the straight lines obtained by the least-square method nearly coincide with each other.

From their slope, m for $d \propto t^{1/m}$ can be obtained and the calculated results are shown in Table 6-2. It is interesting to find that regardless of misorientation, m is very close to two (2).

6.4. Discussion

6.4.1. PFZ width

For later purposes, the result in Fig. 6-7 will first be discussed. Figure 6-8 shows the grain-boundary energies of the Cu[011] symmetric tilt boundaries as a function of the misorientation angle θ. This result was obtained by Miura *et al.* [16] by measuring the shape of boundary SiO_2 particles. Except for the small energy cusp at $\theta = 38.9°$ ($\Sigma 9\{221\}$), the boundary energy increases monotonically with increase in θ for the range $\theta = 5°$~$50.5°$ of the present bicrystals.

It can be thought intuitively that the grain-boundary energy is larger in more irregular grain boundaries. Therefore, it would be safe to consider that as the misorientation angle increases from 5° to 50.5°, the structure of grain boundaries becomes more irregular and disturbed. From this, the fact that PFZs are not well developed in the 5° boundaries (Fig. 6-2) can be reasonably understood. These boundaries are less irregular than other boundaries and, therefore, the ability to absorb solute atoms (Fe and Co) must be smaller.

For the 10° to 50.5° boundaries, the PFZ width changed with time as $d^2 = K_1 t$ where K_1 is a constant. According to the theoretical work by Jha *et al.* [15], $m = 2$ is obtained by considering that the concentration of solute atoms on the surface of boundary particles differs from that in a grain.

Table 6-1. Calculated n value for each boundary.

Misorientation angle	n
5°	(3)
10°	2.97
15°	4.29
20°	4.64
50.5°	5.36

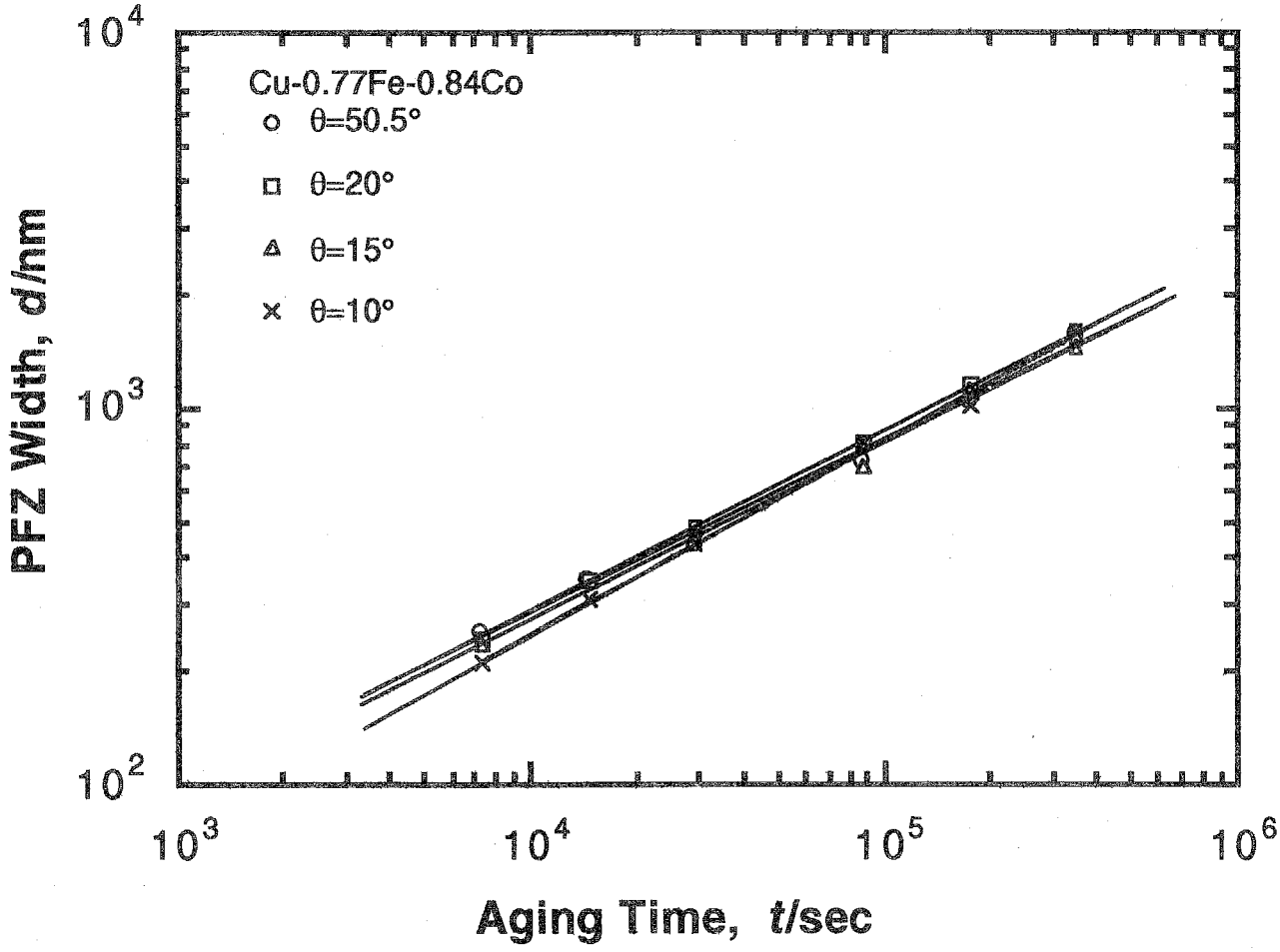

Fig. 6-7. Change in the PFZ width with aging time. The straight lines were obtained by the least-square method.

Table 6-2. Calculated m value for each boundary.

Misorientation angle	m
5°	—
10°	1.95
15°	2.13
20°	2.09
50.5°	2.17

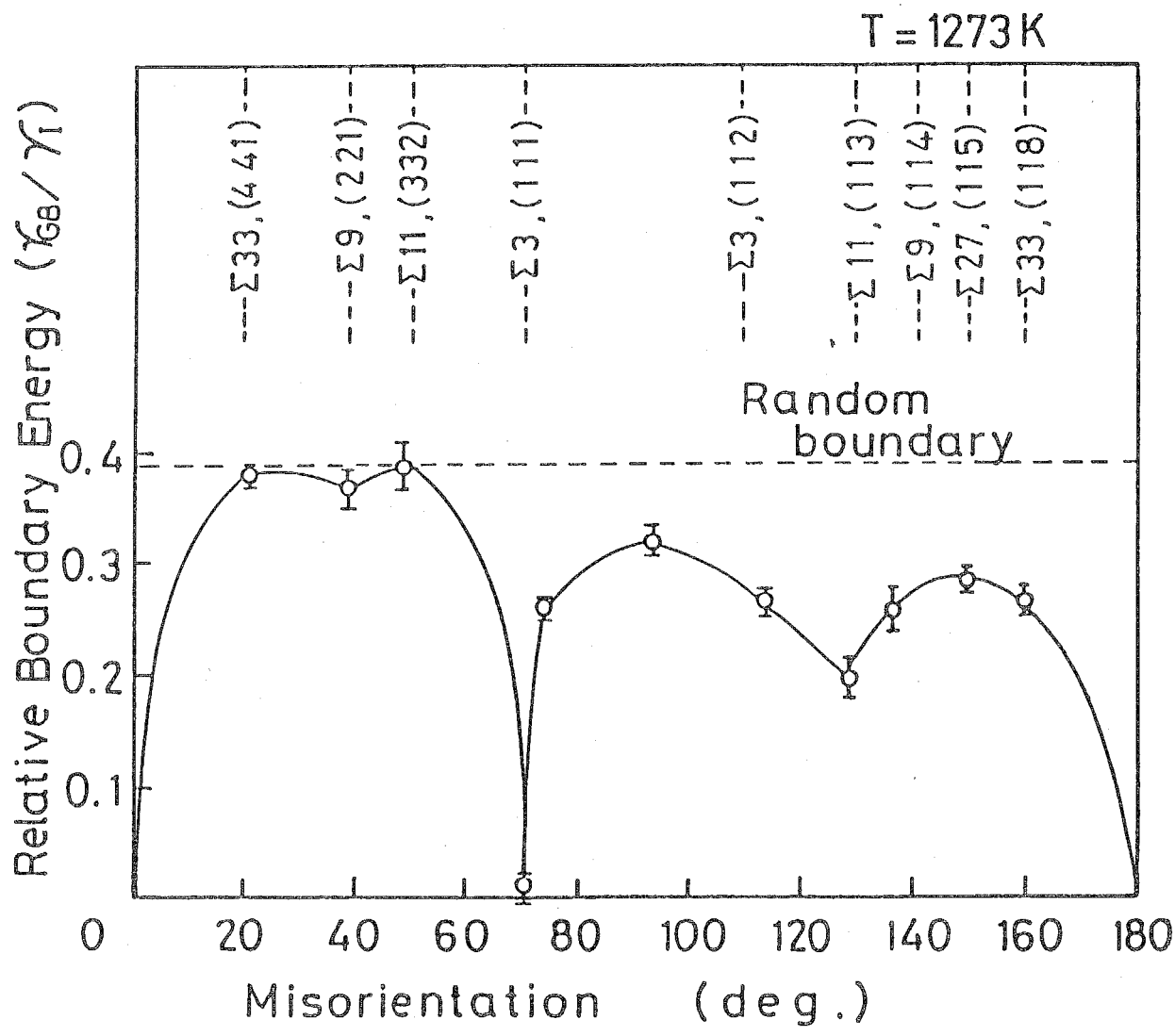

Fig. 6-8. The grain-boundary energy γ_{GB}, relative to the SiO_2/Cu interfacial energy γ_I, against the misorientation angle for [011] symmetric tilt boundaries in Cu [16].

This difference drives the solute atoms towards the grain boundary by bulk diffusion. As a result, the PFZs develop following the usual $(D_v t)^{1/2}$ kinetics (D_v: the bulk diffusion coefficient of solute atoms). Provided that there are enough sinks of solute atoms in a grain boundary, the kinetics of the bulk diffusion should not depend on the boundary character but depends only on the concentration gradient [15]. This is consistent with the present result in Fig. 6-7 that m is equal to two and K_1 is independent of the misorientation angle.

Different from the present result, Monzen *et al.* [9] reported that the PFZ width is wider along higher-energy boundaries. This result was obtained using the same Cu-Fe-Co alloy system aged at 873K for 1h. For this case, K_1 depends on the misorientation, or the grain-boundary character. It can be speculated that the nucleation rate and nucleation frequency of boundary particles depend on the boundary character. Therefore, during the early stage of aging where the nucleation of boundary particles occurs, solute atoms near the boundary would be directly absorbed in the boundary and, as a result, the PFZ width would vary with boundaries. However, during the growth stage after the completion of the nucleation, the PFZs widen by the bulk diffusion of solute atoms in the abutting grains. Since the result in Fig. 6-7 was obtained after long aging over 1h, the boundary particles are considered to be well in the growth stage. Therefore, the apparent discrepancy between the present result and that by Monzen *et al.* can be explained reasonably.

As shown in Fig. 6-7, PFZs continue to grow even after aging over 96h and their width does not show the tendency of saturation. This means that solute atoms are always supplied from the in-grain sources to the boundaries during the entire growth stage. The growth of boundary particles, therefore, is affected by the bulk diffusion of solute atoms. This is an important point to be remembered for the discussion of the growth mechanism of the boundary particles in the next section.

6.4.2. Growth of boundary α-Fe-Co particles

It has been found in Section 6.3.1. that the growth of the boundary particles depends on the boundary character or misorientation. As shown in Fig. 6-6 and Table 6-1, the power n for $\bar{r}^{\,n} = K_2 t$ (K_2: a constant) varied between three to five depending on the boundaries. According to the growth theories of boundary particles, $n = 5$ should be observed for the particle growth on small-angle boundaries (one-dimensional (1D) dislocation pipe diffusion) [11, 12, 18] and $n = 4$ on large-angle boundaries (2D grain-boundary diffusion) [10, 12, 17, 18]. For the growth controlled by 3D bulk diffusion, $n = 3$ is the case [19, 20], as discussed in Chapter 3.

Among the boundaries in the present study, 5° and 10° boundaries may be regarded as

small-angle boundaries. The structure of small-angle boundaries is often represented by regular arrays of dislocations [21]. Turnbull and Hoffman [22] successfully explained the misorientation dependence of grain-boundary diffusion through the short-circuit pipe diffusion along the boundary dislocations. Then, according to the above theories, $n = 5$ should be expected for these boundaries. However, the experimental results in Table 6-1 show that $n \approx 3$ for small-angle boundaries ($\theta =$ 10°) and $n \approx 5$ for large-angle boundaries ($\theta = 20°$ and 50.5°). This appears to be the opposite of the theoretical prediction. However, these seemingly unexplainable experimental results can be understood by considering the development of PFZs during aging.

As mentioned in the previous section, PFZs continue to widen on aging. Moreover, from the misorientation-independence of the m and K_1 values, the similar contribution of the 3D bulk diffusion towards the particle growth on all the observed boundaries is concluded. If we assume that all the present symmetric tilt boundaries consist of regular arrays of straight edge dislocations lying parallel to the [011] tilt axis, the distance h between the parallel edge dislocations is written as

$$h = b / 2\sin(\theta/2) \tag{6-1}$$

where b is the magnitude of the Burgers vector. Therefore, as misorientation increases, h decreases and the dislocation density in the boundaries increases. The pipe diffusion model by Turnbull and Hoffman [22] says that grain-boundary diffusivity is determined by the dislocation density and the kinetics of particle growth is expressed as [18]

$$\bar{r}^5 - \bar{r}_0^5 = K_d t \tag{6-2}$$

where

$$K_d = 5ZqI'CV_m^2 D_d / 4RT. \tag{6-3}$$

Here Z is the number of dislocations which meet a particle, q is the cross section of the dislocation pipe diffusion, D_d is the pipe-diffusion coefficient. Other constants have been defined in Chapter 3. Among various factors, only Z depends on the misorientation angle. Equations (6-2) and (6-3) indicate that pipe diffusion in small-angle boundaries has small contribution towards the particle growth since Z values for these boundaries are small. This means that the relative contribution of the above-mentioned bulk diffusion is large for the particle growth on small-angle boundaries. If

the bulk diffusion controls the particle growth, the power n should be equal to three (3), as discussed in Chapter 3. This is believed to be the case for the particle growth on 5° and 10° small-angle boundaries in the present study. In fact, $n = 2.97$ is obtained for the 10° boundary (Table 6-1). Although experimental data could not be obtained, $n = 3$ can also be expected for the 5° boundary, as indicated in Table 6-1. As misorientation increases, the dislocation density, and thus the Z value, increase in Eq. (6-3). On the other hand, the contribution of the bulk diffusion has been found to be the same. Therefore, the relative contribution of the pipe diffusion towards the particle growth increases and the n value should change gradually from 3 to 5. This is believed to be the reason why $n \approx 5$ was observed for the 20° and 50.5° boundaries and $n \approx 4$ for the intermediate 15° boundary.

One may argue that the dislocation model of grain boundaries is not applicable to such large-angle boundaries as the 20° and 50.5° boundaries. In fact, using the dislocation model for the 50.5° boundary, the distance between edge dislocations becomes $d = 1.2b$ from Eq. (6-1). Since d is so small, dislocation cores overlap. However, Hoffman [23] and Biscondi [24] experimentally showed that even in large-angle tilt boundaries, anisotropic diffusion occurred predominantly along the direction parallel to the tilt axis. Therefore, the dislocation model used in the present study may be justified at least qualitatively.

We have seen above that when the bulk diffusion plays an important role, the growth kinetics of boundary particles is similar to that of in-grain particles: The usual LSW rate equation for the 3D Ostwald ripening, discussed in Chapter 3, can be applied. The result obtained by Butler and Swann [2] that the n values range between three to four for the boundary precipitation of $MgZn_2$ particles in a polycrystalline Al-Zn-Mg alloy is considered to indicate the important role of the bulk diffusion in addition to the grain-boundary diffusion.

It has been pointed out [25] that the short-circuit grain-boundary diffusion appears most significantly in the temperature range between $T_m/2$ to $2T_m/3$ where T_m is the melting temperature. Since the present aging temperature of 873K is close to $2T_m/3$, the effect of the grain-boundary diffusion on the particle growth must have been masked by the stronger effect of the bulk diffusion, in particular for the 5° and 10° boundaries. Therefore, it is very probable that if a lower aging temperature was chosen, n became closer to four.

The above discussion, although satisfactorily explains the experimental results, is qualitative rather than quantitative. To make it a little more quantitative, let us consider the case of the 20° boundary and evaluate the 1D pipe diffusion coefficient D_d. Applying the result for $\theta = 20°$ in Fig. 6-6 and using Eqs. (6-2) and (6-3) together with the numerical values listed in Table 6-3, we obtain

Table 6-3. Numerical values used for the estimation of the pipe diffusion coefficient D_d.

Γ (J/m^2)	C (mol/m^3)	V_m (m^3/mol)	Z	q (m^2)
*3	**240	7.105×10^{-6}	75	25×10^{-20}

*[26], **[27]

$D_d = 2.4\times10^{-12}$ m^2/s at 873K or $T/T_m = 0.64$. This value is about 10^5 times larger than the bulk diffusion coefficient D_v of iron in a copper matrix at the same temperature. It is known empirically [25] that the ratios D_g/D_v (D_g: the grain-boundary diffusion coefficient) and D_d/D_v at the same T/T_m do not depend strongly on materials. Turnbull and Hoffman [22] obtained that $D_d/D_v \approx 10^6$ for the self pipe-diffusion coefficient of Ag at 773K ($T/T_m = 0.62$). Therefore, the obtained value of $D_d/D_v \approx 10^5$ at $T/T_m = 0.64$ is considered reasonable. Since the effect of the bulk diffusion is much smaller than that of the pipe diffusion for the 20° boundary, the observed $n = 4.64$, which is much larger than three and closer to five, can be understood.

6.4.3. Morphology of boundary α-Fe-Co particles

As shown in Figs. 6-2 to 6-4, the shape of boundary particles depends on the misorientation of the two grains; not far from spherical on 10° and 15° boundaries and rod-like on 20° and 50.5° boundaries. Here, factors controlling the shape of the boundary particles will be discussed.

Grain-boundary energy can be pointed out as one of the possible factors. It is well-known [16, 26] that the boundary particles become more oblate and lenticular with larger aspect ratios as the boundary energy increases. Such a lenticular shape is determined by the equilibrium between the boundary energy and the particle/matrix interfacial energy. In this case, the aspect ratio should not change during the quasi-equilibrium growth of the particles. However, Figure 6-5 shows that the aspect ratio keeps increasing even after prolonged aging for particles on the 20° and 50.5° boundaries. Therefore, the preferential growth of these particles along the [011] direction cannot be attributed entirely to the effect of the grain-boundary energy.

Another factor to determine the shape of the boundary particles is the crystallographic relationship between a particle and a matrix. As mentioned earlier, the boundary α-Fe-Co particles have a KS orientation relationship to one of the two copper grains and the [011] growth direction is that which describes the directional parallel relationship of the KS orientation. In Chapter 5, the growth of in-grain α-Fe particles has been examined and it has been found that crystallography plays an important role in the preferential growth along ⟨110⟩-type directions. Therefore, the present tendency towards the growth along [011] may well be determined crystallographically even for the boundary particles. However, if this is the only factor, it is difficult to understand why the aspect ratio of the particles on low-misorientation boundaries ($\theta = 5°$ and 10°) did not change on aging (Fig. 6-5). To understand this point, one more factor related to the kinetics of the particle growth must be taken into account.

As mentioned in 6.4.2., the anisotropic diffusion parallel to the [011] tilt axis prevails in the

present symmetric tilt boundaries. Moreover, the diffusivity is larger in boundaries with larger misorientation angles. Therefore, it is reasonable to consider that the preferential diffusion along [011] caused the elongation of particles along the same direction. The elongation must be more enhanced as the diffusivity increases. This means that the particles on 20° and 50.5° boundaries should elongate more significantly than those on 10° and 15° boundaries. This is in agreement with the experimental results shown in Fig. 6-5.

Finally, the reason why the precipitation of boundary α-Fe-Co particles is very difficult on small-angle boundaries (such as the 5° boundary in the present study) will be briefly discussed. As shown in Fig. 6-2, metastable γ-Fe-Co particles rather than stable α-Fe-Co particles prevailed on the 5° boundary. The scarceness of stable boundary particles on a small-angle boundary is in agreement with the observations by Unwin and Nicholson [1] and by Monzen *et al.* [9]. Furthermore, the precipitation of metastable particles is in qualitative agreement with the study by Vaughan [27]. Generally speaking, when boundary particles precipitate, the grain-boundary energy decreases and the particle/matrix interfacial energy increases. When the overall energy change is negative, the precipitation is energetically possible. The interfacial energy between incoherent α-Fe-Co particles and the copper matrix must be much larger than that between coherent γ-Fe-Co particles and the copper matrix. In fact, as discussed in Chapter 3, a factor of 15 difference exists for the case of the iron particles. Therefore, if the incoherent α-Fe-Co particles precipitate on such low-energy small-angle boundaries as the 5° boundary, the increase in the interfacial energy cannot be compensated for by the decrease in the grain-boundary energy. This is considered to be the reason why the precipitation of α-Fe-Co particles was very difficult on the 5° boundary. It is of course very probable that the solute concentration on such a small-angle boundary is small. However, this cannot explain why the γ-Fe-Co particles precipitated rather than the α-Fe-Co particles.

6.5. Summary and conclusions

In this Chapter 6, the precipitation of α-Fe-Co particles on various [011] symmetric tilt boundaries of copper was examined using orientation-controlled bicrystals of a Cu-0.77mass%Fe-0.84mass%Co alloy. The results and conclusions are summarized as follows.

(1) On the small-angle boundary with 5° misorientation, although some γ-Fe-Co particles existed, α-Fe-Co particles hardly precipitated and the width of PFZs was very narrow. It is concluded that since the 5° boundary is a low-energy boundary, the increase in the particle/matrix interfacial

energy associated with the precipitation of the incoherent α-Fe-Co particles can hardly be compensated for by the decrease in the grain-boundary energy.

(2) The shape of boundary α-Fe-Co particles depended on the misorientation angle θ. On $\theta = 10°$ and 15° boundaries, the particles were nearly spherical, while on 20° and 50.5° boundaries, they were rod-like with the longitudinal direction parallel to the [011] tilt axis. It is concluded that not only crystallography but also anisotropic pipe diffusion along [011] is responsible for the misorientation-dependent shape of the boundary particles.

(3) The relationship $d^2 = K_1 t$ (K_1: a constant) was found to hold between the width d of PFZs and the aging time t for all the bicrystals investigated. From this, it is concluded that solute Fe and Co atoms are always supplied by bulk diffusion from the in-grain sources to the boundaries during the growth process of boundary particles.

(4) The relationship $\bar{r}^{\,n} = K_2 t$ (K_2: a constant) existed between the average radius $\bar{r}$ of boundary particles and the aging time t. Here the power n changed systematically from three (3) to five (5) as misorientation increases from 10° to 50.5°. Therefore, it has been found that the kinetics of the growth of boundary particles depends on the misorientation angle. The change in the n values can be explained reasonably by considering the relative contribution of bulk diffusion and dislocation pipe diffusion towords the particle growth.

References

[1] P. N. T. Unwin and R. B. Nicholson: *Acta Metall.*, **17** (1969), 1379.

[2] E. P. Butler and P. R. Swann: *Acta Metall.*, **24** (1976), 343.

[3] P. Czurratis, P. Kroggel and H.Löffer: *Z. Metallk.*, **79** (1988), 307.

[4] J. K. Park and A. J. Ardell: *Acta Metall.*, **34** (1986), 2399.

[5] J. K. Lee and H. I. Aaronson: *Acta Metall.*, **23** (1975), 799.

[6] J. K. Lee and H. I. Aaronson: *Acta Metall.*, **23** (1975), 803.

[7] J. Le Coze, M. Biscondi, J. Levy and C. Goux: *Mém. Sci. Rev. Mét.*, **70** (1973), 397.

[8] R. Monzen and K. Kitagawa: *Scripta Metall.*, **22** (1988), 173.

[9] R. Monzen, K. Kitagawa, M. Kato and T. Mori: *J. Jap. Inst. Met.*, **54** (1990), 1308.

[10] M. V. Speight: *Acta Metall.*, **16** (1968), 133.

[11] H. Kreye: *Z. Metallk.*, **61** (1970), 108.

[12] A. J. Ardell: *Acta Metall.*, **20** (1972), 601.

[13] T. H. Sanders Jr., E. A. Ludwiczak and R. R. Sawtell: *Mater. Sci. Eng.*, **43** (1980), 247.

[14] O. Jensrud and N. Ryum: *Mater. Sci. Eng.*, **64** (1984), 229.

[15] S. C. Jha, T. H. Sanders Jr. and M. A. Dayananda: *Acta Metall.*, **35** (1987), 473.

[16] H. Miura, M. Kato and T. Mori: *Colloq. de Phys.*, **51** (1990), C1-263.

[17] H. O. K. Kirchner: *Metall. Trans.*, **2** (1971), 2861.

[18] R. D. Vengrenovitch: *Acta Metall.*, **30** (1982), 1079.

[19] I. M. Lifshitz and V. V. Slyozov: *J. Phys. Chem. Solids*, **19** (1961), 35.

[20] C. Wagner: *Z. Elektrochem.*, **65** (1961), 581.

[21] W. T. Read and W. Shockley: *Phys. Rev.*, **78** (1950), 275.

[22] D. Turnbull and R. E. Hoffman: *Acta Metall.*, **2** (1954), 419.

[23] R. Hoffman: *Acta Metall.*, **4** (1956), 98.

[24] M. Biscondi: *Physical Chemistry of the Solid State, Application to Metals and their Compounds*, Ed. by P. Lacombe, Amsterdom, Elsevier, (1984), 225.

[25] P. G. Shewmon: *Diffusion in Solids*, New York, McGraw-Hill, (1963).

[26] T. Fujii, M. Kato and T. Mori: *Mater. Trans., JIM*, **32** (1991), 229.

[27] G. Tammann and W. Oelsen: *Z. anorg. allog. Chem.*, **186** (1930), 257.

[28] T. Mori, H. Miura, T. Tokita, J. Haji and M. Kato: *Phil. Mag. Let.*, **58** (1988), 11.

[29] D. Vaughan: *Acta Metall.*, **16** (1968), 563.

Chapter 7.

General Summary and Future Prospects

7.1. General summary and conclusions

In this thesis, studies on various aspects of physical metallurgy, (1) phase transformation, (2) growth and coarsening kinetics of precipitates, (3) magnetism and (4) crystallography of precipitates, of iron (iron-cobalt) particles in a copper matrix have been described. The unique feature of the Cu-Fe alloy system and the usage of orientation-controlled single and bicrystals have enabled us to significantly extend the knowledge on the above various subjects.

The contents and main findings of this thesis are summarized as follows:

In Chapter 1, "General Introduction", the historical backgrounds and the motivation and aim of the present studies have been mentioned.

In Chapter 2, "Stress Effects on the Martensitic Transformation of Small Iron Particles in a Copper Matrix", the stress effect on the $\gamma \rightarrow \alpha$ martensitic transformation in small iron particles in a single-crystal copper matrix has been examined. It has been found that specific Kurdjumov-Sachs variants out of 24 crystallographically equivalent ones are formed preferentially depending on the direction ([001] or [419]) and sense (tension or compression) of the applied stress. Compressive deformation induces more martensites than tensile deformation for specimens stressed along $[001]_f$. On the other hand, for specimens stressed along $[419]_f$, no significant differences has been found between tensile and compressive deformations. In polycrystalline specimens, tensile deformation induces more martensites than compressive deformation. These experimental results can be understood reasonably and consistently if the significant stress effect on the f.c.c.$\rightarrow$b.c.c. lattice change in the early stage of the martensitic transformation is considered.

In Chapter 3, "Growth of α-Iron Particles in a Copper Matrix", the growth kinetics of α-iron particles in a copper matrix has been examined. By applying the Lifshitz-Slyozov-Wagner (LSW) theory for Ostwald ripening, the α-Fe/Cu interfacial enegy of $3.3 J/m^2$ has been evaluated from the growth curve. The growth kinetics has also been studied for the case where both α- and γ-iron particles co-exsist. The LSW theory has been found to be effective to treat the individual particle growth kinetics when the growth of α- and γ-iron is followed separately. It is also concluded that when the two types of particles coexist, the difference in chemical free energies of the γ- and α-iron must also be considered in their growth process in addition to the effects of particle size and interfacial energies. Furthermore, fundamental rate equations for the Ostwald

ripening have been derived in a simple manner by taking directly into account the change in the precipitate/matrix interfacial free energy. This method enables us to image the physics involved in the rate equations very easily.

In Chapter 4, "Magnetic Anisotropy Caused by the Formation of Stress-Induced Martensite in Small Iron Particles in a Copper Matrix", magnetic anisotropy of the deformed and successively annealed Cu-Fe single crystals with transfomed α-iron particles has been examined by measuring magnetic torque around $(\bar{1}\,1\,\bar{1})_f$. The shape of the torque curves depends strongly on the sense of the applied stress while the amplitude of the curves becomes larger with increase in annealing time. The stress-dependent shape reflects the preferential formation of specific stress-induced martensite variants out of crystallographycally equivalent ones. The annealing time-dependent growth of the amplitude of the torque curves reflects the spherical to ellipsoidal shape change of the α-iron particles. These results are in good agreement with those of the TEM observations in Chapter 2.

In Chapter 5, "Crystallography and Morphology of Needle-Like α-Iron Particles in a Copper Matrix", the crystallography and morphology of elongated α-iron particles in a copper matrix have been examined. Two types of growth directions, $\langle 110 \rangle_f$ and $\langle 16\ 19\ 3 \rangle_f$, are observed. The precipitate/matrix interface consists of several facets of habit planes. The predominant habit plane orientations of the $\langle 110 \rangle_f$ elongated particles are $\{111\}_f/\{110\}_b$ and $\{112\}_f/\{321\}_b$. These observed crystallography and morphology of the α-iron particles have been explained excellently by combining the simple geometrical and physical criteria, *i.e.*, invariant-line deformation criterion and the strain-energy minimization criterion.

In Chapter 6, "Growth of Grain-Boundary Precipitates in Cu-Fe-Co Bicrystals", the growth of α-Fe-Co precipitates on various [011] symmetric tilt boundaries in Cu-Fe-Co bicrystals has been examined. It has been found that, on a small-angle grain boundary with 5° misorientation, α-Fe-Co particles hardly precipitate and the width of the precipitate free zones (PFZs) is very narrow. The shape of the particles depends on the misorientation angle θ as a result of preferential diffusion along the tilt axis; nearly spherical on θ = 10° and 15° boundaries while elongated rod-like along the [011] tilt axis on 20° and 50.5° boundaries. It has been found that the relationship $d^2 = K_1 t$ (K_1: a constant) holds between the PFZ width d and the aging time t for all the boundaries investigated. On the othe hand, the relationship $\bar{r}^{\,n} = K_2 t$ (K_2: a constant) exists between the average particle radius $\bar{r}$ and the aging time. The misorientation-dependent change in the n values from three to five as θ increases from 5° to 50.5° can be explained by considering the relative contribution of bulk diffusion and dislocation pipe diffusion towards the particle growth.

7.2. Future prospects

Although the Cu-Fe and Cu-Fe-Co alloys were used in the studies described in this thesis, many of the obtained results are considered to be more generally applicable to other alloy systems. Here, to conclude this thesis, some remarks will be made as to what results are regarded to be very general and what still remain to be investigated in future.

Related to Chapter 2, the conclusion that the stress effect appears most predominantly in the early stage of martensitic transformations to change the lattice is believed to be a general one. The usage of the Cu-Fe alloy single crystals was very advantageous to examine this subject. Clever experiments, such as that in the present study, must be performed for other alloy systems to ensure the universality of the present conclusion.

In Chapter 3, the growth kinetics of α-iron particles in a copper matrix was examined for the cases of (i) α-iron particles alone and (ii) coexisting α- and γ-iron particles. The particle growth under the condition of the coexistence of two different types (coherent and incoherent) of the particles has neither experimentally nor theoretically been studied in detail. In the usual growth kinetics, only the reduction in the interfacial free energy is considered as the driving force for the particle growth. On the contrary, for the coexisting case, thermal stability, or the difference in chemical free energies between the two types of particles, must also be taken into account in the theoretical analysis. The theoretical understanding of this subject is a challenging problem to be pursued in future.

Furthermore, the growth kinetics must be modified to treat more rigorously the case of non-spherical particle growth. Since other factors such as anisotropic interfacial energy and interfacial diffusion must be introduced in the analysis, this problem is considered to be highly complicated. Computer simulation may, in general, be necessary to treat the case.

The technique of the magnetic anisotropy measurement discussed in Chapter 4 is considered useful not only for the scientific study of basic magnetic properties of materials but also for the engineering investigation of, say, texture in steels. If austenite is paramagnetic and ferrite and martensite are ferromagnetic, stress-induced transformation texture can easily be detected by the magnetic anisotropy measurement. The combination of this technique and the discussed stress effects in Chapter 2 will hopefully help us understand such phenomena as deformation texture and the development of internal stresses.

The study on the crystallography and morphology of precipitate particles in Chapter 5 is interesting in a sense that simple geometrical criteria were found to be excellently applicable to this

case. As mentioned in the text, such geometrical criteria have been known to be useful in explaining the crystallography of plate-like martensites and epitaxy between deposit and substrate crystals. The present study suggests their wider application possibility to various other diffusion-controlled precipitation products. It is, of course, true that simple geometrical criteria fail to be applicable for certain systems, in particular for systems with strong interatomic interactions. Therefore, it is interesting to know the ranges of the applicability and limitations of these geometrical criteria for diffusionless and diffusion-controlled transformations and epitaxies.

For Chapter 6, it must be pointed out that more extensive and systematic studies are necessary to establish the roles of grain boundaries on the precipitation and growth of boundary particles. Considering the important effects of grain-boundary segregation and precipitation on mechanical properties of materials, the lack of systematic data is a serious problem. There are many factors which make the study on the boundary precipitation and growth very complicated and tedious. To list some, grain-boundary character, bulk diffusion, grain-boundary diffusion, dislocation pipe diffusion, particle/matrix interfacial energy, etc. The present study can be regarded as a first attempt for the systematic investigation of this subject. As we have seen, the use of orientation-controlled bicrystals is a must for such studies. Even if the same alloy system is chosen, data for many other bicrystals and aging conditions (temperature and time) must be collected to find which of the above factors are important under what conditions.

As listed above, even if we limit ourselves to the subjects treated in this thesis, many problems still remain to be solved in future. Although the studies described in this thesis are not yet complete and comprehensive, I hope they contribute for the better to the understanding of the above various subjects.

Acknowledgments

Five years have passed since my growth stage, or my research life, started at Nagatsuta. Professor Masaharu Kato, my advisor, supplied me the great driving force and essential power for the growth. I cannot express my gratitude to him enough in this narrow space. Thus my acknowledgment to him will be completed sometime in future.

I am deeply indebted to Professor Tsutomu Mori, my co-advisor, for his fruitful advice and encouragement during the course of this study.

I am grateful to Professors Akikazu Sato and Minoru Wada for helpful discussions.

Other persons to whom I owe this thesis are as follows:

Dr. Shiro Horie, Mr. Yasuo Hoshino,
Mr. Miki Moriyama, Mr. Teruhiro Enami,
Dr. Yoshimi Watanabe, Miss Kumi Okawa,
Professor Ryoichi Monzen (Kanazawa University),
Dr. Susumu Onaka (Kyoto University).

Finally, I would like to express my appreciation to my parents for their encouragement.

August, 1992

藤居俊之

Toshiyuki Fujii